

Exact CHY Integrand Construction Using Combinatorial Neural Networks and Discrete Optimization

Simeng Li^a Yaobo Zhang^a

^a*School of Physics, Ningxia University, Yinchuan, 750021, China*

E-mail: yaobozhang@zju.edu.cn, 3102532061@qq.com

ABSTRACT: We present a novel approach to the inverse CHY problem—constructing integrands from desired pole structures—by establishing a correspondence between CHY combinatorics and Combinatorial Neural Networks (CNNs). Our key innovation is the generalized pole degree $K(s_A)$, which is additive under integrand multiplication and satisfies hierarchical recursion relations. These recursions naturally map to CNN message-passing architectures, enabling discrete automatic differentiation that preserves exact integer constraints throughout the computation. Unlike conventional machine learning approaches that yield numerical approximations, our method leverages the intrinsic combinatorial structure of the CHY formalism to guarantee exact algebraic solutions. This work demonstrates how specialized neural architectures can solve fundamental physics problems requiring strict mathematical constraints, providing a modest step toward bridging combinatorics, machine learning, and scattering amplitude theory.

KEYWORDS: Scattering Amplitudes, CHY Formalism, Combinatorial Neural Networks, Discrete Automatic Differentiation, Integer Linear Programming, Inverse Problem

Contents

1	Introduction	2
1.1	Background: The CHY Formalism and AI in Theoretical Physics	2
1.2	From Graphs to Combinatorial Neural Networks	3
2	Graph-Theoretic Structure of CHY Integrands	5
2.1	Integrand as 4-Regular Graph and Integration Rules	5
2.2	Combinatorial Structure of Generalized CHY Graphs	6
2.3	Recursion Relation for Generalized Pole Degree $K(s_A)$	7
2.4	Bootstrap Equations for Integrands	10
2.5	Examples of Bootstrap Construction	12
3	From Poles to Simplices: A Topological Perspective	16
3.1	Simplicial Structure in CHY Pole Hierarchies	16
3.2	Combinatorial Neural Networks and Discrete Automatic Differentiation	18
3.3	Neural-Inspired Pick-Pole Algorithm	21
3.4	Examples of 6-Point CHY Integrands	23
4	Applications to Higher-Order Pole Expansion	32
4.1	Cross-Ratio Identities and Higher-Order Poles	32
4.2	Decomposing 0-Regular Graphs into Cross-Ratios	33
4.3	Examples: 6-Point CHY Integrand with Higher-Order Poles	35
5	Conclusion	41
A	Proofs of Recursion Relations of $K(A)$	44
B	Solving Bootstrap Equations via Integer Linear Programming	45
C	Hamiltonian Cycles and 0-Regular Graph Decomposition	51
D	Discrete AD-Based Neural Network Examples on 8-Point CHY Integrands	54
E	Examples: 8-Point CHY Integrand with Higher-Order Poles	63

1 Introduction

The Cachazo-He-Yuan (CHY) formalism [1–3] provides a compact and universal representation of tree-level scattering amplitudes in a wide range of quantum field theories, including Yang-Mills, gravity, and scalar theories. In this framework, amplitudes are written as integrals over the moduli space of n marked points on the Riemann sphere, localized by the scattering equations—a set of algebraic constraints that reflect momentum conservation and on-shell conditions.

While much progress has been made on evaluating CHY integrals for a given integrand—what we refer to as the “forward CHY problem”—a less explored and equally fundamental question is the *inverse CHY problem*: Given a desired set of physical singularities (i.e., pole structures), how does one construct a CHY integrand that produces them? This inverse direction is combinatorially complex, especially for high-multiplicity processes and integrands with nontrivial numerator structures.

In this paper, we propose a systematic approach to address the inverse CHY problem by establishing an unexpected connection between CHY integrands and combinatorial neural networks. We introduce a generalized pole degree $K(s_A)$ that satisfies elegant recursion relations, transforming the inverse problem into integer linear programming. Most remarkably, these recursion relations naturally correspond to the architecture of combinatorial neural networks, enabling us to develop discrete automatic differentiation algorithms that guarantee exact solutions.

1.1 Background: The CHY Formalism and AI in Theoretical Physics

The CHY formalism expresses an n -particle scattering amplitude \mathcal{A}_n as an integral over the positions of n punctures $\{z_i\}$ on the Riemann sphere:

$$\mathcal{A}_n = \int \frac{\prod_{i=1}^n dz_i}{\text{vol}(\text{SL}(2, \mathbb{C}))} \Omega(\mathcal{E}) \mathcal{I}(z). \quad (1.1)$$

The measure $\Omega(\mathcal{E})$ enforces the scattering equations

$$\mathcal{E}_a \equiv \sum_{b \neq a} \frac{s_{ab}}{z_a - z_b} = 0, \quad (1.2)$$

which relate external kinematics to the geometry of the punctured sphere. Different quantum field theories are encoded by different CHY integrands $\mathcal{I}(z)$, which specify the dynamical content of the amplitude. The formalism was originally introduced for tree-level amplitudes in a variety of massless theories [3, 4], and later extended to polynomial forms [5].

The CHY formalism’s remarkable universality has established it as a cornerstone of modern amplitude methods, providing a unifying framework that elegantly connects diverse quantum field theories. Since its inception, the formalism has revealed profound connections between seemingly disparate theories—from bi-adjoint scalars to Yang-Mills and gravity—through the simple modification of integrand functions $\mathcal{I}(z)$. This universality continues to yield new insights, as demonstrated by recent discoveries of novel factorization properties in Yang-Mills amplitudes [6, 7], which further illuminate the hidden structures within the CHY framework.

The formalism’s reach extends beyond tree-level physics, with significant progress in loop-level generalizations. Recent developments have successfully extended CHY methods to one-loop amplitudes in gauge theories [8]. These advances build upon earlier breakthroughs, including the forward-limit construction for loop integrands [9, 10] and the development of ambitwistor string theory connections [11, 12].

Within this rich landscape, computational tools have evolved to match the formalism’s sophistication. The “pick pole” algorithm, designed to isolate contributions containing specific physical singularities $1/s_A$, exemplifies the deep interplay between mathematical structure and practical computation [13, 14]. For bi-adjoint scalar theory, this algorithm admits an elegant implementation based on contiguity properties of particle orderings. The extension to more general CHY integrands, particularly those associated with labelled tree graphs [15] and higher-order poles [16], reveals increasingly intricate mathematical structures that continue to inspire new approaches.

The computational challenges inherent in CHY calculations—from solving scattering equations to managing combinatorial complexity—have stimulated cross-disciplinary innovations. Recent work has explored connections to tropical geometry [17], positive geometries [18], and intersection theory [19], demonstrating how the CHY formalism serves as a bridge between theoretical physics and modern mathematics. It is within this vibrant and expanding research landscape that we contribute our perspective, leveraging emerging techniques from discrete optimization and topological data analysis to address longstanding computational challenges while revealing new mathematical structures within the CHY framework.

Concurrent with these developments, theoretical physics has witnessed a paradigm shift with the integration of artificial intelligence and machine learning techniques. In string theory, machine learning has been employed to navigate the vast landscape of Calabi-Yau manifolds [20–22]. For scattering amplitudes, neural networks have shown promise in evaluating loop integrals [23, 24], optimizing phase-space integration [25], and learning amplitude symmetries [26, 27]. The transformer architecture has proven remarkably effective for symbolic computations in quantum field theory [28, 29]. This progress reflects the emergence of AI-driven discovery as a new paradigm in science [30, 31], where the goal extends beyond predictive models to developing explainable AI that translates patterns into physical insights [32, 33].

However, most machine learning applications in physics rely on continuous optimization yielding approximate results. For the CHY formalism, where exact algebraic structures and integer constraints are paramount, conventional approaches are unsuitable. This motivates our development of a fundamentally different framework based on discrete optimization and exact algorithms.

1.2 From Graphs to Combinatorial Neural Networks

Our key insight is that the pole structure of CHY integrands naturally exhibits a hierarchical organization that can be precisely captured by combinatorial neural networks—architectures originally developed for processing higher-order topological structures in data science [34, 35]. This represents a conceptual leap: rather than applying standard machine

learning tools to approximate solutions, we identify an exact correspondence between the mathematical structure of CHY integrands and these specialized neural architectures.

We begin by extending the conventional pole index $\chi(A) = L[A] - 2(|A| - 1)$ to introduce the generalized pole degree $K(s_A)$, which measures the net number of internal edges within particle subsets. This quantity exhibits remarkable combinatorial properties: it behaves additively under integrand multiplication, transforming the complex problem of integrand composition into simple integer arithmetic. More importantly, $K(s_A)$ satisfies hierarchical recursion relations:

$$K(A) = \frac{1}{(|A| - 2)!} \sum_{\substack{B \subset A \\ |B|=|A|-1}} K(B), \quad (1.3)$$

which encode the complete pole structure in terms of two-particle data.

Building on these recursive properties, we formulate the inverse CHY problem as a systematic bootstrap procedure. Given a desired pole structure, we show that the construction of appropriate CHY integrands reduces to solving a mixed integer linear programming problem. The fundamental insight is that the hierarchical recursion relations create a system of linear constraints on the two-particle pole degrees $\{K(s_{ij})\}$, enabling systematic exploration of the space of possible theories within the CHY framework.

Interestingly, we discover that the hierarchical recursion structure of $K(s_A)$ corresponds precisely to the architecture of combinatorial neural networks. This connection reveals that the inverse CHY problem can be reformulated as a discrete backpropagation process operating on simplicial complexes. Unlike continuous automatic differentiation used in standard machine learning frameworks, our approach requires integer discrete automatic differentiation that respects the combinatorial constraints of the CHY formalism. The algorithm learns the discrete structure of the CHY integrand space, navigating it efficiently to find solutions that precisely satisfy all specified pole requirements.

Leveraging this structure, we develop a neural-inspired algorithm that propagates constraints through the simplicial complex and enables effective bootstrapping of integrands. The algorithm bears resemblance to message-passing procedures in combinatorial neural networks and supports modular construction of integrands with higher-order poles. To validate our method, we analyze six- and eight-point examples, showing that our approach leads to more compact decompositions than traditional symmetric methods [16].

Our framework not only provides a new perspective on the CHY landscape but also establishes a paradigm for applying machine learning to fundamental physics problems. By identifying deep structural correspondences between physics and computational frameworks, we demonstrate that certain problems naturally map to specialized architectures. As the field progresses toward more complex calculations at higher multiplicities and loop orders, such interdisciplinary approaches that leverage structural insights from both physics and machine learning will likely become increasingly important.

2 Graph-Theoretic Structure of CHY Integrands

2.1 Integrand as 4-Regular Graph and Integration Rules

The CHY formalism allows for a direct translation from the algebraic form of an integrand to a graph-theoretic object. For an n -particle process, the punctures z_i are treated as vertices of a graph. For each factor of $(z_i - z_j)^{-k}$ in the denominator of the integrand, k edges are drawn between vertices i and j . For the BAS integrand, $\mathcal{I}_{\text{BAS}} = \text{PT}(\alpha)\text{PT}(\beta)$, each PT factor contributes edges between cyclically adjacent vertices in its respective ordering. Since each vertex k is connected to two neighbors in the α ordering and two neighbors in the β ordering, every vertex has exactly four edges connected to it. Such a graph, where every vertex has a degree of 4, is known as a 4-regular (or quartic) graph [11, 36–40].

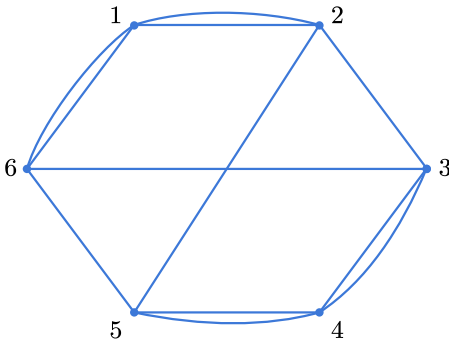


Figure 1. The 4-regular graph of integrand $\mathcal{I} = \text{PT}(123456)\text{PT}(125436)$

This graphical representation leads to a powerful set of ”integration rules,” which provide a purely combinatorial algorithm for evaluating the CHY integral without explicitly solving the scattering equations [16, 36, 39, 40]. The final amplitude is a sum over terms, each being a product of inverse Mandelstam variables, $\prod 1/s_{A_i}$. The rules determine which sets of Mandelstam variables appear.

1. **Identify Potential Poles:** For any subset of external labels $A \subset \{1, \dots, n\}$, a ”pole index” $\chi(A)$ is calculated:

$$\chi(A) := L[A] - 2(|A| - 1) \quad (2.1)$$

where $L[A]$ is the number of edges in the 4-regular graph with both endpoints in A , and $|A|$ is the number of particles in A . A Mandelstam variable s_A corresponds to a physical pole of order $\chi(A) + 1$ only if $\chi(A) \geq 0$ [36, 37]. For BAS theory, all physical poles are simple poles, corresponding to $\chi(A) = 0$.

2. **Find Compatible Sets:** A single term in the final amplitude corresponds to a valid Feynman diagram with $n - 3$ propagators. The algorithm requires finding sets of $n - 3$ distinct subsets $\{A_1, \dots, A_{n-3}\}$, each satisfying $\chi(A_i) = 0$, that are ”compatible.” Compatibility is a graph-theoretic condition ensuring that the corresponding propagators can coexist in a single cubic Feynman diagram [12].

3. **Sum Contributions:** Each compatible set contributes a term $1/(s_{A_1} \cdots s_{A_{n-3}})$ to the amplitude. The full amplitude is the sum over all such contributions [37].

For example, for a 6-point BAS amplitude with integrand $\mathcal{I} = \text{PT}(123456)\text{PT}(125436)$, one would first draw the corresponding 12-edge, 6-vertex, 4-regular graph. Then, one would identify all subsets A with $\chi(A) = 0$ (e.g., $A = \{1, 2, 6\}$) and find all compatible triplets of such subsets. The sum of the inverse products of the corresponding Mandelstam variables gives the final amplitude, matching the result from a traditional Feynman diagram calculation [36, 38, 41].

2.2 Combinatorial Structure of Generalized CHY Graphs

The graph-theoretic methods outlined for the bi-adjoint scalar (BAS) theory can be extended into a more general and powerful framework. This allows for a unified combinatorial analysis of any theory described by a rational CHY integrand.

First, we generalize the graph representation itself. To accommodate any rational function of differences $(z_i - z_j)$, we introduce two types of edges:

- A factor of $(z_i - z_j)^{-1}$ in the denominator corresponds to a **solid edge**.
- A factor of $(z_i - z_j)^{+1}$ in the numerator corresponds to a **dashed edge**.

This establishes a direct map between any rational integrand $I(z)$ and a corresponding graph with two edge types.

With this representation, we can define a local property for each vertex v , its **Net Degree**, which counts the net power of factors involving z_v in the integrand:

$$\text{deg}_{\text{net}}(v) := \text{deg}_{\text{solid}}(v) - \text{deg}_{\text{dashed}}(v) \quad (2.2)$$

This concept of a local net count can be conceptually extended to a "regional" property for any subset of vertices $A \subset \{1, \dots, n\}$. This gives rise to the **Generalized Pole Degree**, $\mathbf{K}(\mathbf{A})$, which measures the net number of internal edges within the region defined by A :

$$K(A) := L_{\text{solid}}[A] - L_{\text{dashed}}[A] \quad (2.3)$$

where $L_{\text{solid}}[A]$ and $L_{\text{dashed}}[A]$ are the number of solid and dashed edges, respectively, with both endpoints in the set A . This new degree directly relates to the original pole index $\chi(A)$ found in the literature via the simple formula:

$$\chi(A) = K(A) - 2(|A| - 1) \quad (2.4)$$

This relation elegantly separates the theory-dependent contribution to the pole structure, captured by $K(s_A)$, from the universal geometric contribution of the worldsheet, $-2(|A| - 1)$.

The true power of this framework is revealed when we consider the multiplication of integrands, as in the "double copy" construction. The multiplication of two graphs, G_α and G_β , corresponding to integrands $I_\alpha(z)$ and $I_\beta(z)$, is defined as a new graph $G_\gamma = G_\alpha * G_\beta$

corresponding to the product integrand $I_\alpha(z)I_\beta(z)$. The edge set of the product graph is the union of the edge sets of the original graphs. The index $K(s_A)$ behaves very simply under this operation.

Theorem: The $K(s_A)$ is additive under graph multiplication. *Proof:* For a product graph $G_\gamma = G_\alpha * G_\beta$, the number of internal edges in a subset A is the sum of internal edges from the constituent graphs. Thus,

$$\begin{aligned} K_\gamma(A) &:= L_{\text{solid}, \gamma}[A] - L_{\text{dashed}, \gamma}[A] \\ &= (L_{\text{solid}, \alpha}[A] + L_{\text{solid}, \beta}[A]) - (L_{\text{dashed}, \alpha}[A] + L_{\text{dashed}, \beta}[A]) \\ &= (L_{\text{solid}, \alpha}[A] - L_{\text{dashed}, \alpha}[A]) + (L_{\text{solid}, \beta}[A] - L_{\text{dashed}, \beta}[A]) \\ &= K_\alpha(A) + K_\beta(A). \quad \square \end{aligned}$$

This additivity provides a simple algebraic tool to compute the pole structure of complicated theories by summing the known indices of their simpler constituents.

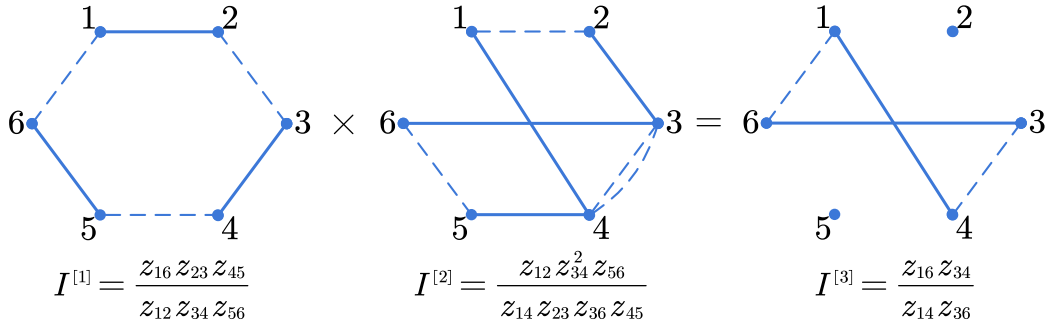


Figure 2. The "0-regular graphs" is closed under multiplication

Finally, we return to the local property of Net Degree to classify the global structure of graphs. A graph is called "n-regular" if all its vertices have a net degree of n . The additivity of the net degree under multiplication implies that the product of an m -regular and an n -regular graph is an $(m+n)$ -regular graph. This has a profound consequence: the set of "0-regular graphs" is closed under multiplication. Furthermore, one can show that this set forms a commutative group, with the empty graph ($I(z) = 1$) as the identity and graph inversion (swapping solid and dashed edges) as the inverse operation. This "0-regular group" acts as a set of transformations on other graphs; multiplying an n -regular graph by any 0-regular graph yields another n -regular graph, preserving the graph's fundamental regularity class while modifying its detailed pole structure, as tracked by $K(s_A)$.

2.3 Recursion Relation for Generalized Pole Degree $K(s_A)$

The generalized pole degree $K(s_A)$ introduced in the previous section exhibits a remarkable recursive structure that underlies the combinatorial organization of CHY integrands. This recursion provides a systematic way to compute pole degrees for arbitrary subsets of external particles from simpler building blocks.

	$I^{[1]}$	$I^{[2]}$	$I^{[3]}$		$I^{[1]}$	$I^{[2]}$	$I^{[3]}$
$deg(s_1)$	0	0	0	$K(s_{35})$	1	-1	0
$deg(s_2)$	0	0	0	$K(s_{36})$	0	0	0
$deg(s_3)$	0	0	0	$K(s_{45})$	0	1	1
$deg(s_4)$	0	0	0	$K(s_{46})$	0	0	0
$deg(s_5)$	0	0	0	$K(s_{56})$	-1	0	-1
$deg(s_6)$	0	0	0	$K(s_{123})$	0	0	0
$K(s_{12})$	1	-1	0	$K(s_{124})$	1	0	1
$K(s_{13})$	0	0	0	$K(s_{125})$	1	-1	0
$K(s_{14})$	0	1	1	$K(s_{126})$	0	-1	-1
$K(s_{15})$	0	0	0	$K(s_{134})$	1	-1	0
$K(s_{16})$	-1	0	-1	$K(s_{135})$	0	0	0
$K(s_{23})$	-1	1	0	$K(s_{136})$	-1	1	0
$K(s_{24})$	0	0	0	$K(s_{145})$	-1	2	1
$K(s_{25})$	0	0	0	$K(s_{146})$	-1	1	0
$K(s_{26})$	0	0	0	$K(s_{156})$	0	-1	-1
$K(s_{34})$	1	-2	-1				

Figure 3. The $K_{I^{[3]}}(s_A) = K_{I^{[1]}}(s_A) + K_{I^{[2]}}(s_A)$ for all poles

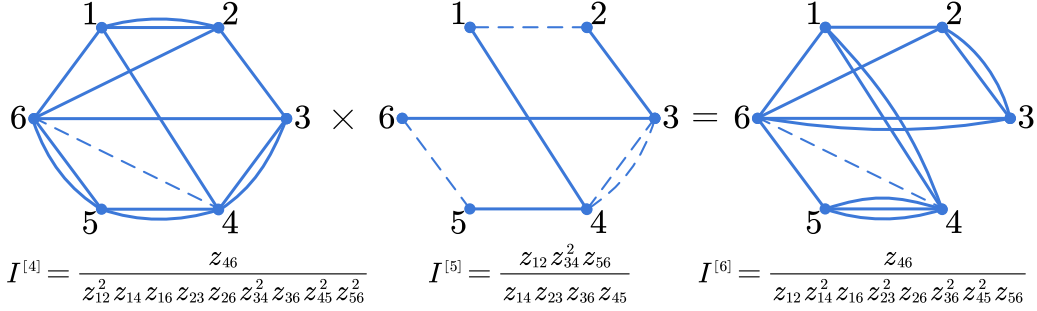


Figure 4. The "0-regular group" acts as a set of transformations on other graphs

For any non-empty subset $A \subseteq \{1, \dots, n\}$ with cardinality $|A| \geq 3$, the generalized pole degree satisfies the fundamental recursion

$$K(A) = \frac{1}{(|A| - 2)!} \sum_{\substack{B \subset A \\ |B|=|A|-1}} K(B). \quad (2.5)$$

This relation expresses the pole degree of any subset as a normalized sum over all its codimension-1 faces, revealing a hierarchical structure in the pole content of CHY integrands. The proof is given in Appendix A.

Illustrative examples.

	$I^{[4]}$	$I^{[5]}$	$I^{[6]}$		$I^{[4]}$	$I^{[5]}$	$I^{[6]}$
$deg(s_1)$	4	0	4	$K(s_{35})$	0	-1	-1
$deg(s_2)$	4	0	4	$K(s_{36})$	1	0	1
$deg(s_3)$	4	0	4	$K(s_{45})$	2	1	3
$deg(s_4)$	4	0	4	$K(s_{46})$	-1	0	-1
$deg(s_5)$	4	0	4	$K(s_{56})$	2	0	2
$deg(s_6)$	4	0	4	$K(s_{123})$	3	0	3
$K(s_{12})$	2	-1	1	$K(s_{124})$	3	0	3
$K(s_{13})$	0	0	0	$K(s_{125})$	2	-1	1
$K(s_{14})$	1	1	2	$K(s_{126})$	4	-1	3
$K(s_{15})$	0	0	0	$K(s_{134})$	3	-1	2
$K(s_{16})$	1	0	1	$K(s_{135})$	0	0	0
$K(s_{23})$	1	1	2	$K(s_{136})$	2	1	3
$K(s_{24})$	0	0	0	$K(s_{145})$	3	2	5
$K(s_{25})$	0	0	0	$K(s_{146})$	1	1	2
$K(s_{26})$	1	0	1	$K(s_{156})$	3	-1	2
$K(s_{34})$	2	-2	0				

Figure 5. The $K_{I^{[6]}}(s_A) = K_{I^{[4]}}(s_A) + K_{I^{[5]}}(s_A)$ for all poles

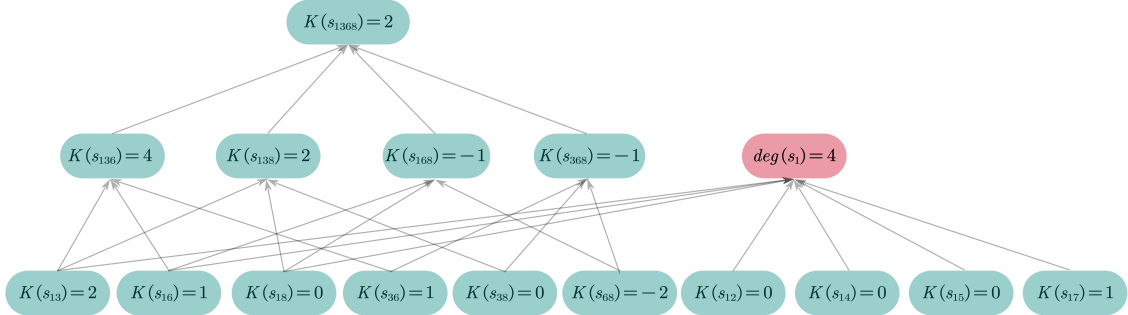


Figure 6. The recursion relation of $K(s_A)$ on $I_8 = \frac{z_{68}^2}{z_{13}^2 z_{16} z_{17} z_{24}^2 z_{28}^2 z_{35} z_{36} z_{46}^2 z_{56} z_{58}^2 z_{67} z_{78}^2}$

- **Three points.** For s_{123} the recursion reads

$$K(s_{123}) = K(s_{12}) + K(s_{13}) + K(s_{23}).$$

- **Four points.** For s_{1234} the recursion reads

$$K(s_{1234}) = \frac{K(s_{123}) + K(s_{124}) + K(s_{134}) + K(s_{234})}{2}.$$

The fundamental recursion (2.5) is a special case of a more general relation that con-

nects pole degrees at different codimensions. For any integer $1 \leq d \leq |A| - 1$, we have

$$K(A) = \frac{1}{\binom{|A|-2}{d}} \sum_{\substack{B \subset A \\ |B|=|A|-d}} K(B). \quad (2.6)$$

The case $d = 1$ recovers the original recursion (2.5). The proof is given in Appendix A.

The existence of multiple recursion relations at different codimensions provides valuable consistency checks for numerical implementations. For instance, when computing $K(12345)$, one can use: (i) $d = 1$: sum over 5 four-point values with weight $1/6$; (ii) $d = 2$: sum over 10 three-point values with weight $1/3$; (iii) $d = 3$: sum over 10 two-point values with weight 1. Each route must yield the same result, providing a powerful diagnostic for computational accuracy.

The recursive structure combined with the additivity property of $K(s_A)$ under graph multiplication reveals that the pole degrees form a graded algebraic structure. The recursion relations at different codimensions are compatible, in the sense that applying a codimension- d_1 recursion followed by a codimension- d_2 recursion yields the same result as applying a codimension- $(d_1 + d_2)$ recursion directly. This structure provides an efficient algorithm for computing the pole content of any CHY integrand constructed.

2.4 Bootstrap Equations for Integrands

The relationship between the generalized pole degree $K(s_A)$ and the pole index $\chi(A)$ established in equation (2.4) provides a powerful framework for solving the inverse CHY problem. This inverse problem asks: given a desired set of poles in a scattering amplitude, can we construct a CHY integrand that produces exactly those poles?

From equation (2.4), we know that the pole index is determined by (2.4). The fundamental principle of CHY integration rules tells us that only subsets A with $\chi(A) = 0$ contribute simple poles $1/s_A$ to the final amplitude [36, 39]. This immediately gives us a classification scheme for any subset $A \subset \{1, \dots, n\}$:

- **Physical poles:** $\chi(A) = 0 \rightarrow$ simple poles $1/s_A$ appear in the amplitude
- **Absent poles:** $\chi(A) < 0 \rightarrow$ no poles appear for these channels
- **Higher-order poles:** $\chi(A) > 0 \rightarrow$ would correspond to multiple poles, but these typically do not appear in tree-level amplitudes for generic theories

This classification leads to a key insight: for any desired amplitude with a specific pole structure, the pattern of which poles appear and which are absent constrains the possible values of $K(s_A)$. Consider a target amplitude that has simple poles for a set $\mathcal{P} = \{A_1, A_2, \dots, A_k\}$ and no poles for the complementary set $\overline{\mathcal{P}}$. The bootstrap equations are:

$$\text{For } A \in \mathcal{P} : \quad K(A) = 2(|A| - 1) \quad (2.7)$$

$$\text{For } A \in \overline{\mathcal{P}} : \quad K(A) < 2(|A| - 1) \quad (2.8)$$

The equality constraints ensure that the desired poles appear with the correct order, while the inequality constraints ensure that unwanted poles are absent.

However, the values $K(A)$ cannot be chosen arbitrarily—they must satisfy the recursion relations derived in Section 2.3. This creates a highly constrained system where the fundamental unknowns are the two-particle pole degrees $K(s_{ij})$ for all pairs $\{i, j\}$. Using the recursion relation (2.5), any higher-order pole degree can be expressed in terms of lower-order ones. For example:

$$K(s_{ijk}) = K(s_{ij}) + K(s_{ik}) + K(s_{jk}) \quad (2.9)$$

$$K(s_{ijkl}) = \frac{K(s_{ijk}) + K(s_{ijl}) + K(s_{ikl}) + K(s_{jkl})}{2} \quad (2.10)$$

Continuing this process, we can express all pole degrees $K(A)$ with $|A| \geq 3$ as linear combinations of the two-particle pole degrees $K(s_{ij})$. This reduces our bootstrap system to a set of linear constraints on the $\binom{n}{2}$ variables $\{K(s_{ij})\}_{1 \leq i < j \leq n}$.

A crucial observation is that for rational CHY integrands constructed from products of Parke-Taylor factors and their generalizations, all pole degrees $K(s_A)$ are integers. This follows from the fact that each factor $(z_i - z_j)^{\pm 1}$ contributes ± 1 to the edge count. Therefore, the bootstrap equations become a mixed system of linear Diophantine equations and inequalities:

$$\mathbf{M}_{\text{eq}} \vec{K}_2 = \vec{b}_{\text{eq}} \quad (2.11)$$

$$\mathbf{M}_{\text{ineq}} \vec{K}_2 < \vec{b}_{\text{ineq}} \quad (2.12)$$

where $\vec{K}_2 = (K(s_{12}), K(s_{13}), \dots, K(s_{n-1,n}))^T$ is the vector of two-particle pole degrees, \mathbf{M}_{eq} and \mathbf{M}_{ineq} encode the recursion relations for equality and inequality constraints respectively, while \vec{b}_{eq} and \vec{b}_{ineq} encode the corresponding target pole structures.

The bootstrap approach yields a constructive algorithm for the inverse CHY problem. The basic idea is to transform the desired pole structure into a system of linear constraints on the fundamental variables $K(s_{ij})$, solve this constrained system, and then use the additivity property under graph multiplication to construct the corresponding integrand. The algorithm proceeds in the following steps:

Algorithm 1 CHY Integrand Bootstrap Construction

Require: Target pole structure \mathcal{P} (set of desired simple poles)

Ensure: CHY integrand $I(z)$ producing amplitude with pole structure \mathcal{P}

- 1: **Input:** Specify desired pole structure $\mathcal{P} \subset \mathcal{S}_n$ where \mathcal{S}_n is the set of all possible subsets
 - 2: **Constraint Setup:** For each $A \in \mathcal{P}$, impose $K(A) = 2(|A| - 1)$
 - 3: **Constraint Setup:** For each $A \in \bar{\mathcal{P}}$, impose $K(A) < 2(|A| - 1)$
 - 4: **Recursion Matrix:** Construct matrices $\mathbf{M}_{\text{eq}}, \mathbf{M}_{\text{ineq}}$ encoding relations between $K(A)$ and $K(s_{ij})$
 - 5: **Mixed Integer System:** Formulate $\mathbf{M}_{\text{eq}} \vec{K}_2 = \vec{b}_{\text{eq}}$ and $\mathbf{M}_{\text{ineq}} \vec{K}_2 < \vec{b}_{\text{ineq}}$
 - 6: **Integer Solution:** Solve for integer vector \vec{K}_2 satisfying the mixed system
 - 7: **if** no integer solution exists **then**
 - 8: **return** "No CHY integrand exists for this pole structure"
 - 9: **end if**
 - 10: **Decomposition:** Use additivity $K_{\alpha * \beta} = K_\alpha + K_\beta$ to factor solution
 - 11: **Construction:** Build integrand $I(z) = \prod_i I_i(z)$ from elementary factors
 - 12: **return** CHY integrand $I(z)$
-

For illustration, consider a six-particle amplitude where we want simple poles for s_{12} , s_{34} , and s_{56} , but no other two-particle poles. The bootstrap equations become $K(s_{12}) = K(s_{34}) = K(s_{56}) = 0$ and $K(s_{ij}) < 0$ for all other pairs $\{i, j\}$. Combined with the recursion relations for higher-order poles, this system constrains the possible CHY integrands. One solution corresponds to the integrand $I = \frac{1}{z_{12}^2 z_{14} z_{15} z_{23} z_{26} z_{34}^2 z_{36} z_{45} z_{56}^2}$, which indeed produces poles only in the appropriate channels.

This bootstrap framework thus provides a systematic method to reverse-engineer CHY integrands from desired amplitude structures, opening new possibilities for amplitude construction and the exploration of novel theories within the CHY formalism. The method is particularly powerful because it leverages the additive structure of the generalized pole degree $K(s_A)$, allowing complex integrands to be built systematically from simpler components.

2.5 Examples of Bootstrap Construction

To illustrate the power of the bootstrap framework developed in Section 2.4, we present concrete examples demonstrating how to reverse-engineer CHY integrands from desired pole structures. These examples showcase both the computational implementation of the bootstrap algorithm and the elegant interplay between the algebraic constraints and the resulting graph structures.

Consider a six-particle amplitude where we desire simple poles for the channels s_{12} , s_{23} , s_{34} , s_{56} , s_{123} , s_{156} , s_{234} , and s_{456} . This represents a highly constrained scenario with eight simple poles, approaching the maximum possible for a six-particle amplitude.

Following the bootstrap algorithm, we first translate these requirements into con-

straints on the K-values. The equality constraints (2.7) yield:

$$K(s_{12}) = K(s_{23}) = K(s_{34}) = K(s_{56}) = 2 \quad (2.13)$$

$$K(s_{123}) = K(s_{156}) = K(s_{234}) = K(s_{456}) = 4 \quad (2.14)$$

For all other channels, the inequality constraints (2.8) require $K(s_A) < 2(|A| - 1)$. Additionally, the single-particle K-values must satisfy the regularity condition:

$$K_i = \sum_{j \neq i} K(s_{ij}) = 4 \quad \text{for all } i \in \{1, \dots, 6\} \quad (2.15)$$

This yields a mixed integer linear programming problem with 15 fundamental variables $K(s_{ij})$, subject to 14 equality constraints (8 from desired poles, 6 from single-particle conditions) and 27 inequality constraints from unwanted channels. The constraint matrix \mathbf{M}_{eq} encodes how each higher-order K-value depends on the two-particle degrees through the recursion relations. For instance, the constraint for $K(s_{123}) = 4$ translates to:

$$K(s_{12}) + K(s_{13}) + K(s_{23}) = 4 \quad (2.16)$$

The complete system of inequalities includes 27 inequality constraints (from unwanted two-particle and three-particle channels):

$$\begin{aligned} K_{1,3} < 2, K_{1,4} < 2, K_{1,5} < 2, K_{1,6} < 2, K_{2,4} < 2, K_{2,5} < 2, K_{2,6} < 2, \\ K_{3,5} < 2, K_{3,6} < 2, K_{4,5} < 2, K_{4,6} < 2, K_{1,2} + K_{1,4} + K_{2,4} < 4, \\ K_{1,2} + K_{1,5} + K_{2,5} < 4, K_{1,2} + K_{1,6} + K_{2,6} < 4, K_{1,3} + K_{1,4} + K_{3,4} < 4, \\ K_{1,3} + K_{1,5} + K_{3,5} < 4, K_{1,3} + K_{1,6} + K_{3,6} < 4, K_{1,4} + K_{1,5} + K_{4,5} < 4, \\ K_{1,4} + K_{1,6} + K_{4,6} < 4, K_{2,3} + K_{2,5} + K_{3,5} < 4, K_{2,3} + K_{2,6} + K_{3,6} < 4, \\ K_{2,4} + K_{2,5} + K_{4,5} < 4, K_{2,4} + K_{2,6} + K_{4,6} < 4, K_{2,5} + K_{2,6} + K_{5,6} < 4, \\ K_{3,4} + K_{3,5} + K_{4,5} < 4, K_{3,4} + K_{3,6} + K_{4,6} < 4, K_{3,5} + K_{3,6} + K_{5,6} < 4, \end{aligned}$$

and the complete system of 14 equality constraints (8 from desired poles, 6 from single-particle conditions):

$$\begin{aligned} K_{1,2} = 2, K_{2,3} = 2, K_{3,4} = 2, K_{5,6} = 2, K_{1,2} + K_{1,3} + K_{2,3} = 4, \\ K_{1,5} + K_{1,6} + K_{5,6} = 4, K_{4,5} + K_{4,6} + K_{5,6} = 4, K_{2,3} + K_{2,4} + K_{3,4} = 4, \\ K_1 = K_{1,2} + K_{1,3} + K_{1,4} + K_{1,5} + K_{1,6} = 4, \\ K_2 = K_{1,2} + K_{2,3} + K_{2,4} + K_{2,5} + K_{2,6} = 4, \\ K_3 = K_{1,3} + K_{2,3} + K_{3,4} + K_{3,5} + K_{3,6} = 4, \\ K_4 = K_{1,4} + K_{2,4} + K_{3,4} + K_{4,5} + K_{4,6} = 4, \\ K_5 = K_{1,5} + K_{2,5} + K_{3,5} + K_{4,5} + K_{5,6} = 4, \\ K_6 = K_{1,6} + K_{2,6} + K_{3,6} + K_{4,6} + K_{5,6} = 4. \end{aligned}$$

Solving this system yields the unique integer solution:

$$\begin{aligned}
K_{1,2} &\rightarrow 2, & K_{1,3} &\rightarrow 0, & K_{1,4} &\rightarrow 0, \\
K_{2,3} &\rightarrow 2, & K_{2,4} &\rightarrow 0, & K_{2,5} &\rightarrow 0, \\
K_{2,6} &\rightarrow 0, & K_{3,4} &\rightarrow 2, & K_{3,5} &\rightarrow 0, \\
K_{3,6} &\rightarrow 0, & K_{4,5} &\rightarrow 1, & K_{4,6} &\rightarrow 1, \\
K_{5,6} &\rightarrow 2, & K_{1,5} &\rightarrow 1, & K_{1,6} &\rightarrow 1
\end{aligned}
\tag{2.17}$$

The resulting CHY integrand:

$$I_6 = \frac{1}{z_{12}^2 z_{15} z_{16} z_{23}^2 z_{34}^2 z_{45} z_{46} z_{56}^2}
\tag{2.18}$$

demonstrates that the bootstrap construction successfully produces an integrand with precisely the desired pole structure. The resulting integrand I_6 generates an amplitude whose only simple poles are s_{12} , s_{23} , s_{34} , s_{56} , s_{123} , s_{156} , s_{234} , and s_{456} , exactly as specified in our requirements. The K-values directly translate to the powers in the integrand: each $K(s_{ij}) = 2$ yields a factor z_{ij}^{-2} in the denominator, while $K(s_{ij}) = 1$ gives z_{ij}^{-1} , and $K(s_{ij}) = 0$ means the corresponding factor is absent.

For this particular example, the mixed integer linear programming problem yields a unique solution, making it an ideal illustration of the bootstrap method. The constraint system can be solved using standard integer programming packages available in Mathematica (through functions like `LinearProgramming` with integer constraints) or Python (using libraries such as `cvxpy`, `PuLP`, or `scipy.optimize.milp`). These computational tools efficiently handle the combinatorial nature of finding integer solutions to our linear constraint system. More complex examples with non-unique solutions and detailed computational methods for solving the bootstrap equations are presented in Appendix B.

The graph-theoretic framework developed in this section has revealed the deep combinatorial structure underlying CHY integrands. Starting from the observation that integrands can be represented as generalized graphs with solid and dashed edges, we discovered three fundamental principles:

Additive Structure: The generalized pole degree $K(s_A)$ is additive under integrand multiplication, leading to a group structure on 0-regular graphs that acts transitively on integrand spaces. This algebraic property transforms the complex problem of integrand multiplication into simple integer addition.

Recursive Organization: The pole degrees satisfy elegant recursion relations that encode the full pole structure in the two-particle data.

Bootstrap Construction: The inverse problem—constructing integrands from desired poles—reduces to integer linear programming, providing a systematic approach to exploring new theories within the CHY framework and guaranteeing the existence and uniqueness of solutions for compatible pole structures.

These algebraic and combinatorial insights suggest a natural extension to higher-dimensional structures. The recursion relations, which connect pole degrees across different particle subsets, hint at an underlying topological organization where the pole hierarchy

can be viewed as a simplicial complex. This perspective may offer additional mathematical tools for understanding the CHY formalism.

The discrete optimization problems arising from the bootstrap construction also suggest potential connections to computational methods from combinatorial optimization and machine learning. In particular, algorithms designed for discrete structures on graphs and simplicial complexes could potentially be adapted to address computational challenges in amplitude calculations.

In the next section, we explore this topological perspective more systematically. By viewing the pole structure as a simplicial complex rather than just a graph, we uncover additional mathematical structure that provides both theoretical insights and practical algorithms for the pole selection problem. This approach connects the CHY formalism to recent developments in topological data analysis and suggests new computational strategies for working with multi-particle amplitudes.

3 From Poles to Simplices: A Topological Perspective

3.1 Simplicial Structure in CHY Pole Hierarchies

The pole structure of CHY integrands exhibits a natural hierarchical organization that goes beyond the graph-theoretic framework presented in Section 2. This hierarchy is most clearly revealed when we consider the partial ordering of particle subsets by inclusion, which forms a Hasse diagram structure that is intimately connected to simplicial complexes. Consider the collection of all subsets $A \subseteq 1, \dots, n$ ordered by inclusion. For each subset A , we have the pole index $\chi(A) = K(A) - 2(|A| - 1)$ determining whether s_A appears as a pole in the amplitude. The recursion relations (2.5) and (2.6) show that the pole degree $K(A)$ of any subset is completely determined by the pole degrees of its proper subsets. This creates a layered structure where:

This layered Hasse diagram naturally corresponds to the face poset of a simplicial complex. Specifically, if we identify each subset A with a $(|A| - 1)$ -simplex σ_A , then the inclusion relation $B \subset A$ corresponds to the face relation $\sigma_B \prec \sigma_A$. The recursion relation (2.5) can then be reinterpreted as stating that the weight of a simplex is determined by the weights of its codimension-1 faces:

$$K(\sigma) = \frac{1}{(\dim(\sigma) - 1)!} \sum_{\tau \prec_1 \sigma} K(\tau) \quad (3.1)$$

where $\tau \prec_1 \sigma$ denotes that τ is a codimension-1 face of σ . This simplicial perspective transforms the CHY pole structure into a topological data type. The physical poles ($\chi(A) = 0$) form a subcomplex, while the absent poles ($\chi(A) < 0$) and the forbidden higher-order poles ($\chi(A) > 0$) partition the remaining simplices. The bootstrap equations (2.7)-(2.8) become constraints on which simplices can appear in the "physical subcomplex." The passage from graphs to simplicial complexes also enables us to apply tools from combinatorial Hodge theory. Define the space of k -chains C_k as formal linear combinations of k -simplices, with the boundary operator $\partial_k : C_k \rightarrow C_{k-1}$ given by the standard alternating sum over faces. The pole degree function K extends to a cochain $K \in C^*$, and the recursion relations imply a cohomological structure:

$$\delta K = \Omega \quad (3.2)$$

where δ is the coboundary operator and Ω encodes the deviations from the naive dimensional counting. This reveals that the pole structure has both a "local" contribution (from the coboundary) and a "harmonic" contribution (from the kernel of the Laplacian $\Delta = \delta\partial + \partial\delta$). Furthermore, the multiplicative structure of CHY integrands under the double-copy construction translates into operations on simplicial complexes. The additivity of $K(A)$ under graph multiplication (Theorem in Section 2.3) extends to a functorial relationship between simplicial complexes, where the product of integrands corresponds to a fiber product of the associated complexes with weights adding fiberwise. This topological perspective provides powerful new tools for analyzing CHY integrands:

Persistent homology can track how the pole structure changes under deformations. Spectral sequences can organize the computation of amplitudes. Sheaf cohomology can capture global constraints on consistent pole configurations.

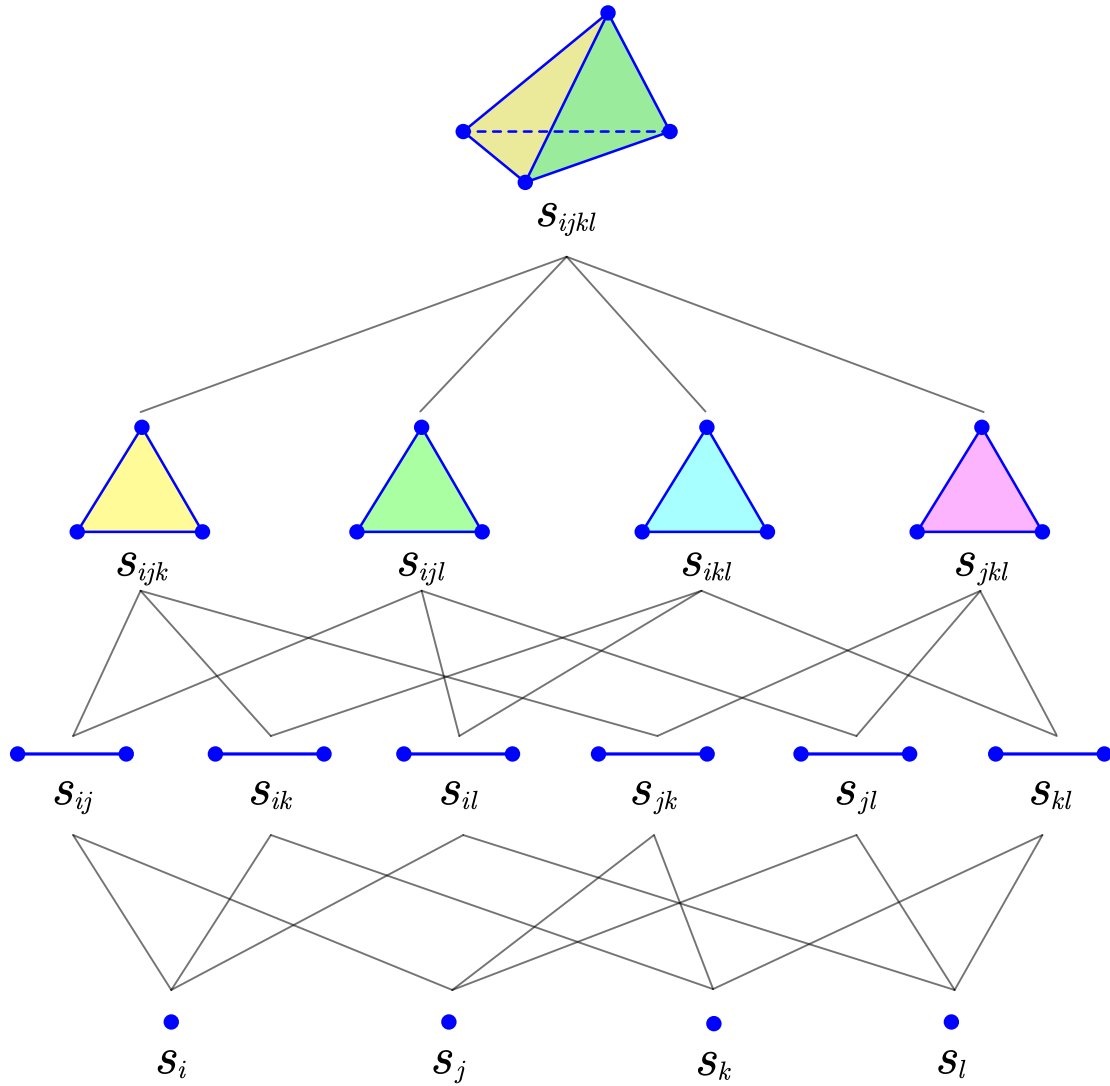


Figure 7. Simplicial Structure: Layer 0: Single particles (vertices), Layer 1: Two-particle channels (edges), Layer 2: Three-particle channels (triangles), ..., Layer k : $(k + 1)$ -particle channels (k -simplices)

The simplicial structure naturally suggests the use of Combinatorial Neural Networks (CNNs), a class of neural architectures designed to operate on higher-order topological structures beyond graphs [35, 42]. Unlike traditional Graph Neural Networks (GNNs) that are limited by the Weisfeiler-Lehman hierarchy [43, 44], CNNs can process information across all dimensions of the simplicial complex simultaneously. This is particularly relevant for CHY integrands, where the pole structure involves intricate relationships among multi-particle channels that cannot be captured by pairwise interactions alone.

Recent developments in topological deep learning [45, 46] and geometric machine learning on simplicial complexes [47, 48] provide the theoretical foundation for these approaches.

The ability of CNNs to perform message passing along both boundary and coboundary relations, and to aggregate information hierarchically across different dimensions, makes them a natural computational framework for the recursive pole structures we have identified. The CHY formalism, with its rich combinatorial and topological structure, presents an ideal testing ground for these emerging methods at the intersection of algebraic topology and deep learning.

In the following sections, we will develop this correspondence in detail, showing how the combinatorial and topological structures work together with modern machine learning techniques to provide both theoretical insights and practical computational advantages for the CHY formalism.

3.2 Combinatorial Neural Networks and Discrete Automatic Differentiation

The topological perspective developed in Section 3 naturally leads us to consider computational frameworks that can efficiently handle the hierarchical pole structures of CHY integrands. While traditional Graph Neural Networks (GNNs) have revolutionized many areas of physics [49], they are fundamentally limited to pairwise interactions and cannot capture the higher-order relationships inherent in simplicial complexes [50, 51]. This is where Combinatorial Neural Networks (CNNs) and automatic differentiation techniques become essential tools for the CHY formalism.

A crucial observation is that the pole adjustment algorithm operates on *discrete* structures—the K-values are integers, and the operations involve discrete increments and decrements. This is fundamentally different from the continuous automatic differentiation implemented in popular frameworks like TensorFlow, PyTorch, or JAX [52–54]. Current frameworks are designed for continuous optimization and lack native support for:

- Integer-valued gradients and discrete optimization
- Topological constraints on simplicial complexes
- Exact satisfaction of linear Diophantine equations

The discrete nature of our problem requires a specialized automatic differentiation framework that can handle:

$$\frac{\partial K(s_A)}{\partial K(s_{ij})} \in \mathbb{Z} \quad (3.3)$$

where the "derivatives" are actually sensitivity coefficients derived from the recursion relations (2.5).

For a k -simplex σ in our pole hierarchy, the CNN update rule takes the form [35]:

$$h_\sigma^{(t+1)} = \phi \left(h_\sigma^{(t)}, \bigoplus_{\tau \in \mathcal{B}(\sigma)} m_{\tau \rightarrow \sigma}^{(t)}, \bigoplus_{\tau \in \mathcal{C}(\sigma)} m_{\tau \rightarrow \sigma}^{(t)} \right) \quad (3.4)$$

where $\mathcal{B}(\sigma)$ denotes the boundary (codimension-1 faces) and $\mathcal{C}(\sigma)$ denotes the coboundary (simplices containing σ). This bidirectional information flow perfectly mirrors the upward and downward propagation we observe in the pole adjustment algorithm.

Algorithm 2 PropagateUpdate: Discrete Automatic Differentiation

Require: Graph G , modified pole s_A , change ΔK , fixed poles \mathcal{F}

Ensure: Updated K-values satisfying all constraints

```
1: Queue  $Q \leftarrow \{s_A\}$ , Visited  $V \leftarrow \emptyset$ 
2: while  $Q \neq \emptyset$  do
3:    $s_B \leftarrow$  call DEQUEUE( $Q$ )
4:   if  $s_B \in V$  then
5:     continue
6:   end if
7:    $V \leftarrow V \cup \{s_B\}$ 
8:   {Upward propagation to supersets}
9:   for each superset  $s_C \supset s_B$  with  $|s_C| = |s_B| + 1$  do
10:    if  $s_C \notin \mathcal{F}$  then
11:       $\Delta K_C \leftarrow \Delta K / (|s_B| - 1)!$ 
12:       $K^*(s_C) \leftarrow K^*(s_C) + \Delta K_C$ 
13:      call ENQUEUE( $Q, s_C$ )
14:    else
15:      {Fixed point encountered, trigger backpropagation}
16:      call BACKPROPAGATE( $G, s_B, s_C, \Delta K, \mathcal{F}$ )
17:    end if
18:  end for
19:  {Backward propagation to subsets (if from higher layer)}
20:  if  $|s_B| > 2$  then
21:    for each subset  $s_D \subset s_B$  with  $|s_D| = |s_B| - 1$  do
22:      if  $s_D \notin \mathcal{F}$  then
23:        Select one  $s_D$  and update (choice based on constraints)
24:         $K^*(s_D) \leftarrow K^*(s_D) + \Delta K$ 
25:        call ENQUEUE( $Q, s_D$ )
26:      end if
27:    end for
28:  end if
29: end while
```

The key insight is that our "gradients" are actually linear relationships derived from the recursion relations. For any modification $\Delta K(s_{ij})$ to a two-point pole, the change propagates through the hierarchy according to:

$$\Delta K(s_A) = \sum_{\substack{i,j \in A \\ i < j}} c_{A,ij} \Delta K(s_{ij}) \quad (3.5)$$

where the coefficients $c_{A,ij} \in \mathbb{Q}$ are determined by the combinatorial structure of the simplex.

The training process for this specialized CNN architecture proceeds through two fundamental phases that work together to maintain the consistency of the pole hierarchy:

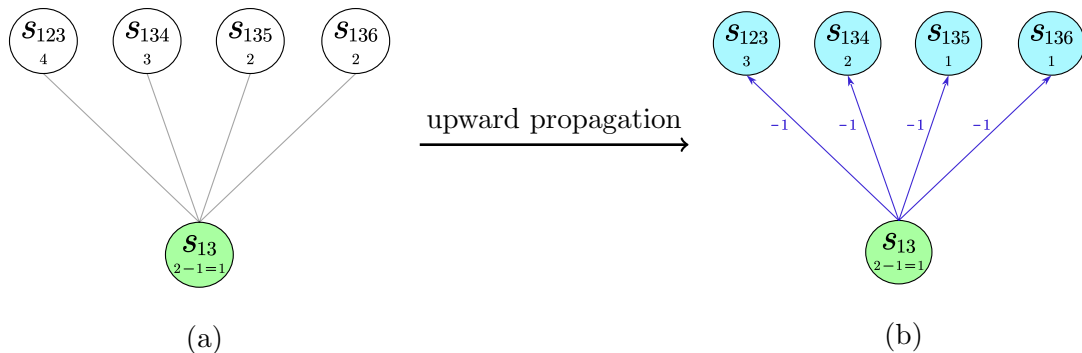


Figure 8. Upward propagation in the discrete automatic differentiation algorithm. (a) Initial configuration showing the two-particle pole s_{13} with $K(s_{13}) = 2$ being decremented by 1 (green node). The gray edges represent the dependency relationships from the recursion relation $K(s_{ABC}) = K(s_{AB}) + K(s_{AC}) + K(s_{BC})$. (b) After applying $\Delta K = -1$ to s_{13} , the change propagates upward to all three-particle supersets containing particles 1 and 3. Each superset $\{s_{123}, s_{134}, s_{135}, s_{136}\}$ receives an update of -1 (shown as blue edges with -1 labels), maintaining the recursion relations. The updated values are shown in cyan nodes.

1. Upward Propagation Update: When we modify a pole degree $K(s_A)$ by an integer amount ΔK , this change must propagate upward through the hierarchy to all supersets to maintain the recursion relations. As illustrated in Figure 8, the algorithm systematically updates all affected higher-order poles according to the formula:

$$K(s_B) \leftarrow K(s_B) + \frac{\Delta K}{(|A| - 1)!} \quad \text{for all } B \supset A \text{ with } |B| = |A| + 1 \quad (3.6)$$

2. Backward Propagation (Triggered by Fixed Nodes): When the upward propagation encounters a fixed pole—one whose value must remain constant due to physical constraints—the algorithm triggers a backward propagation phase. As shown in Figure 9, this phase redistributes the constraints by selecting appropriate subsets and adjusting their values to compensate for the fixed constraint while maintaining all recursion relations.

These two processes continue alternating until the Combinatorial Neural Network reaches a stable configuration where all constraints are satisfied. At convergence, we extract the bottom layer K-values (the two-particle pole degrees $\{K(s_{ij})\}$), which completely determine the CHY integrand through:

$$I(z) = \prod_{1 \leq i < j \leq n} (z_i - z_j)^{-K(s_{ij})} \quad (3.7)$$

This discrete automatic differentiation ensures:

- All K-values remain integers (when changes are properly scaled)
- Recursion relations are exactly satisfied at each step
- Fixed poles maintain their values throughout propagation

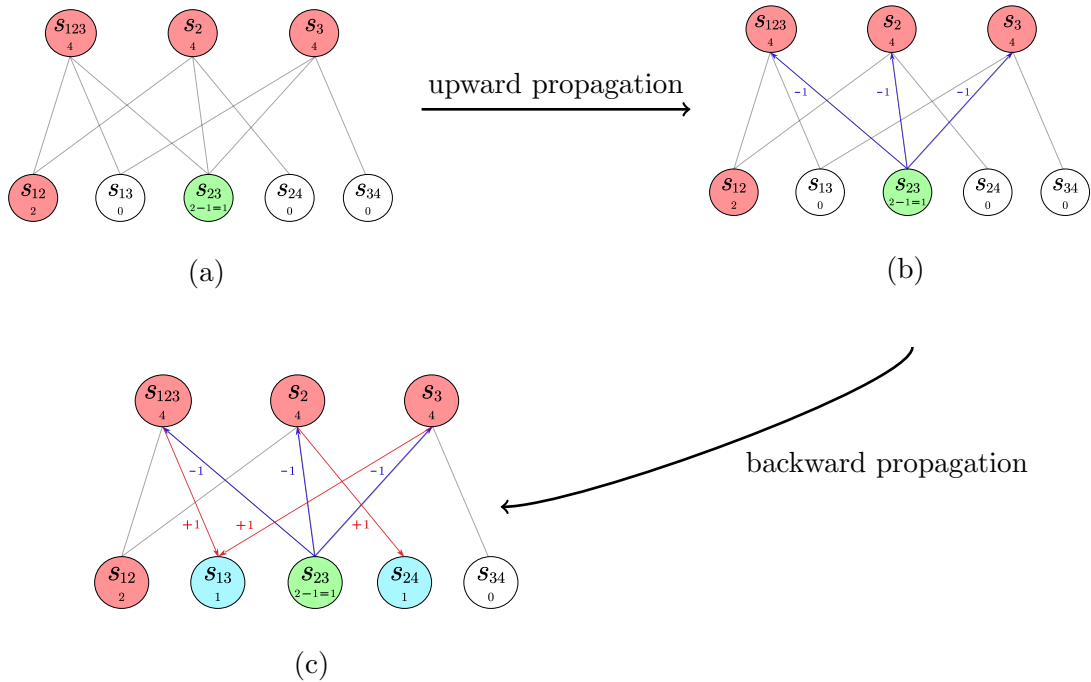


Figure 9. Backward propagation triggered by fixed constraints in the pole hierarchy. (a) Initial state with fixed poles s_{12} , s_{123} , s_2 , and s_3 (red nodes) that must maintain their values throughout the algorithm. The pole s_{23} (green) is to be decremented by 1. (b) Upward propagation attempts to update the three-particle poles, but encounters the fixed constraint at s_{123} (and implicitly at single-particle nodes s_2 and s_3). (c) Backward propagation is triggered to maintain consistency: to compensate for the inability to modify fixed nodes, the algorithm selects s_{13} (intersection of subsets from s_{123} and supersets of s_3) and s_{24} (superset of s_2), incrementing each by $+1$ (red edges). This redistribution ensures all recursion relations remain satisfied while respecting the fixed constraints.

The backpropagation step, triggered when encountering fixed points, implements a discrete version of the chain rule that respects the topological constraints of the simplicial complex. This is fundamentally different from continuous backpropagation and requires specialized algorithms not found in current deep learning frameworks [55].

The examples in the following sections serve both as validation of the algorithm and as intuitive illustrations of how discrete automatic differentiation operates on the CHY pole hierarchy.

3.3 Neural-Inspired Pick-Pole Algorithm

The computational framework developed in Section 3.2, combining Combinatorial Neural Networks with discrete automatic differentiation, provides the essential infrastructure for implementing the pole selection algorithm. We now turn to the central computational challenge in the CHY formalism: isolating specific physical singularities from the complete amplitude structure.

The pick-pole algorithm addresses a fundamental problem in the practical application of the CHY formalism [13, 14]. Given a CHY integrand $I(z)$ that produces an amplitude

with multiple poles, we often need to isolate contributions containing a specific pole $1/s_A$ where $s_A = (\sum_{i \in A} k_i)^2$. This capability is essential for analyzing the analytic structure of amplitudes, studying factorization limits when particles become collinear or soft, and constructing loop-level integrands from tree-level data via forward limits and unitarity cuts [9, 10].

For the bi-adjoint scalar theory, where the integrand takes the form $I[\pi|\rho] = \text{PT}(\pi) \times \text{PT}(\rho)$, the algorithm is elegant and provably correct [36, 56]. The key insight is that a pole s_A appears if and only if the set A forms a contiguous block in both orderings π and ρ . One can then multiply by an appropriate cross-ratio factor to eliminate unwanted contributions:

$$\mathcal{P}_{bd}^{ac} = \frac{z_{ac}z_{bd}}{z_{ad}z_{cb}} \quad (3.8)$$

where a, b are the endpoints of the contiguous set A and c, d are their nearest neighbors in the complement \bar{A} [57].

For more general CHY integrands, particularly those associated with labelled tree graphs [15], the notion of ‘‘contiguity’’ loses meaning, and the algorithm becomes significantly more complex. As noted in [57], the current approach is fundamentally heuristic, relying on a generate-and-test search through combinations of cross-ratio factors. This heuristic method, while powerful enough to construct the first universal one-loop CHY integrand for BAS theory [14], suffers from exponential computational complexity and lacks a rigorous proof of correctness.

Our approach reformulates this challenge within the graph-theoretic and topological framework developed in previous sections. The key insight is that pole selection corresponds to a systematic adjustment of K-values while maintaining all recursion relations and fixed-point constraints. Rather than searching through combinations of cross-ratio factors, we directly manipulate the underlying graph structure through controlled modifications of the generalized pole degrees.

Algorithm 3 Pick-Pole Algorithm for CHY Integrands

Require: CHY integrand $I(z)$ with pole structure, target pole s_T to retain

Ensure: Modified integrand $I^*(z)$ containing only terms with pole s_T

- 1: **Initialize:** Construct pole hierarchy graph G with K-values from $I(z)$
 - 2: **Identify:** Mark poles to retain $\mathcal{P}_{\text{retain}} = \{s_T\} \cup \text{CompatiblePoles}(s_T)$
 - 3: **Identify:** Mark poles to remove $\mathcal{P}_{\text{remove}} = \text{AllPoles}(I) \setminus \mathcal{P}_{\text{retain}}$
 - 4: **for** each pole $s_A \in \mathcal{P}_{\text{remove}}$ **do**
 - 5: $K^*(s_A) \leftarrow K(s_A) - 1$ {Decrement K-value}
 - 6: **call** PROPAGATEUPDATE($G, s_A, -1, \mathcal{P}_{\text{retain}}$)
 - 7: **end for**
 - 8: **return** Integrand $I^*(z)$ constructed from modified K-values
-

The algorithm’s correctness relies on several key properties established in previous sections. The additivity of K-values (Theorem in Section 2.2) ensures that modifications propagate correctly through the graph structure. The recursion relations (2.5)-(2.6) main-

tain consistency across different levels of the pole hierarchy. Most critically, the discrete automatic differentiation framework embodied in the `PropagateUpdate` subroutine (Algorithm 2) ensures that all constraints are satisfied throughout the modification process.

The connection to the topological perspective is particularly illuminating. Pole selection can be viewed as a projection operation on the simplicial complex, where we retain only those simplices (poles) compatible with our target. This geometric interpretation provides both intuition and a correctness criterion: the resulting integrand must correspond to a valid subcomplex of the original pole structure. The discrete nature of our approach—working with integer-valued K-degrees and exact constraint satisfaction—distinguishes it fundamentally from continuous optimization methods and ensures that the output is always a valid CHY integrand.

The following sections demonstrate the algorithm’s effectiveness through explicit examples, showing how it successfully isolates desired pole structures in both six-point and eight-point amplitudes. These examples serve not only as validation of the method but also as pedagogical illustrations of how the discrete automatic differentiation operates on the hierarchical pole structure of CHY integrands.

3.4 Examples of 6-Point CHY Integrands

We demonstrate the neural-inspired pick-pole algorithm through a concrete 6-point example. The algorithm operates on discrete structures where K-values are integers, and the pole hierarchy forms a two-layer network structure that enables systematic pole selection through discrete automatic differentiation.

For any subset $A \subset \{1, 2, \dots, n\}$, we define the K-value as:

$$K(s_A) := L[A]$$

Consider a six-point CHY integrand:

$$I_6 = \frac{1}{z_{12}^2 z_{23}^2 z_{34}^2 z_{56}^2 z_{16} z_{45} z_{46} z_{15}}$$

which produces five cubic Feynman diagrams:

$$\frac{1}{s_{12}s_{34}s_{56}} + \frac{1}{s_{123}s_{12}s_{56}} + \frac{1}{s_{123}s_{23}s_{56}} + \frac{1}{s_{156}s_{23}s_{56}} + \frac{1}{s_{156}s_{34}s_{56}}$$

To pick pole s_{12} , we need to retain poles s_{12} , s_{34} , s_{56} and s_{123} while removing poles s_{23} and s_{156} .

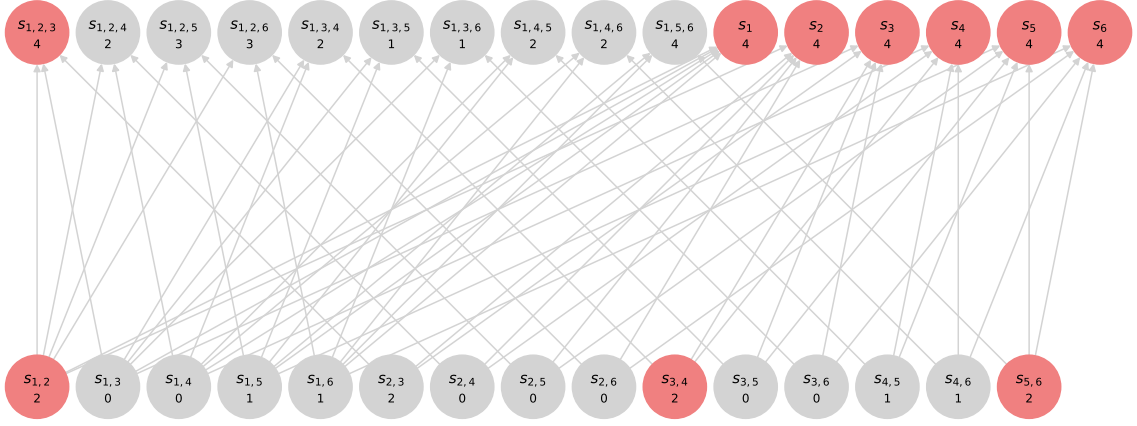


Figure 10. Initial pole hierarchy for 6-point CHY integrand : Two-layer network structure with two-particle poles in the first layer (bottom), single-particle and three-particle poles in the second layer (top). Gray edges represent dependency relationships from recursion relation $K(s_{abc}) = K(s_{ab}) + K(s_{ac}) + K(s_{bc})$ and $deg(s_a) = K(s_{ab}) + K(s_{ac}) + K(s_{ad}) + K(s_{ae}) + K(s_{af})$. Red nodes indicate fixed poles that must be preserved during the algorithm.

The recursion relations defining the pole hierarchy are:

$$K(s_{abc}) = K(s_{ab}) + K(s_{ac}) + K(s_{bc})$$

$$deg(s_a) = K(s_{ab}) + K(s_{ac}) + K(s_{ad}) + K(s_{ae}) + K(s_{af})$$

We fix the K-values of desired poles:

$$K(s_{12}) = 2, \quad K(s_{34}) = 2, \quad K(s_{56}) = 2, \quad K(s_{123}) = 4$$

Step 1: Remove pole s_{23}

We decrement the K-value of the unwanted pole s_{23} :

$$K^*(s_{23}) = K(s_{23}) - 1 = 1$$

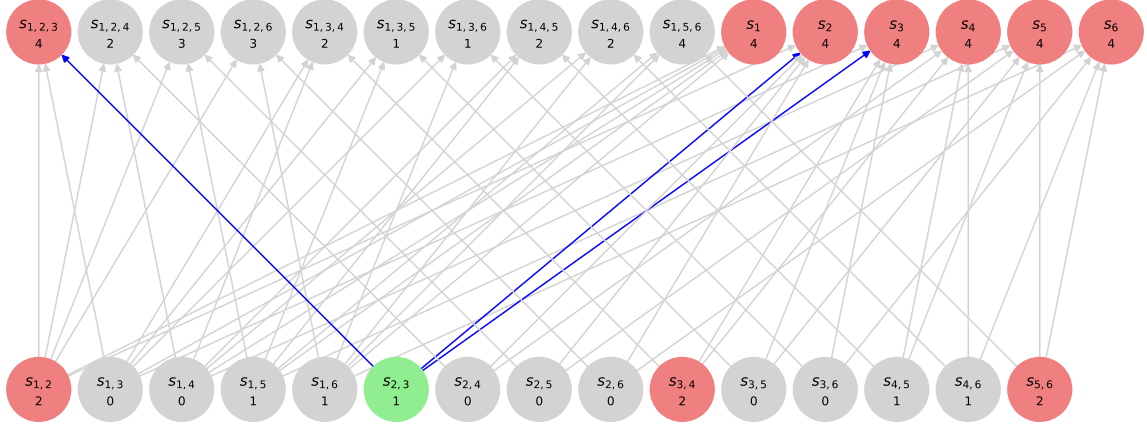


Figure 11. First upward propagation : The modification $\Delta K = -1$ at pole s_{23} (green node) propagates upward through the network hierarchy. Blue arrows show the upward propagation paths to single-particle subsets and three-particle supersets. The algorithm encounters fixed constraints at s_{123} , s_2 , and s_3 (red nodes), triggering the backward propagation mechanism.

The upward propagation encounters fixed points s_{123} , s_2 , and s_3 , triggering backward propagation.

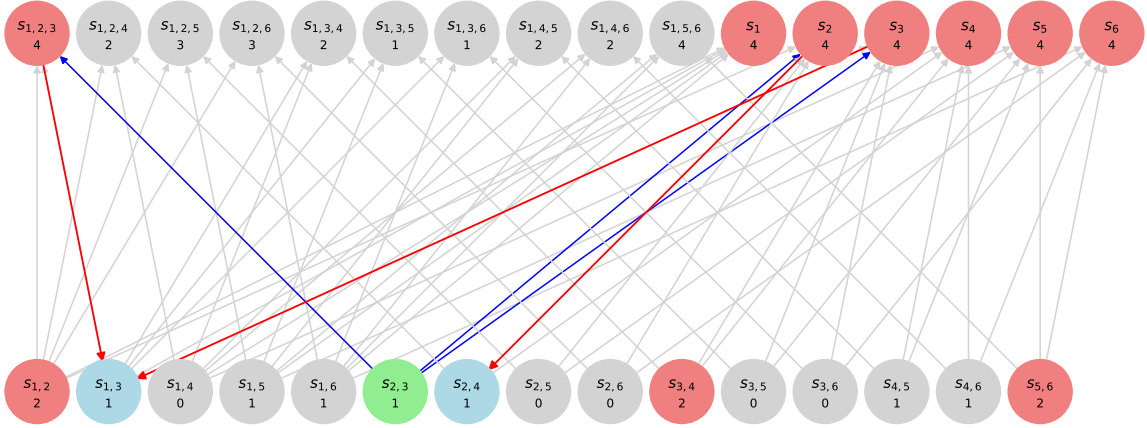


Figure 12. First backward propagation : When upward propagation hits fixed constraints, the discrete automatic differentiation algorithm redistributes the changes through backward propagation (red arrows). The algorithm selects intersection s_{13} and superset s_{24} , incrementing their K-values by +1 to maintain all recursion relations while respecting fixed constraints.

The algorithm compensates by selecting appropriate poles:

$$K^*(s_{13}) = K(s_{13}) + 1 = 1, \quad K^*(s_{24}) = K(s_{24}) + 1 = 1$$

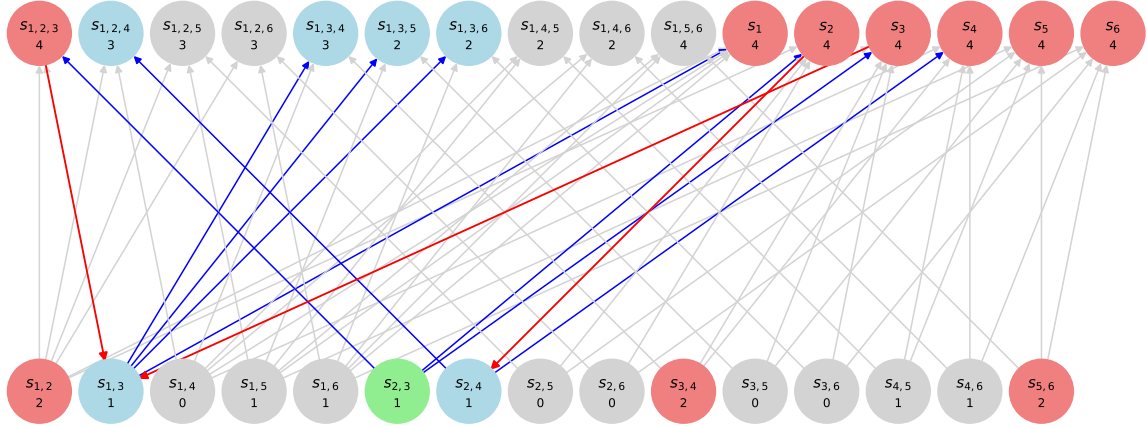


Figure 13. Second upward propagation : The changes at s_{13} and s_{24} propagate upward (blue arrows), updating their three-particle supersets s_{134} , s_{135} , s_{136} and s_{124} by $+1$. The propagation again encounters fixed points s_1 and s_4 , necessitating another round of backward propagation.

The upward propagation again encounters fixed points s_1 and s_4 .

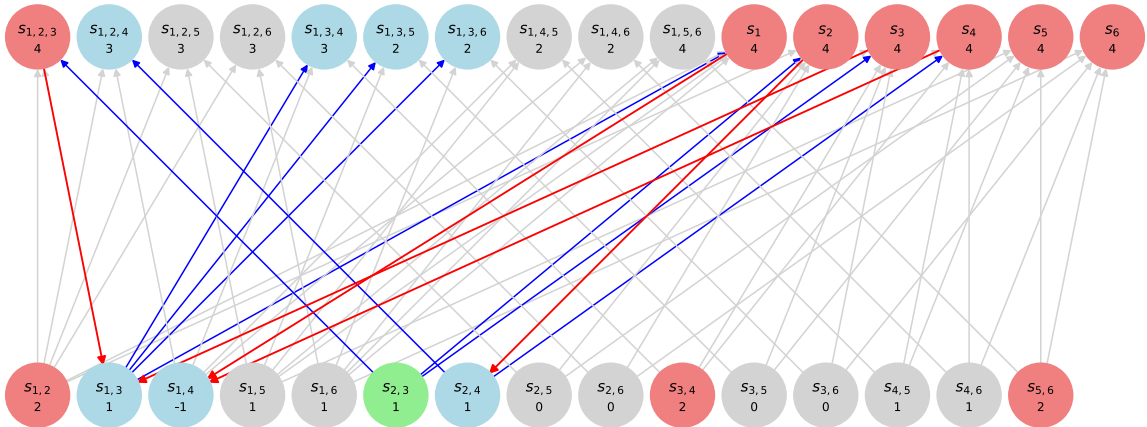


Figure 14. Second backward propagation : To maintain consistency with fixed single-particle constraints, the algorithm performs backward propagation from the second layer to the first layer (red arrows). The intersection s_{14} of dependent supersets from fixed nodes s_1 and s_4 is decremented by -1 , ensuring all recursion relations remain satisfied.

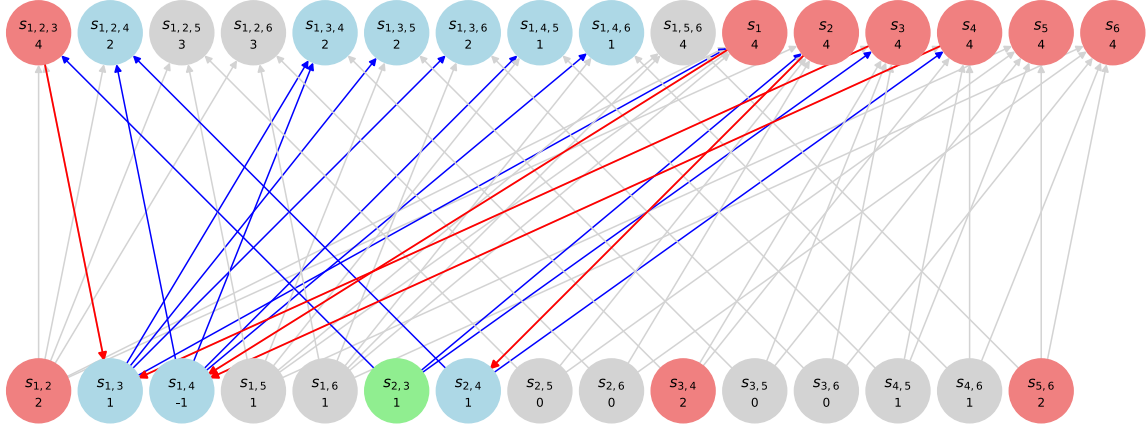


Figure 15. Final upward propagation for s_{23} removal : The third upward propagation completes without encountering additional fixed points, indicating successful convergence of the discrete automatic differentiation algorithm. The removal of pole s_{23} is now complete with all constraints satisfied.

The algorithm terminates when no fixed points are encountered, completing the removal of pole s_{23} .

Step 2: Remove pole s_{156}

We now repeat the procedure to remove pole s_{156} .

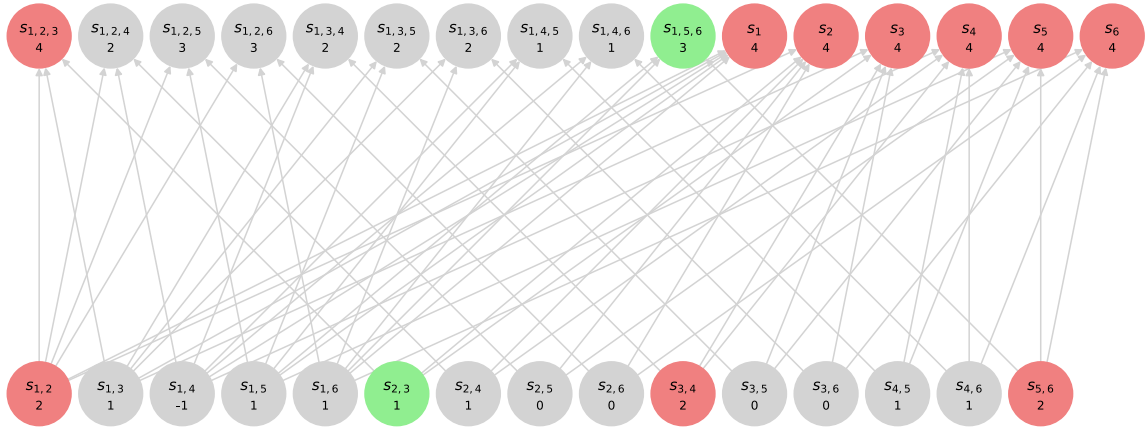


Figure 16. Updated pole hierarchy for s_{156} removal : The network structure after removing s_{23} , showing updated K-values throughout the hierarchy. Fixed points (red) and the target pole s_{156} for removal (green) are clearly marked. The algorithm now proceeds to remove the second unwanted pole while maintaining all established constraints.

We decrement the K-value of pole s_{156} :

$$K^*(s_{156}) = K(s_{156}) - 1 = 3$$

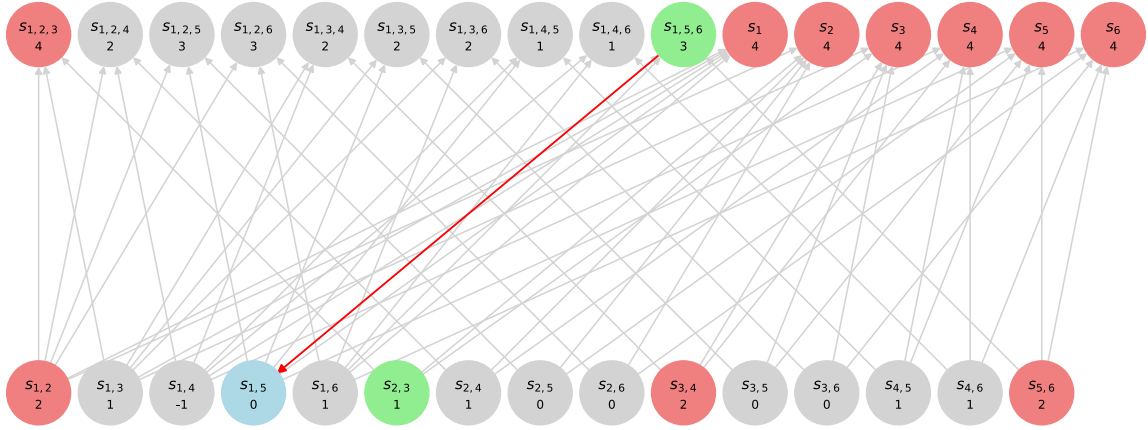


Figure 17. Downward propagation : Unlike the previous case, the modification at three-particle pole s_{156} requires downward propagation to the first layer (red arrows). The algorithm selects subset s_{15} and decrements its K-value by -1, demonstrating the bidirectional nature of the discrete automatic differentiation framework.

The downward propagation selects subset s_{15} for modification.

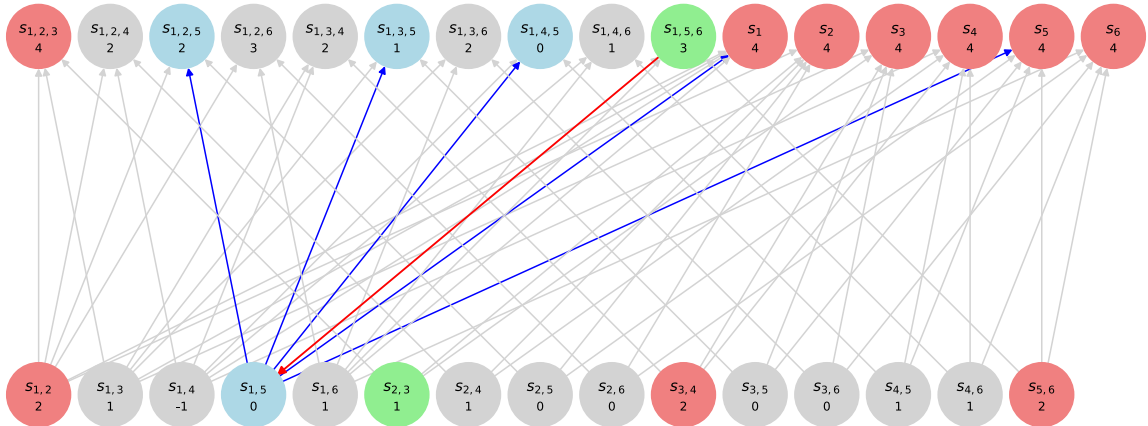


Figure 18. Upward propagation from s_{15} : The change at s_{15} propagates upward (blue arrows) to its three-particle supersets s_{125} , s_{135} , and s_{145} , each decremented by -1. Fixed points s_1 and s_5 are encountered, triggering backward propagation to maintain network consistency.

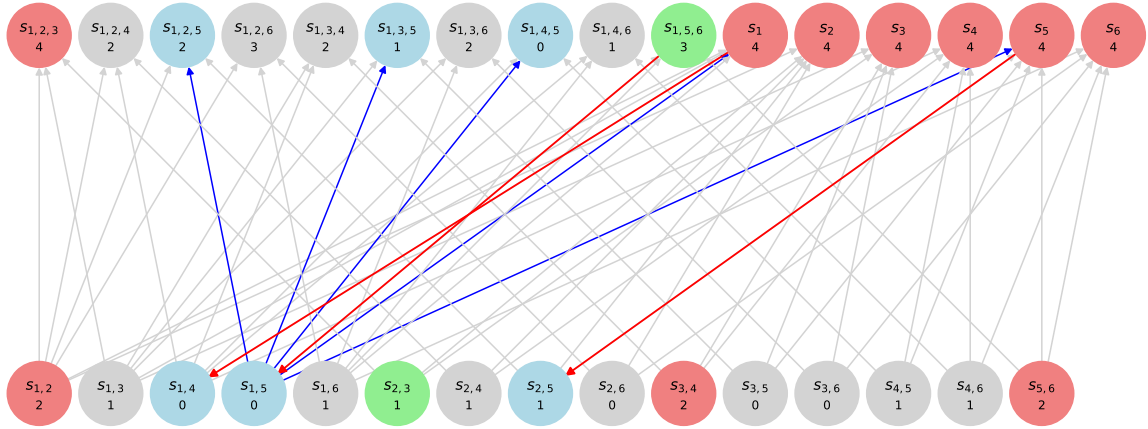


Figure 19. Backward propagation for fixed constraints : The algorithm redistributes changes through backward propagation (red arrows), selecting supersets s_{14} and s_{25} of fixed points s_1 and s_5 respectively. Each is incremented by $+1$ to compensate for the inability to modify the fixed single-particle poles.

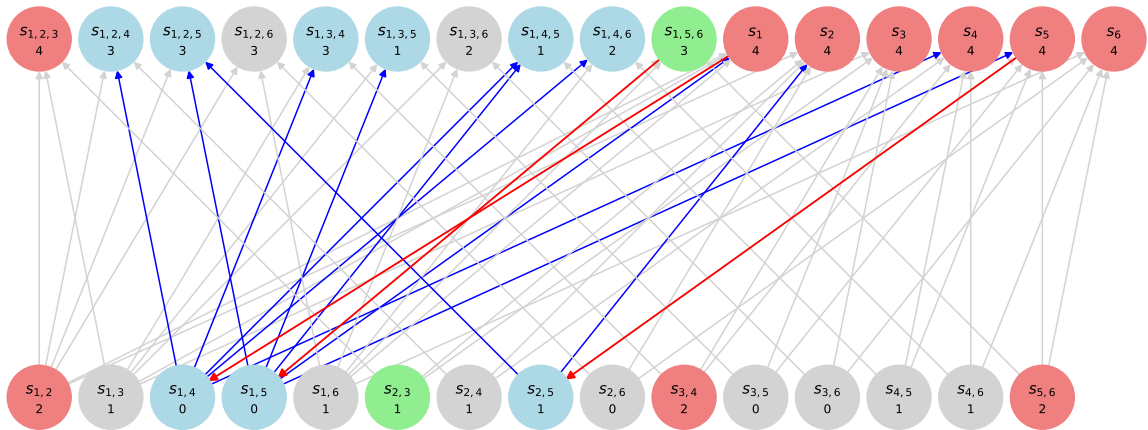


Figure 20. Continued upward propagation : Changes at s_{14} and s_{25} propagate upward, updating their three-particle supersets by $+1$. The algorithm encounters additional fixed points s_2 and s_4 , requiring another round of backward propagation to complete the constraint satisfaction process.

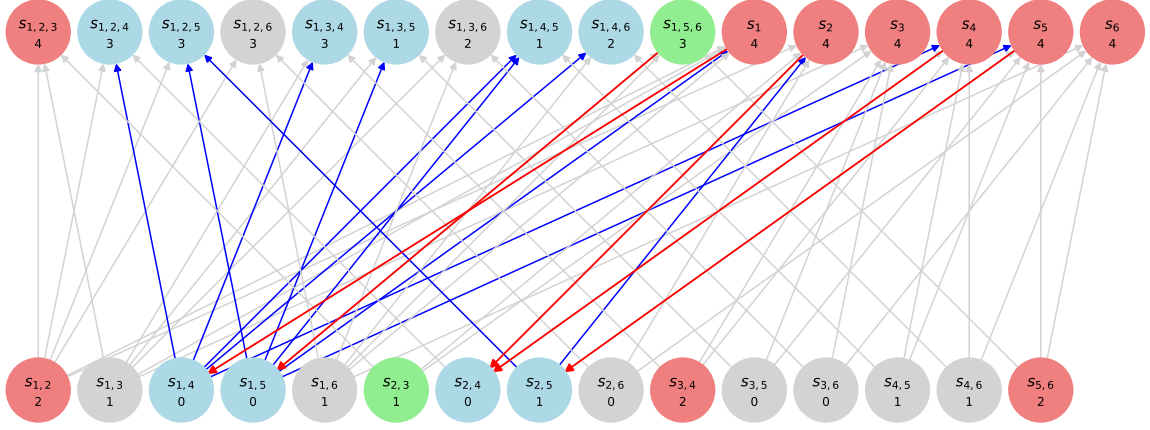


Figure 21. Final backward propagation : The last backward propagation step decrements the intersection s_{24} of supersets from fixed nodes s_2 and s_4 by -1 . This completes the constraint redistribution necessary to maintain all recursion relations while respecting fixed point constraints.

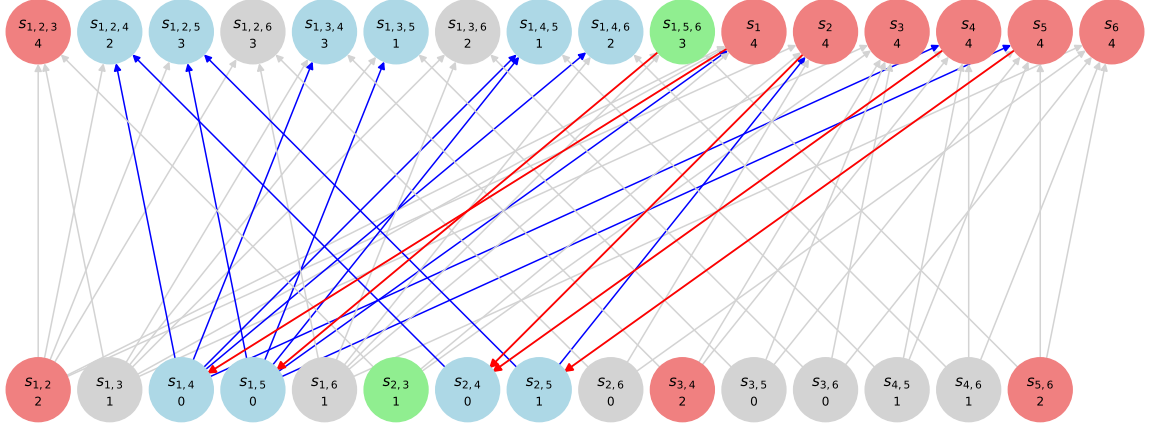


Figure 22. Algorithm convergence : The final upward propagation from s_{24} completes without encountering fixed constraints, indicating successful convergence of the discrete automatic differentiation algorithm. The removal of both unwanted poles s_{23} and s_{156} is now complete, yielding the desired CHY integrand.

The algorithm terminates successfully, yielding the modified CHY integrand:

$$I_6^* = \frac{1}{z_{12}^2 z_{13} z_{16} z_{23} z_{25} z_{34}^2 z_{45} z_{46} z_{56}^2}$$

This produces the amplitudes:

$$\frac{1}{s_{12} s_{34} s_{56}} + \frac{1}{s_{123} s_{12} s_{56}} + \frac{1}{s_{156} s_{34} s_{56}}$$

which successfully picks up all terms containing the desired pole s_{12} .

Summary

This 6-point example demonstrates the effectiveness of our neural-inspired pick-pole algorithm through discrete automatic differentiation on a **two-layer network structure**. The algorithm systematically removes unwanted poles while preserving desired ones through:

1. **Upward propagation:** Changes propagate from lower to higher layers following recursion relations
2. **Backward propagation:** Triggered by fixed constraints, redistributing changes to maintain consistency
3. **Bidirectional information flow:** Both upward and downward propagation enable comprehensive constraint satisfaction

The 6-point case reveals the fundamental two-layer architecture where single-particle and two-particle poles form the first layer, while three-particle poles constitute the second layer. For higher-multiplicity examples, such as the 8-point case which exhibits a **three-layer network structure** (with four-particle poles forming an additional layer), the same algorithmic principles apply but with increased complexity. These more complex examples are presented in Appendix D, demonstrating the scalability of our discrete automatic differentiation framework to larger particle multiplicities while maintaining exact constraint satisfaction throughout the computation.

4 Applications to Higher-Order Pole Expansion

4.1 Cross-Ratio Identities and Higher-Order Poles

Physical tree-level amplitudes must contain only simple poles corresponding to the propagation of on-shell intermediate particles—a requirement dictated by unitarity and locality. Yet when we expand the Pfaffian factors in Yang-Mills or gravity integrands, individual terms routinely exhibit poles of the form $1/s_A^\alpha$ with $\alpha > 1$. These unphysical singularities must precisely cancel when summing over all $(n - 3)!$ solutions to the scattering equations, but verifying such cancellations directly becomes computationally intractable even for moderate multiplicities [16].

For a given n -point CHY-integrand, the poles and the order of the poles can be determined by the pole index $\chi(A) := L[A] - 2(|A| - 1)$. Explicitly, each subset A gives a nonzero pole contribution if and only if $\chi(A) \geq 0$. From the previous algorithm for Feynman diagrams we can obtain all Feynman diagrams for the CHY-integrand with only simple poles. But for higher-order poles, the problem becomes complicated.

For the CHY-integrand with a pole of higher order $\frac{1}{s_A^\alpha}$, we can reduce the order of the CHY-integrand by multiplying an identity containing that pole s_A . The construction of the identity for general higher-order poles is similar to the cross-ratio. In [16], the cross-ratio identity for pole s_A with selected index $j \in A$ and $p \in \bar{A}$ is

$$I_n[A, j, p] \equiv - \sum_{i \in A \setminus \{j\}} \sum_{b \in \bar{A} \setminus \{p\}} \frac{s_{ib} z_{bp} z_{ij}}{s_A z_{ib} z_{jp}} = 1 \quad (4.1)$$

This identity holds only when the worldsheet coordinates $\{z_i\}$ satisfy the scattering equations, making it an on-shell relation that can be freely inserted into the CHY integral. The appearance of the factor s_{ib}/s_A is crucial—when multiplied with an integrand containing a higher-order pole $1/s_A^\alpha$, it effectively reduces the pole order by one. The cross-ratio structure encoded in the factors $z_{bp} z_{ij}/(z_{ib} z_{jp})$ ensures that the resulting terms maintain the correct transformation properties under Möbius transformations.

This cross-ratio identity multiply the CHY-integrand with higher-order poles, and helps as we decompose this CHY-integrand into several CHY-integrand with only simple poles. They decompose the CHY-integrand by iteratively reducing the higher-order poles, until every resulting CHY-integrand is composed of simple poles in a systematic decomposition algorithm. The algorithm proceeds as follows: for each subset A with $\chi(A) > 0$, we apply the appropriate cross-ratio identity, generating a linear combination of new integrands. This process continues until all resulting integrands satisfy $\chi(B) \leq 0$ for all subsets B , ensuring only physical simple poles remain.

However, during the iteration process, we have no control over whether the decomposition increases or decreases the higher-order poles of CHY-integrand, which will lead to redundant terms. So our job is to decrease as much as possible the number of CHY-integrand that contain only simple poles. In the following, we will propose a new decomposition algorithm based on the systematic decomposition algorithm that will be expected to reduce those redundant terms. In this chapter, we explore how the methods developed in previous sections can be applied to this fundamental problem.

4.2 Decomposing 0-Regular Graphs into Cross-Ratios

As established in Section 2.2, the 0-regular graphs form a group under multiplication and act as transformations on CHY integrands while preserving their regularity class. A crucial insight for decomposing higher-order poles is that multiplying a CHY integrand by an appropriate 0-regular graph can systematically reduce the pole orders. Specifically, when a CHY integrand contains a higher-order pole $1/s_A^\alpha$ with $\alpha > 1$, we can construct a suitable 0-regular graph whose multiplication reduces this pole to simple poles, thereby enabling the systematic decomposition described in Section 4.1.

The 0-regular graphs can be understood as generalized long cross-ratios that extend beyond the standard four-point cross-ratios. A key computational advantage emerges from the fact that any 0-regular graph, regardless of its complexity, can be systematically decomposed into products of standard four-point cross-ratios. This decomposition provides a systematic algorithm for constructing the cross-ratio identities needed for higher-order pole reduction.

Decomposition Algorithm for 0-regular Graphs. The systematic decomposition of 0-regular graphs into standard cross-ratios follows a graph-theoretic algorithm based on bipartite graph representations and Hamiltonian cycle theory. The algorithm proceeds as follows and is illustrated in Figure 23:

Step 1: Bipartite Graph Construction. Transform the 0-regular graph into a bipartite representation where vertices are partitioned into two sets, with solid edges connecting vertices from different sets and dashed edges represented as constraints on the bipartite structure.

Step 2: Hamiltonian Path Construction. From left to right in the bipartite representation, construct a closed path containing exactly four points by following the pattern: solid edges (left to right), dashed edges (right to left). This systematic traversal ensures that we identify minimal four-point cross-ratio structures within the larger graph.

Step 3: Path Completion. If a closed four-point path cannot be immediately formed, we can add one solid edge and one dashed edge at appropriate vertices while maintaining the 0-regular property of the graph. This operation preserves the graph's net degree structure while enabling path completion.

Step 4: Cross-ratio Identification. By Hamilton's theorem for graph cycles, the above operations will always yield a closed four-point path. Each such path corresponds to a decomposition where a six-point cross-ratio factor $\frac{z_{ij}z_{kl}z_{mn}}{z_{in}z_{jk}z_{lm}}$ can be decomposed into two four-point cross-ratios:

$$\frac{z_{ij}z_{kl}}{z_{il}z_{kj}} \times \frac{z_{kl}z_{mn}}{z_{kn}z_{ml}} \quad (4.2)$$

Enhanced Decomposition Method for Higher-Order Pole Integrands. With the systematic decomposition of 0-regular graphs established, we can now develop a more efficient method for decomposing higher-order pole integrands that significantly reduces computational complexity compared to the systematic approach outlined in Section [16].

Enhanced Algorithm:

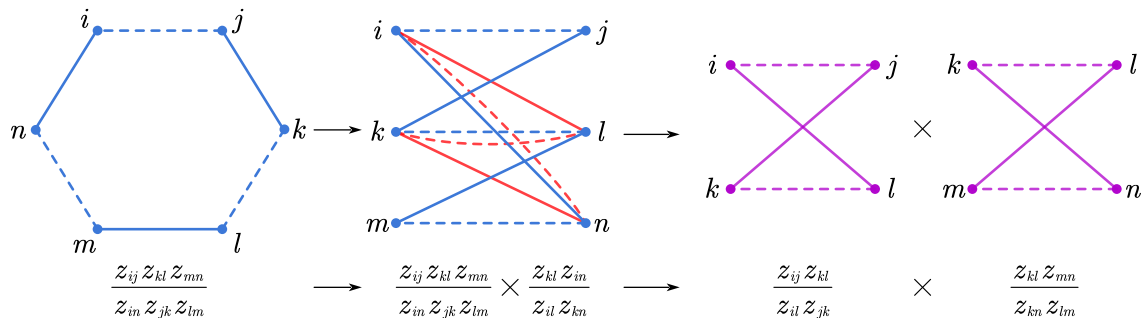


Figure 23. Systematic decomposition of 0-regular graphs into standard cross-ratios. (a) Original 0-regular graph, (b) Bipartite representation, (c) Hamiltonian path identification, (d) Resulting cross-ratio decomposition.

1. **0-regular Graph Construction:** For a given higher-order pole integrand, apply the methods from Section 2 to construct an appropriate 0-regular graph that reduces the higher-order poles when multiplied with the original integrand.
2. **Cross-ratio Decomposition:** Apply the algorithm described above to decompose this 0-regular graph into products of standard four-point cross-ratios, systematically identifying all minimal cross-ratio structures.
3. **Cross-Ratio Identity Construction:** For each four-point cross-ratio identified in the decomposition, construct the corresponding cross-ratio identity using the methods from Section 4.1. This yields a set of multiplicative factors that can be applied to the original integrand.

The key advantage of this enhanced approach is computational efficiency. Rather than applying multiple cross-ratio identities simultaneously (which leads to exponential growth in the number of terms), we apply them sequentially based on the systematic decomposition of the 0-regular graph.

Computational Advantages. Our preliminary analysis of two representative examples demonstrates that this enhanced decomposition method produces significantly fewer intermediate terms compared to the symmetric approach mentioned in Section 4.1. Specifically:

- The traditional symmetric approach applies all necessary cross-ratio identities simultaneously, leading to $\prod_i n_i$ terms where n_i is the number of terms in each identity.
- Our enhanced method applies identities sequentially based on the 0-regular graph decomposition, typically reducing the total number of terms by factors of 2-5 depending on the complexity of the pole structure.

In the following sections, we will demonstrate this enhanced method through detailed examples of 6-point and 8-point CHY integrands with higher-order poles, showing explicit

comparisons between the number of terms generated by each approach. These examples illustrate both the theoretical elegance and practical computational advantages of the graph-theoretic approach to pole decomposition in the CHY formalism.

4.3 Examples: 6-Point CHY Integrand with Higher-Order Poles

We demonstrate our enhanced decomposition method through a concrete six-point example that illustrates the computational advantages over traditional approaches. Consider the CHY integrand

$$I_6 = \frac{1}{z_{12}^3 z_{23} z_{34}^3 z_{45} z_{56}^3 z_{61}}, \quad (4.3)$$

whose 4-regular graph representation is shown in Figure 24.

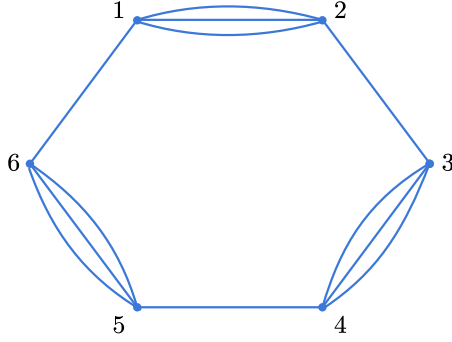


Figure 24. The 4-regular graph representation of the six-point CHY integrand I_6 . Each vertex represents a particle, and the edge multiplicities encode the powers in the denominator of equation (4.3). The triple edges connecting vertices (1, 2), (3, 4), and (5, 6) correspond to the factors z_{12}^3 , z_{34}^3 , and z_{56}^3 respectively, immediately revealing the three double poles in the amplitude.

Using the pole index formula $\chi(A) = L[A] - 2(|A| - 1)$, we identify that this integrand contains exactly three double poles: s_{12} , s_{34} , and s_{56} (where $\chi = 1$ for each). To systematically reduce these higher-order poles to simple poles, we employ the cross-ratio identity method with the six-point cross-ratio factor $\frac{z_{12}z_{34}z_{56}}{z_{16}z_{23}z_{45}}$.

The key to our enhanced approach is the systematic decomposition of this six-point cross-ratio into elementary four-point factors, as illustrated in Figure 25.

Based on this decomposition, we strategically select two basic cross-ratio identities that minimize the generation of new higher-order poles:

$$I_6[\{1, 2\}, 1, 4] = -\frac{s_{23}z_{21}z_{34}}{s_{12}z_{14}z_{23}} - \frac{s_{25}z_{21}z_{54}}{s_{12}z_{14}z_{25}} - \frac{s_{26}z_{21}z_{64}}{s_{12}z_{14}z_{26}}, \quad (4.4)$$

$$I_6[\{5, 6\}, 6, 3] = -\frac{s_{51}z_{13}z_{56}}{s_{56}z_{51}z_{63}} - \frac{s_{52}z_{23}z_{56}}{s_{56}z_{52}z_{63}} - \frac{s_{54}z_{43}z_{56}}{s_{56}z_{54}z_{63}}. \quad (4.5)$$

Multiplying I_6 by these identities yields $3^2 = 9$ terms, whose pole structures are systematically tracked in Figure 26.

Among these nine terms, five immediately yield CHY integrands with only simple poles, while the remaining four terms

$$I_6 \times \frac{s_{26}s_{52}}{s_{12}s_{56}} \frac{z_{12}z_{23}z_{46}z_{56}}{z_{14}z_{25}z_{26}z_{36}}, \quad I_6 \times \frac{s_{25}s_{52}}{s_{12}s_{56}} \frac{z_{12}z_{23}z_{45}z_{56}}{z_{14}z_{25}^2z_{36}}, \quad \text{etc.} \quad (4.6)$$

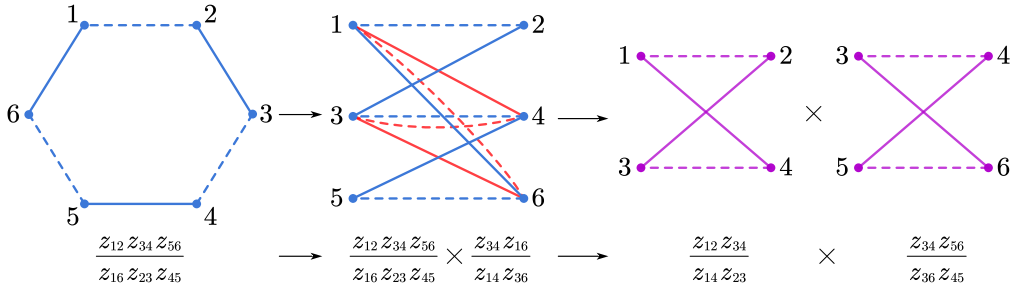


Figure 25. Systematic decomposition of the six-point cross-ratio factor $\frac{z_{12} z_{34} z_{56}}{z_{16} z_{23} z_{45}}$ into two four-point cross-ratios. The bipartite representation (center) reveals the natural factorization into $\frac{z_{12} z_{34}}{z_{14} z_{23}} \times \frac{z_{34} z_{56}}{z_{36} z_{45}}$, providing the foundation for our sequential application of cross-ratio identities.

still contain the double pole s_{34} .

To eliminate this remaining higher-order pole, we apply the cross-ratio identity for subset $\{3, 4\}$:

$$I_6[\{3, 4\}, 3, 1] = -\frac{s_{42} z_{21} z_{43}}{s_{34} z_{31} z_{42}} - \frac{s_{45} z_{51} z_{43}}{s_{34} z_{31} z_{45}} - \frac{s_{46} z_{61} z_{43}}{s_{34} z_{31} z_{46}}. \quad (4.7)$$

Figures 27–30 illustrate how each of the four intermediate terms is further decomposed into three terms with only simple poles.

Through this systematic process, the original CHY integrand I_6 with three double poles is decomposed into $5 + 4 \times 3 = 17$ terms, each containing only simple poles. The sum of these 17 terms reproduces the correct amplitude with all physical and spurious pole cancellations properly accounted for.

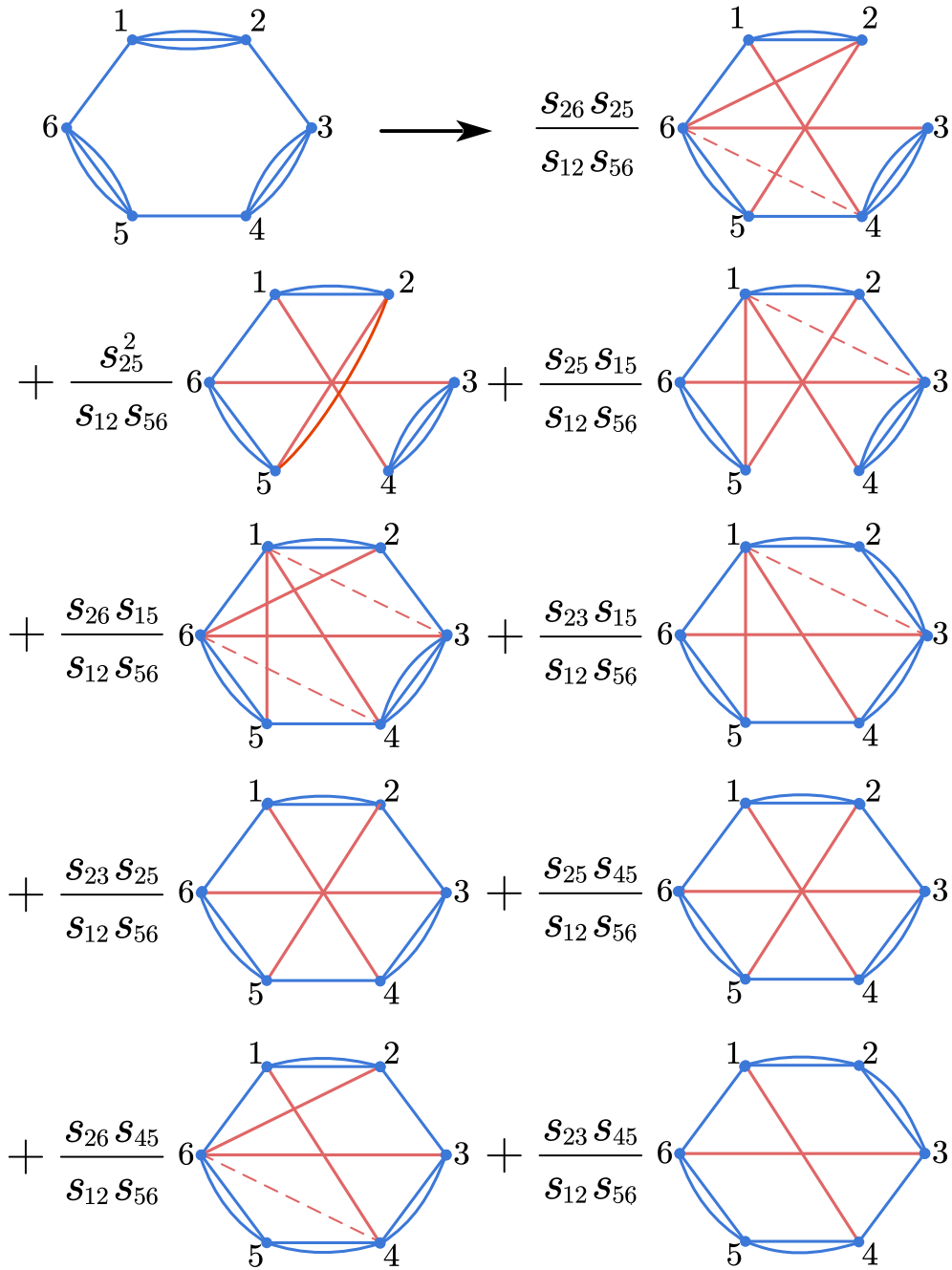


Figure 26. Complete decomposition tree showing how the original integrand I_6 with three double poles is systematically reduced through cross-ratio identities. The first level shows the $3 \times 3 = 9$ terms from applying identities (4.4) and (4.5). Five terms (shown in gray) already contain only simple poles, while four terms (shown in white) retain the double pole s_{34} , requiring further decomposition.

$$\begin{aligned}
& \frac{\mathcal{S}_{26} \mathcal{S}_{25}}{\mathcal{S}_{12} \mathcal{S}_{56}} \text{Diagram}_1 \longrightarrow - \frac{\mathcal{S}_{26} \mathcal{S}_{25} \mathcal{S}_{24}}{\mathcal{S}_{12} \mathcal{S}_{56} \mathcal{S}_{34}} \text{Diagram}_2 \\
& - \frac{\mathcal{S}_{26} \mathcal{S}_{25} \mathcal{S}_{45}}{\mathcal{S}_{12} \mathcal{S}_{56} \mathcal{S}_{34}} \text{Diagram}_3 - \frac{\mathcal{S}_{26} \mathcal{S}_{25} \mathcal{S}_{46}}{\mathcal{S}_{12} \mathcal{S}_{56} \mathcal{S}_{34}} \text{Diagram}_4
\end{aligned}$$

Figure 27. Decomposition of the first intermediate term containing double pole s_{34} . Applying identity (4.7) yields three CHY integrands with only simple poles, each corresponding to a distinct channel in the final amplitude. The cross-ratio factors effectively cancel the z_{34}^3 contribution, reducing the pole order from 2 to 1.

$$\begin{aligned}
& \frac{\mathcal{S}_{25}^2}{\mathcal{S}_{12} \mathcal{S}_{56}} \text{Diagram}_1 \longrightarrow - \frac{\mathcal{S}_{25}^2 \mathcal{S}_{24}}{\mathcal{S}_{12} \mathcal{S}_{56} \mathcal{S}_{34}} \text{Diagram}_2 \\
& - \frac{\mathcal{S}_{25}^2 \mathcal{S}_{45}}{\mathcal{S}_{12} \mathcal{S}_{56} \mathcal{S}_{34}} \text{Diagram}_3 - \frac{\mathcal{S}_{25}^2 \mathcal{S}_{46}}{\mathcal{S}_{12} \mathcal{S}_{56} \mathcal{S}_{34}} \text{Diagram}_4
\end{aligned}$$

Figure 28. Decomposition of the second intermediate term. The systematic application of identity (4.7) again produces three terms with simple poles, demonstrating the consistency of our approach across different intermediate configurations.

$$\begin{aligned}
& \frac{\mathcal{S}_{25} \mathcal{S}_{15}}{\mathcal{S}_{12} \mathcal{S}_{56}} \text{Diagram 1} \longrightarrow - \frac{\mathcal{S}_{25} \mathcal{S}_{15} \mathcal{S}_{24}}{\mathcal{S}_{12} \mathcal{S}_{56} \mathcal{S}_{34}} \text{Diagram 2} \\
& - \frac{\mathcal{S}_{25} \mathcal{S}_{15} \mathcal{S}_{45}}{\mathcal{S}_{12} \mathcal{S}_{56} \mathcal{S}_{34}} \text{Diagram 3} - \frac{\mathcal{S}_{25} \mathcal{S}_{15} \mathcal{S}_{24}}{\mathcal{S}_{12} \mathcal{S}_{56} \mathcal{S}_{34}} \text{Diagram 4}
\end{aligned}$$

Figure 29. Decomposition of the third intermediate term. Note how the cross-ratio identity precisely targets the s_{34} pole while preserving the simple pole structure in other channels.

$$\begin{aligned}
& \frac{\mathcal{S}_{26} \mathcal{S}_{15}}{\mathcal{S}_{12} \mathcal{S}_{56}} \text{Diagram 1} \longrightarrow - \frac{\mathcal{S}_{26} \mathcal{S}_{15} \mathcal{S}_{24}}{\mathcal{S}_{12} \mathcal{S}_{56} \mathcal{S}_{34}} \text{Diagram 2} \\
& - \frac{\mathcal{S}_{26} \mathcal{S}_{15} \mathcal{S}_{45}}{\mathcal{S}_{12} \mathcal{S}_{56} \mathcal{S}_{34}} \text{Diagram 3} - \frac{\mathcal{S}_{26} \mathcal{S}_{15} \mathcal{S}_{46}}{\mathcal{S}_{12} \mathcal{S}_{56} \mathcal{S}_{34}} \text{Diagram 4}
\end{aligned}$$

Figure 30. Decomposition of the fourth and final intermediate term. The complete decomposition process transforms one integrand with three double poles into 17 integrands with only simple poles.

Computational Efficiency and Comparison

Our enhanced decomposition method demonstrates significant computational advantages over traditional approaches. For this six-point example with three double poles (s_{12} , s_{34} , s_{45}):

Method	Total Terms	Decomposition Steps
Systematic algorithm [16]	27	4
Our enhanced method	17	2

This improvement becomes even more pronounced for higher-multiplicity amplitudes. A detailed eight-point example demonstrating the scalability of our approach is presented in Appendix E, where the reduction from 265 to 153 terms showcases the method’s effectiveness for more complex cases.

Through this three-round process, the eight-point CHY integrand I_8 with four double poles is systematically decomposed into $9 + 60 + 12 + 72 = 153$ terms, each containing only simple poles. The improvement over traditional methods is summarized in the following table:

Method	Round 1	Round 2	Round 3	Round 4	Total
Systematic algorithm [16]	5 [5]	25 [20]	105 [20]	265 [0]	265
Our method	25 [16]	89 [8]	153 [0]	—	153

Numbers in brackets $[\cdot]$ indicate terms with remaining higher-order poles at each stage.

The systematic nature of our decomposition, guided by the graph-theoretic structure of 0-regular graphs, ensures that this computational advantage persists as we move toward even higher multiplicities relevant for precision calculations in quantum field theory. Our enhanced method achieves a reduction factor by:

1. Systematically decomposing cross-ratio factors using the 0-regular graph structure
2. Applying identities sequentially to minimize intermediate term proliferation
3. Leveraging the hierarchical nature of pole constraints to optimize the decomposition order

These examples demonstrate that our 0-regular-graph approach to higher-order pole decomposition maintains its computational advantages as complexity increases, making it a practical tool for higher-order pole calculations.

5 Conclusion

In this work, we have established a profound connection between the combinatorial structure of CHY integrands and the architecture of Combinatorial Neural Networks, revealing how discrete optimization techniques can provide analytically exact solutions to fundamental problems in scattering amplitude calculations. Our framework, built upon the generalized pole degree $K(s_A)$, transforms the abstract mathematical challenges of the CHY formalism into concrete computational problems with guaranteed exact solutions.

The key achievements of our approach can be summarized as follows:

1. Algebraic Foundation: The generalized pole degree $K(s_A)$ provides a transparent characterization of CHY integrands through two fundamental properties—additivity under multiplication and hierarchical recursion relations. These properties reveal that the pole structure forms a graded algebraic system, enabling systematic manipulation of integrand compositions.

2. Exact Inverse Construction: By reformulating the inverse CHY problem as mixed integer linear programming, we transform the combinatorial search through possible integrands into a well-defined optimization problem. The recursion relations create a system of linear constraints that can be solved exactly, yielding all valid CHY integrands for a given pole structure.

3. Combinatorial Neural Network Correspondence: The hierarchical propagation of pole degrees through the recursion relations naturally maps to the message-passing architecture of Combinatorial Neural Networks. This correspondence is not merely conceptual—it provides a concrete algorithmic framework where upward and downward propagation in the pole hierarchy corresponds to forward and backward passes in the network, with discrete gradients maintaining exact algebraic constraints throughout.

4. Algorithmic Efficiency: Our discrete automatic differentiation algorithm guarantees exact integer solutions. Unlike continuous optimization methods that yield numerical approximations, our approach preserves all algebraic relations exactly, ensuring that the output is always a valid CHY integrand satisfying all physical constraints.

5. Higher-order Pole Reduction: The framework extends naturally to higher-order pole decomposition through 0-regular graph factorization. Our examples demonstrate significant computational advantages over existing methods, reducing the number of intermediate terms while maintaining complete algebraic control over the decomposition process.

The distinguishing feature of our approach is the synergy between the **combinatorial structure inherent in the CHY formalism** and the **training process of Combinatorial Neural Networks**. This is not a traditional numerical approximation scheme—every step maintains exact algebraic relations, and the final results are analytically precise. The discrete nature of our optimization perfectly matches the integer-valued constraints of the CHY formalism, while the neural network architecture naturally captures the hierarchical dependencies among poles.

Looking forward, this work opens several promising directions for future research, particularly in connecting with the broader geometric program of scattering amplitudes:

Amplituhedron and Positive Geometries: Recent revolutionary developments in scattering amplitude theory have revealed that amplitudes can be understood as volumes of certain “positive geometries” [58, 59]. The amplituhedron, a geometric object whose volume directly encodes the integrand of planar $\mathcal{N} = 4$ super Yang-Mills amplitudes, exemplifies this paradigm shift. Our combinatorial framework naturally aligns with this geometric perspective—just as the amplituhedron can be triangulated into BCFW cells [60], our discrete optimization approach systematically decomposes complex integrands into elementary building blocks. The success of our method for CHY integrands suggests that similar neural-inspired algorithms could tackle the combinatorial challenges of amplituhedron triangulations, where finding optimal decompositions remains a central computational challenge.

Associahedra and Cluster Algebras: The connection between scattering amplitudes and associahedra has proven fundamental for understanding tree-level amplitudes in bi-adjoint scalar theories [61]. The associahedron’s vertices correspond to triangulations of polygons, while its face structure encodes factorization channels—a direct geometric realization of locality. This combinatorial structure is governed by cluster algebras [62], whose mutation sequences bear striking resemblance to the propagation rules in our discrete automatic differentiation. Our framework could be extended to systematically explore the space of kinematic associahedra and their generalizations, potentially revealing new classes of theories with geometric origins.

Positive Grassmannian and On-Shell Diagrams: The positive Grassmannian $Gr_{k,n}^+$ provides a unified geometric space for organizing on-shell processes [63]. Each positroid cell corresponds to an on-shell diagram, with the cell decomposition governed by combinatorial rules. Our neural network architecture, designed to handle hierarchical constraint propagation, could be adapted to navigate the positroid stratification efficiently. This would enable systematic construction of on-shell diagrams satisfying specific singularity requirements, extending our pole selection algorithms to the richer geometric setting of the Grassmannian.

Loop-Level Extensions and Tropical Geometry: While our current work focuses on tree-level amplitudes, the geometric structures persist at loop level through connections to tropical geometry [64]. The tropical limit of the positive Grassmannian reveals a polyhedral structure amenable to combinatorial optimization. Our discrete framework could potentially address the increased complexity of loop integrands by leveraging these tropical structures, where the continuous moduli space degenerates into a discrete combinatorial skeleton.

Machine Learning for Amplitude Bootstrap: Recent applications of transformer models to predict amplitude coefficients [65] demonstrate the potential of machine learning in amplitude calculations. Our work provides a complementary approach—rather than learning from data, we embed the exact combinatorial constraints into the network architecture itself. This suggests a hybrid approach where transformers could learn optimal strategies for navigating the discrete optimization landscape defined by our framework, potentially discovering new patterns in the space of consistent quantum field theories.

The convergence of theoretical physics and modern computational mathematics ex-

emplified in this work represents more than a technical advance—it points toward a new paradigm where the combinatorial structures underlying physical theories can be directly leveraged by specialized computational architectures. As we push toward higher multiplicities and more complex calculations, such interdisciplinary approaches that recognize and exploit the deep mathematical structures of physics will become increasingly essential. The exact, analytical nature of our results, achieved through discrete optimization on combinatorial structures, demonstrates that machine learning techniques need not be limited to numerical approximations but can provide rigorous mathematical tools for theoretical physics.

Acknowledgements

We are sincerely grateful to Ningxia University for its generous startup funding, and we appreciate the assistance of AI-based tools in polishing the presentation of this work.

A Proofs of Recursion Relations of $K(A)$

Proof of the fundamental recursion

We prove the fundamental recursion (2.5) by induction on $|A|$.

Base case ($|A| = 3$): For a three-element set $A = \{a, b, c\}$, there are exactly three codimension-1 subsets: $\{a, b\}$, $\{b, c\}$, and $\{a, c\}$. By direct inspection of the graph, each internal edge of the triangle (a, b, c) is counted exactly once when summing the edges of the three two-element subsets. Therefore:

$$K(abc) = K(ab) + K(bc) + K(ac) = \frac{1}{1!}[K(ab) + K(bc) + K(ac)]$$

which confirms (2.5) since $(|A| - 2)! = 1! = 1$.

Inductive step: Assume (2.5) holds for all subsets of size m with $3 \leq m < |A|$. Consider a subset A with $|A| \geq 4$. For each $(|A| - 1)$ -element subset $B \subset A$, the induction hypothesis gives:

$$K(B) = \frac{1}{(|B| - 2)!} \sum_{\substack{C \subset B \\ |C|=|B|-1}} K(C) = \frac{1}{(|A| - 3)!} \sum_{\substack{C \subset B \\ |C|=|A|-2}} K(C)$$

Summing over all $|A|$ subsets $B \subset A$ with $|B| = |A| - 1$:

$$\sum_{\substack{B \subset A \\ |B|=|A|-1}} K(B) = \frac{1}{(|A| - 3)!} \sum_{\substack{B \subset A \\ |B|=|A|-1}} \sum_{\substack{C \subset B \\ |C|=|A|-2}} K(C)$$

Each $(|A| - 2)$ -element subset $C \subset A$ appears in the double sum exactly $|A| - |C| = 2$ times. By a careful counting argument involving the distribution of edges among subgraphs, we obtain:

$$K(A) = \frac{1}{(|A| - 2)!} \sum_{\substack{B \subset A \\ |B|=|A|-1}} K(B)$$

This completes the induction. \square

Proof of the general recursion

We provide a direct combinatorial proof of (2.6). Consider any edge $e = (i, j)$ in the graph with both endpoints $i, j \in A$. Define the indicator function:

$$m_e(B) = \begin{cases} 1 & \text{if both } i, j \in B \\ 0 & \text{otherwise} \end{cases}$$

The key observation is that for each such edge:

$$\sum_{\substack{B \subset A \\ |B|=|A|-d}} m_e(B) = \binom{|A| - 2}{|A| - d - 2} = \binom{|A| - 2}{d}$$

This count follows because the edge e contributes to the sum if and only if B contains both i and j . The number of such subsets equals the number of ways to choose the remaining $|A| - d - 2$ elements from the $|A| - 2$ elements in $A \setminus \{i, j\}$.

Since $K(s_A)$ counts the net number of internal edges (solid minus dashed), and each edge's contribution is multiplied by exactly $\binom{|A|-2}{d}$ in the sum, we obtain:

$$\sum_{\substack{B \subset A \\ |B|=|A|-d}} K(B) = \binom{|A|-2}{d} \cdot K(A)$$

Dividing both sides by $\binom{|A|-2}{d}$ yields the general recursion (2.6). \square

B Solving Bootstrap Equations via Integer Linear Programming

The inverse CHY problem—constructing integrands from desired amplitude structures—presents unique mathematical challenges. Unlike the forward problem of evaluating known integrands, the inverse problem requires navigating a vast discrete space of possible graph configurations while satisfying intricate algebraic constraints. The combinatorial nature of this problem, combined with the requirement for exact integer solutions, places it firmly in the realm of NP-hard optimization problems [66, 67].

This appendix describes how modern computational optimization techniques, specifically Integer Linear Programming (ILP), can be leveraged to solve the bootstrap equations systematically. The approach transforms the abstract mathematical problem into a concrete computational framework amenable to well-established algorithmic solutions.

Mathematical Formulation. The bootstrap construction requires finding integer values $\{K(s_{ij})\}$ that satisfy a system of linear constraints derived from physical requirements:

- **Equality constraints:** For desired poles, $K(s_A) = 2(|A| - 1)$
- **Inequality constraints:** For unwanted poles, $K(s_A) < 2(|A| - 1)$
- **Regularity constraints:** For 4-regular graphs, $K_i = \sum_{j \neq i} K(s_{ij}) = 4$

This naturally maps to an Integer Linear Programming problem:

- **Variables:** $\vec{x} = (K(s_{12}), K(s_{13}), \dots, K(s_{n-1,n}))^T \in \mathbb{Z}^{\binom{n}{2}}$
- **Constraints:** $\mathbf{A}_{eq} \vec{x} = \vec{b}_{eq}$, $\mathbf{A}_{ineq} \vec{x} < \vec{b}_{ineq}$
- **Feasibility:** Find any \vec{x} satisfying all constraints (no objective function)

The key insight enabling this formulation is that all higher-order pole degrees $K(s_A)$ with $|A| > 2$ can be expressed as linear combinations of the fundamental variables $\{K(s_{ij})\}$ via the recursion relations (2.5). This linearization is crucial—without it, the constraints would involve nonlinear relationships that would make the problem intractable.

Computational Complexity. The difficulty of this problem cannot be overstated. For an n -particle amplitude:

- The number of variables scales as $\binom{n}{2} = O(n^2)$
- The number of potential constraints scales as $2^n - 1$ (one for each subset)
- The search space for integer solutions grows exponentially

Even for moderate values of n , brute-force enumeration becomes impossible. For $n = 10$, there are already 45 variables and over 1000 potential constraints. The integer requirement transforms what would be a polynomial-time solvable linear program into an NP-hard problem [68, 69].

Algorithmic Approaches. Modern ILP solvers employ sophisticated techniques to handle this complexity. The fundamental framework is Branch-and-Bound, enhanced with cutting plane methods [70, 71]:

Algorithm 4 Enhanced Branch-and-Cut Algorithm

```

1: Solve LP relaxation using simplex or interior point methods
2: if solution is integer then
3:   return solution
4: else
5:   Apply cutting plane generation (Gomory cuts, lift-and-project)
6:   Select branching variable using strong branching or pseudocost
7:   Create child nodes with disjoint constraints
8:   Apply preprocessing: bound tightening, constraint propagation
9:   Recursively solve subproblems with pruning based on bounds
10:  Use heuristics (feasibility pump, RINS) to find integer solutions
11: end if

```

Recent advances in ILP solvers have improved performance through parallelization, machine learning-guided branching strategies, and symmetry detection [72, 73].

Implementation Details. For practical implementation, we utilize:

In **Mathematica** [74]:

- `k[i, j]`: Integer variable representation
- `KValue[set]`: Recursive computation using memoization
- `FindInstance`: Leverages internal ILP solver with symmetry detection

In **Python** [75]:

- `scipy.optimize.milp`: Interfaces with HiGHS solver [76]
- `cvxpy`: Provides modeling language with automatic reformulation [77]
- `PuLP`: Connects to commercial solvers (Gurobi, CPLEX) [78]

The 8-Particle Example. We demonstrate the method on an 8-particle amplitude requiring poles at $s_{15}, s_{16}, s_{23}, s_{68}, s_{78}, s_{156}, s_{234}, s_{378}, s_{678}, s_{1256}$, and s_{3478} . This example, while manageable computationally, exhibits the full complexity of the problem:

- 28 integer variables $\{K(s_{ij})\}_{1 \leq i < j \leq 8}$ includes 5 equalities:

$$K_{1,5} = 2, K_{1,6} = 2, K_{2,3} = 2, K_{6,8} = 2, K_{7,8} = 2,$$

and 23 inequalities:

$$\begin{aligned} K_{1,2} < 2, K_{1,3} < 2, K_{1,4} < 2, K_{1,7} < 2, K_{1,8} < 2, K_{2,4} < 2, K_{2,5} < 2, K_{2,6} < 2, \\ K_{2,7} < 2, K_{2,8} < 2, K_{3,4} < 2, K_{3,5} < 2, K_{3,6} < 2, K_{3,7} < 2, K_{3,8} < 2, K_{4,5} < 2, \\ K_{4,6} < 2, K_{4,7} < 2, K_{4,8} < 2, K_{5,6} < 2, K_{5,7} < 2, K_{5,8} < 2, K_{6,7} < 2. \end{aligned}$$

- 162 total constraints (20 equalities, 142 inequalities). In addition to the above 28 integer variables, it also includes 15 equalities:

$$\begin{aligned} K_{1,2} + K_{1,6} + K_{2,6} &= 4, K_{1,5} + K_{1,6} + K_{5,6} = 4, K_{2,3} + K_{2,4} + K_{3,4} = 4, \\ K_{3,7} + K_{3,8} + K_{7,8} &= 4, K_{6,7} + K_{6,8} + K_{7,8} = 4, \\ K_{1,2} + K_{1,5} + K_{1,6} + K_{2,5} + K_{2,6} + K_{5,6} &= 6, \\ K_{3,4} + K_{3,7} + K_{3,8} + K_{4,7} + K_{4,8} + K_{7,8} &= 6, \\ K_1 = K_{1,2} + K_{1,3} + K_{1,4} + K_{1,5} + K_{1,6} + K_{1,7} + K_{1,8} &= 4, \\ K_2 = K_{1,2} + K_{2,3} + K_{2,4} + K_{2,5} + K_{2,6} + K_{2,7} + K_{2,8} &= 4, \\ K_3 = K_{1,3} + K_{2,3} + K_{3,4} + K_{3,5} + K_{3,6} + K_{3,7} + K_{3,8} &= 4, \\ K_4 = K_{1,4} + K_{2,4} + K_{3,4} + K_{4,5} + K_{4,6} + K_{4,7} + K_{4,8} &= 4, \\ K_5 = K_{1,5} + K_{2,5} + K_{3,5} + K_{4,5} + K_{5,6} + K_{5,7} + K_{5,8} &= 4, \\ K_6 = K_{1,6} + K_{2,6} + K_{3,6} + K_{4,6} + K_{5,6} + K_{6,7} + K_{6,8} &= 4, \\ K_7 = K_{1,7} + K_{2,7} + K_{3,7} + K_{4,7} + K_{5,7} + K_{6,7} + K_{7,8} &= 4, \\ K_8 = K_{1,8} + K_{2,8} + K_{3,8} + K_{4,8} + K_{5,8} + K_{6,8} + K_{7,8} &= 4. \end{aligned}$$

and 51 inequalities, of three poles:

$$\begin{aligned}
&K_{1,2} + K_{1,3} + K_{2,3} < 4, K_{1,2} + K_{1,4} + K_{2,4} < 4, K_{1,2} + K_{1,5} + K_{2,5} < 4, \\
&K_{1,2} + K_{1,7} + K_{2,7} < 4, K_{1,2} + K_{1,8} + K_{2,8} < 4, K_{1,3} + K_{1,4} + K_{3,4} < 4, \\
&K_{1,3} + K_{1,5} + K_{3,5} < 4, K_{1,3} + K_{1,6} + K_{3,6} < 4, K_{1,3} + K_{1,7} + K_{3,7} < 4, \\
&K_{1,3} + K_{1,8} + K_{3,8} < 4, K_{1,4} + K_{1,5} + K_{4,5} < 4, K_{1,4} + K_{1,6} + K_{4,6} < 4, \\
&K_{1,4} + K_{1,7} + K_{4,7} < 4, K_{1,4} + K_{1,8} + K_{4,8} < 4, K_{1,5} + K_{1,7} + K_{5,7} < 4, \\
&K_{1,5} + K_{1,8} + K_{5,8} < 4, K_{1,6} + K_{1,7} + K_{6,7} < 4, K_{1,6} + K_{1,8} + K_{6,8} < 4, \\
&K_{1,7} + K_{1,8} + K_{7,8} < 4, K_{2,3} + K_{2,5} + K_{3,5} < 4, K_{2,3} + K_{2,6} + K_{3,6} < 4, \\
&K_{2,3} + K_{2,7} + K_{3,7} < 4, K_{2,3} + K_{2,8} + K_{3,8} < 4, K_{2,4} + K_{2,5} + K_{4,5} < 4, \\
&K_{2,4} + K_{2,6} + K_{4,6} < 4, K_{2,4} + K_{2,7} + K_{4,7} < 4, K_{2,4} + K_{2,8} + K_{4,8} < 4, \\
&K_{2,5} + K_{2,6} + K_{5,6} < 4, K_{2,5} + K_{2,7} + K_{5,7} < 4, K_{2,5} + K_{2,8} + K_{5,8} < 4, \\
&K_{2,6} + K_{2,7} + K_{6,7} < 4, K_{2,6} + K_{2,8} + K_{6,8} < 4, K_{2,7} + K_{2,8} + K_{7,8} < 4, \\
&K_{3,4} + K_{3,5} + K_{4,5} < 4, K_{3,4} + K_{3,6} + K_{4,6} < 4, K_{3,4} + K_{3,7} + K_{4,7} < 4, \\
&K_{3,4} + K_{3,8} + K_{4,8} < 4, K_{3,5} + K_{3,6} + K_{5,6} < 4, K_{3,5} + K_{3,7} + K_{5,7} < 4, \\
&K_{3,5} + K_{3,8} + K_{5,8} < 4, K_{3,6} + K_{3,7} + K_{6,7} < 4, K_{3,6} + K_{3,8} + K_{6,8} < 4, \\
&K_{4,5} + K_{4,6} + K_{5,6} < 4, K_{4,5} + K_{4,7} + K_{5,7} < 4, K_{4,5} + K_{4,8} + K_{5,8} < 4, \\
&K_{4,6} + K_{4,7} + K_{6,7} < 4, K_{4,6} + K_{4,8} + K_{6,8} < 4, K_{4,7} + K_{4,8} + K_{7,8} < 4, \\
&K_{5,6} + K_{5,7} + K_{6,7} < 4, K_{5,6} + K_{5,8} + K_{6,8} < 4, K_{5,7} + K_{5,8} + K_{7,8} < 4,
\end{aligned}$$

and 68 inequalities, of four poles:

$$\begin{aligned}
& K_{1,2} + K_{1,3} + K_{1,4} + K_{2,3} + K_{2,4} + K_{3,4} < 6, K_{1,2} + K_{1,3} + K_{1,5} + K_{2,3} + K_{2,5} + K_{3,5} < 6, \\
& K_{1,2} + K_{1,3} + K_{1,6} + K_{2,3} + K_{2,6} + K_{3,6} < 6, K_{1,2} + K_{1,3} + K_{1,7} + K_{2,3} + K_{2,7} + K_{3,7} < 6, \\
& K_{1,2} + K_{1,3} + K_{1,8} + K_{2,3} + K_{2,8} + K_{3,8} < 6, K_{1,2} + K_{1,4} + K_{1,5} + K_{2,4} + K_{2,5} + K_{4,5} < 6, \\
& K_{1,2} + K_{1,4} + K_{1,6} + K_{2,4} + K_{2,6} + K_{4,6} < 6, K_{1,2} + K_{1,4} + K_{1,7} + K_{2,4} + K_{2,7} + K_{4,7} < 6, \\
& K_{1,2} + K_{1,4} + K_{1,8} + K_{2,4} + K_{2,8} + K_{4,8} < 6, K_{1,2} + K_{1,5} + K_{1,7} + K_{2,5} + K_{2,7} + K_{5,7} < 6, \\
& K_{1,2} + K_{1,5} + K_{1,8} + K_{2,5} + K_{2,8} + K_{5,8} < 6, K_{1,2} + K_{1,6} + K_{1,7} + K_{2,6} + K_{2,7} + K_{6,7} < 6, \\
& K_{1,2} + K_{1,6} + K_{1,8} + K_{2,6} + K_{2,8} + K_{6,8} < 6, K_{1,2} + K_{1,7} + K_{1,8} + K_{2,7} + K_{2,8} + K_{7,8} < 6, \\
& K_{1,3} + K_{1,4} + K_{1,5} + K_{3,4} + K_{3,5} + K_{4,5} < 6, K_{1,3} + K_{1,4} + K_{1,6} + K_{3,4} + K_{3,6} + K_{4,6} < 6, \\
& K_{1,3} + K_{1,4} + K_{1,7} + K_{3,4} + K_{3,7} + K_{4,7} < 6, K_{1,3} + K_{1,4} + K_{1,8} + K_{3,4} + K_{3,8} + K_{4,8} < 6, \\
& K_{1,3} + K_{1,5} + K_{1,6} + K_{3,5} + K_{3,6} + K_{5,6} < 6, K_{1,3} + K_{1,5} + K_{1,7} + K_{3,5} + K_{3,7} + K_{5,7} < 6, \\
& K_{1,3} + K_{1,5} + K_{1,8} + K_{3,5} + K_{3,8} + K_{5,8} < 6, K_{1,3} + K_{1,6} + K_{1,7} + K_{3,6} + K_{3,7} + K_{6,7} < 6, \\
& K_{1,3} + K_{1,6} + K_{1,8} + K_{3,6} + K_{3,8} + K_{6,8} < 6, K_{1,3} + K_{1,7} + K_{1,8} + K_{3,7} + K_{3,8} + K_{7,8} < 6, \\
& K_{1,4} + K_{1,5} + K_{1,6} + K_{4,5} + K_{4,6} + K_{5,6} < 6, K_{1,4} + K_{1,5} + K_{1,7} + K_{4,5} + K_{4,7} + K_{5,7} < 6, \\
& K_{1,4} + K_{1,5} + K_{1,8} + K_{4,5} + K_{4,8} + K_{5,8} < 6, K_{1,4} + K_{1,6} + K_{1,7} + K_{4,6} + K_{4,7} + K_{6,7} < 6, \\
& K_{1,4} + K_{1,6} + K_{1,8} + K_{4,6} + K_{4,8} + K_{6,8} < 6, K_{1,4} + K_{1,7} + K_{1,8} + K_{4,7} + K_{4,8} + K_{7,8} < 6, \\
& K_{1,5} + K_{1,6} + K_{1,7} + K_{5,6} + K_{5,7} + K_{6,7} < 6, K_{1,5} + K_{1,6} + K_{1,8} + K_{5,6} + K_{5,8} + K_{6,8} < 6, \\
& K_{1,5} + K_{1,7} + K_{1,8} + K_{5,7} + K_{5,8} + K_{7,8} < 6, K_{1,6} + K_{1,7} + K_{1,8} + K_{6,7} + K_{6,8} + K_{7,8} < 6, \\
& K_{2,3} + K_{2,4} + K_{2,5} + K_{3,4} + K_{3,5} + K_{4,5} < 6, K_{2,3} + K_{2,4} + K_{2,6} + K_{3,4} + K_{3,6} + K_{4,6} < 6, \\
& K_{2,3} + K_{2,4} + K_{2,7} + K_{3,4} + K_{3,7} + K_{4,7} < 6, K_{2,3} + K_{2,4} + K_{2,8} + K_{3,4} + K_{3,8} + K_{4,8} < 6, \\
& K_{2,3} + K_{2,5} + K_{2,6} + K_{3,5} + K_{3,6} + K_{5,6} < 6, K_{2,3} + K_{2,5} + K_{2,7} + K_{3,5} + K_{3,7} + K_{5,7} < 6, \\
& K_{2,3} + K_{2,5} + K_{2,8} + K_{3,5} + K_{3,8} + K_{5,8} < 6, K_{2,3} + K_{2,6} + K_{2,7} + K_{3,6} + K_{3,7} + K_{6,7} < 6, \\
& K_{2,3} + K_{2,6} + K_{2,8} + K_{3,6} + K_{3,8} + K_{6,8} < 6, K_{2,3} + K_{2,7} + K_{2,8} + K_{3,7} + K_{3,8} + K_{7,8} < 6, \\
& K_{2,4} + K_{2,5} + K_{2,6} + K_{4,5} + K_{4,6} + K_{5,6} < 6, K_{2,4} + K_{2,5} + K_{2,7} + K_{4,5} + K_{4,7} + K_{5,7} < 6, \\
& K_{2,4} + K_{2,5} + K_{2,8} + K_{4,5} + K_{4,8} + K_{5,8} < 6, K_{2,4} + K_{2,6} + K_{2,7} + K_{4,6} + K_{4,7} + K_{6,7} < 6, \\
& K_{2,4} + K_{2,6} + K_{2,8} + K_{4,6} + K_{4,8} + K_{6,8} < 6, K_{2,4} + K_{2,7} + K_{2,8} + K_{4,7} + K_{4,8} + K_{7,8} < 6, \\
& K_{2,5} + K_{2,6} + K_{2,7} + K_{5,6} + K_{5,7} + K_{6,7} < 6, K_{2,5} + K_{2,6} + K_{2,8} + K_{5,6} + K_{5,8} + K_{6,8} < 6, \\
& K_{2,5} + K_{2,7} + K_{2,8} + K_{5,7} + K_{5,8} + K_{7,8} < 6, K_{2,6} + K_{2,7} + K_{2,8} + K_{6,7} + K_{6,8} + K_{7,8} < 6, \\
& K_{3,4} + K_{3,5} + K_{3,6} + K_{4,5} + K_{4,6} + K_{5,6} < 6, K_{3,4} + K_{3,5} + K_{3,7} + K_{4,5} + K_{4,7} + K_{5,7} < 6, \\
& K_{3,4} + K_{3,5} + K_{3,8} + K_{4,5} + K_{4,8} + K_{5,8} < 6, K_{3,4} + K_{3,6} + K_{3,7} + K_{4,6} + K_{4,7} + K_{6,7} < 6, \\
& K_{3,4} + K_{3,6} + K_{3,8} + K_{4,6} + K_{4,8} + K_{6,8} < 6, K_{3,5} + K_{3,6} + K_{3,7} + K_{5,6} + K_{5,7} + K_{6,7} < 6, \\
& K_{3,5} + K_{3,6} + K_{3,8} + K_{5,6} + K_{5,8} + K_{6,8} < 6, K_{3,5} + K_{3,7} + K_{3,8} + K_{5,7} + K_{5,8} + K_{7,8} < 6, \\
& K_{3,6} + K_{3,7} + K_{3,8} + K_{6,7} + K_{6,8} + K_{7,8} < 6, K_{4,5} + K_{4,6} + K_{4,7} + K_{5,6} + K_{5,7} + K_{6,7} < 6, \\
& K_{4,5} + K_{4,6} + K_{4,8} + K_{5,6} + K_{5,8} + K_{6,8} < 6, K_{4,5} + K_{4,7} + K_{4,8} + K_{5,7} + K_{5,8} + K_{7,8} < 6, \\
& K_{4,6} + K_{4,7} + K_{4,8} + K_{6,7} + K_{6,8} + K_{7,8} < 6, K_{5,6} + K_{5,7} + K_{5,8} + K_{6,7} + K_{6,8} + K_{7,8} < 6,
\end{aligned}$$

- Search space of approximately 10^{20} integer vectors

Remarkably, the constraint system admits exactly four distinct integer solutions:

Solution 1:

$$\begin{aligned}
K_{1,2} &\rightarrow 1, K_{1,3} \rightarrow 0, K_{1,4} \rightarrow 0, K_{1,5} \rightarrow 2, K_{1,6} \rightarrow 2, K_{1,7} \rightarrow 0, K_{1,8} \rightarrow -1, \\
K_{2,3} &\rightarrow 2, K_{2,4} \rightarrow 1, K_{2,5} \rightarrow 0, K_{2,6} \rightarrow 1, K_{2,7} \rightarrow -1, K_{2,8} \rightarrow 0, \\
K_{3,4} &\rightarrow 1, K_{3,5} \rightarrow 0, K_{3,6} \rightarrow -1, K_{3,7} \rightarrow 1, K_{3,8} \rightarrow 1, \\
K_{4,5} &\rightarrow 1, K_{4,6} \rightarrow 0, K_{4,7} \rightarrow 1, K_{4,8} \rightarrow 0, \\
K_{5,6} &\rightarrow 0, K_{5,7} \rightarrow 1, K_{5,8} \rightarrow 0, K_{6,7} \rightarrow 0, K_{6,8} \rightarrow 2, K_{7,8} \rightarrow 2
\end{aligned}$$

Solution 2:

$$\begin{aligned}
K_{1,2} &\rightarrow 1, K_{1,3} \rightarrow 0, K_{1,4} \rightarrow 0, K_{1,5} \rightarrow 2, K_{1,6} \rightarrow 2, K_{1,7} \rightarrow 0, K_{1,8} \rightarrow -1, \\
K_{2,3} &\rightarrow 2, K_{2,4} \rightarrow 1, K_{2,5} \rightarrow 0, K_{2,6} \rightarrow 1, K_{2,7} \rightarrow 0, K_{2,8} \rightarrow -1, \\
K_{3,4} &\rightarrow 1, K_{3,5} \rightarrow 0, K_{3,6} \rightarrow -1, K_{3,7} \rightarrow 1, K_{3,8} \rightarrow 1, \\
K_{4,5} &\rightarrow 1, K_{4,6} \rightarrow 0, K_{4,7} \rightarrow 0, K_{4,8} \rightarrow 1, \\
K_{5,6} &\rightarrow 0, K_{5,7} \rightarrow 1, K_{5,8} \rightarrow 0, K_{6,7} \rightarrow 0, K_{6,8} \rightarrow 2, K_{7,8} \rightarrow 2
\end{aligned}$$

Solution 3:

$$\begin{aligned}
K_{1,2} &\rightarrow 1, K_{1,3} \rightarrow 0, K_{1,4} \rightarrow 0, K_{1,5} \rightarrow 2, K_{1,6} \rightarrow 2, K_{1,7} \rightarrow 1, K_{1,8} \rightarrow -2, \\
K_{2,3} &\rightarrow 2, K_{2,4} \rightarrow 1, K_{2,5} \rightarrow 0, K_{2,6} \rightarrow 1, K_{2,7} \rightarrow -1, K_{2,8} \rightarrow 0, \\
K_{3,4} &\rightarrow 1, K_{3,5} \rightarrow 0, K_{3,6} \rightarrow -1, K_{3,7} \rightarrow 1, K_{3,8} \rightarrow 1, \\
K_{4,5} &\rightarrow 1, K_{4,6} \rightarrow 0, K_{4,7} \rightarrow 1, K_{4,8} \rightarrow 0, \\
K_{5,6} &\rightarrow 0, K_{5,7} \rightarrow 0, K_{5,8} \rightarrow 1, K_{6,7} \rightarrow 0, K_{6,8} \rightarrow 2, K_{7,8} \rightarrow 2
\end{aligned}$$

Solution 4:

$$\begin{aligned}
K_{1,2} &\rightarrow 1, K_{1,3} \rightarrow 0, K_{1,4} \rightarrow 0, K_{1,5} \rightarrow 2, K_{1,6} \rightarrow 2, K_{1,7} \rightarrow 1, K_{1,8} \rightarrow -2, \\
K_{2,3} &\rightarrow 2, K_{2,4} \rightarrow 1, K_{2,5} \rightarrow 0, K_{2,6} \rightarrow 1, K_{2,7} \rightarrow 0, K_{2,8} \rightarrow -1, \\
K_{3,4} &\rightarrow 1, K_{3,5} \rightarrow 0, K_{3,6} \rightarrow -1, K_{3,7} \rightarrow 1, K_{3,8} \rightarrow 1, \\
K_{4,5} &\rightarrow 1, K_{4,6} \rightarrow 0, K_{4,7} \rightarrow 0, K_{4,8} \rightarrow 1, \\
K_{5,6} &\rightarrow 0, K_{5,7} \rightarrow 0, K_{5,8} \rightarrow 1, K_{6,7} \rightarrow 0, K_{6,8} \rightarrow 2, K_{7,8} \rightarrow 2
\end{aligned}$$

All solutions satisfy the regularity condition $K_i = 4$ for $i = 1, \dots, 8$. Each solution yields a distinct CHY integrand via:

$$I_n = \prod_{1 \leq i < j \leq n} (z_i - z_j)^{-K(s_{ij})} \quad (\text{B.1})$$

For instance, Solution 1 produces:

$$I_8^{[1]} = \frac{z_{18} z_{27} z_{36}}{z_{12} z_{15}^2 z_{16}^2 z_{23}^2 z_{24} z_{26} z_{34} z_{37} z_{38} z_{45} z_{47} z_{57} z_{68}^2 z_{78}^2} \quad (\text{B.2})$$

Solution 2 produces:

$$I_8^{[2]} = \frac{z_{18} z_{28} z_{36}}{z_{12} z_{15}^2 z_{16}^2 z_{23}^2 z_{24} z_{26} z_{34} z_{37} z_{38} z_{45} z_{48} z_{57} z_{68}^2 z_{78}^2} \quad (\text{B.3})$$

Solution 3 produces:

$$I_8^{[3]} = \frac{z_{18}^2 z_{27} z_{36}}{z_{12} z_{15}^2 z_{16}^2 z_{17} z_{23}^2 z_{24} z_{26} z_{34} z_{37} z_{38} z_{45} z_{47} z_{58} z_{68}^2 z_{78}^2} \quad (\text{B.4})$$

Solution 4 produces:

$$I_8^{[4]} = \frac{z_{18}^2 z_{28} z_{36}}{z_{12} z_{15}^2 z_{16}^2 z_{17} z_{23}^2 z_{24} z_{26} z_{34} z_{37} z_{38} z_{45} z_{48} z_{58} z_{68}^2 z_{78}^2} \quad (\text{B.5})$$

The existence of exactly four solutions is non-trivial. It demonstrates that the pole structure alone does not uniquely determine the CHY integrand, revealing a hidden degeneracy in the map from amplitudes to worldsheet representations. This multiplicity has profound implications for understanding the space of consistent quantum field theories within the CHY framework and suggests deeper mathematical structures yet to be uncovered [19, 79, 80].

C Hamiltonian Cycles and 0-Regular Graph Decomposition

This appendix provides the mathematical foundation for the decomposition of 0-regular graphs into standard cross-ratios, as described in Section 4.2. We establish the theoretical basis through Hamiltonian cycle theory and prove a specialized decomposition theorem for 0-regular graphs in the CHY formalism.

We begin with the fundamental definitions from graph theory [81, 82]. Let $G = (V, E)$ be a graph with vertex set V and edge set E . A **Hamiltonian path** in G is a path that visits every vertex exactly once, while a **Hamiltonian cycle** is a cycle that visits every vertex exactly once and returns to the starting vertex. For our application to CHY integrands, we work with multigraphs that allow multiple edges between vertices and distinguish between two types of edges: solid edges (corresponding to factors $(z_i - z_j)^{-1}$) and dashed edges (corresponding to factors $(z_i - z_j)^{+1}$).

A multigraph $G = (V, E_s \cup E_d)$ is called **0-regular** if for every vertex $v \in V$, the net degree satisfies $\deg_{\text{net}}(v) = \deg_s(v) - \deg_d(v) = 0$, where $\deg_s(v)$ and $\deg_d(v)$ are the degrees of vertex v with respect to solid and dashed edges, respectively. The key insight is that 0-regular graphs possess special structural properties that guarantee the existence of certain types of cycles, building upon classical results in graph theory.

Theorem C.1 (Euler's Theorem for 0-regular Graphs). *Every connected 0-regular multigraph contains an Eulerian cycle that alternates between solid and dashed edges.*

Proof. Since the graph is 0-regular, every vertex has equal numbers of solid and dashed edges. This means that at every vertex, we can pair incoming and outgoing edges of different types. By Euler's classical theorem [83] for multigraphs, a connected multigraph

has an Eulerian cycle if and only if every vertex has even degree when considering both edge types together. For 0-regular graphs, this condition is automatically satisfied since $\deg_s(v) = \deg_d(v)$ for all vertices v . \square

The crucial step in our decomposition algorithm is the extraction of four-point cycles that correspond to elementary cross-ratios. This relies on the structural properties guaranteed by results such as Dirac's theorem [84] and Ore's theorem [85] for Hamiltonian cycles, though our specific case requires a more specialized approach due to the alternating edge types.

Lemma C.2 (Four-Point Cycle Existence). *Every 0-regular multigraph on $n \geq 4$ vertices contains a four-point cycle of the form $(v_1, v_2, v_3, v_4, v_1)$ where consecutive edges alternate between solid and dashed types.*

Proof. We construct the cycle using the bipartite structure described in Section 4.2. Partition the vertices into two sets V_L (left) and V_R (right). Since the graph is 0-regular, we can orient the edges such that solid edges go from V_L to V_R and dashed edges go from V_R to V_L . Consider the bipartite representation $G' = (V_L \cup V_R, E')$ where each original vertex v appears in both V_L and V_R , and edges are directed according to their type. Since the original graph is connected and 0-regular, the bipartite representation contains a path of length 4 of the form $v_1^L \xrightarrow{\text{solid}} v_2^R \xrightarrow{\text{dashed}} v_3^L \xrightarrow{\text{solid}} v_4^R \xrightarrow{\text{dashed}} v_1^L$. This corresponds to a four-point alternating cycle $(v_1, v_2, v_3, v_4, v_1)$ in the original graph. \square

Building upon these foundational results, we now establish the main theorem that justifies our decomposition algorithm. This theorem extends classical graph decomposition techniques [82] to the specific case of 0-regular multigraphs with alternating edge types.

Theorem C.3 (0-regular Graph Decomposition). *Every 0-regular multigraph G with $n \geq 4$ vertices can be decomposed into a product of elementary four-point cross-ratios. Specifically, the integrand factor corresponding to G can be written as:*

$$\mathcal{I}_G(z) = \prod_{\alpha} \frac{z_{i_{\alpha}j_{\alpha}} z_{k_{\alpha}l_{\alpha}}}{z_{i_{\alpha}k_{\alpha}} z_{j_{\alpha}l_{\alpha}}} \quad (\text{C.1})$$

where each factor corresponds to a four-point cycle extracted from G .

Proof. We proceed by strong induction on the number of vertices n . For the base case ($n = 4$), Lemma C.2 guarantees the existence of a four-point alternating cycle, which directly corresponds to a single cross-ratio factor. For the inductive step, assume the theorem holds for all 0-regular graphs with fewer than n vertices. Consider a 0-regular graph G with n vertices. By Lemma C.2, we can extract a four-point cycle $C_4 = (v_1, v_2, v_3, v_4, v_1)$ from G , corresponding to a cross-ratio factor $\mathcal{P}_4 = \frac{z_{v_1 v_2} z_{v_3 v_4}}{z_{v_1 v_3} z_{v_2 v_4}}$.

Consider the reduced graph $G' = G \setminus C_4$ obtained by removing the edges of C_4 from G . For each vertex v_i in the cycle C_4 , exactly one solid edge and one dashed edge are removed, so $\deg'_{\text{net}}(v_i) = \deg_{\text{net}}(v_i) - (1 - 1) = 0$. For vertices not in C_4 , no edges are removed, so their net degrees remain zero. Thus G' is also 0-regular. If G' is connected with at least

4 vertices, we apply the inductive hypothesis. If G' becomes disconnected, we apply the inductive hypothesis to each connected component separately, then multiply the results. The complete decomposition is $\mathcal{I}_G(z) = \mathcal{P}_4 \cdot \mathcal{I}_{G'}(z)$. \square

The constructive proof directly yields the algorithmic implementation described in Section 4.2. The algorithm repeatedly extracts four-point cycles from the 0-regular graph until decomposition is complete, with each cycle contributing an elementary cross-ratio factor to the final product.

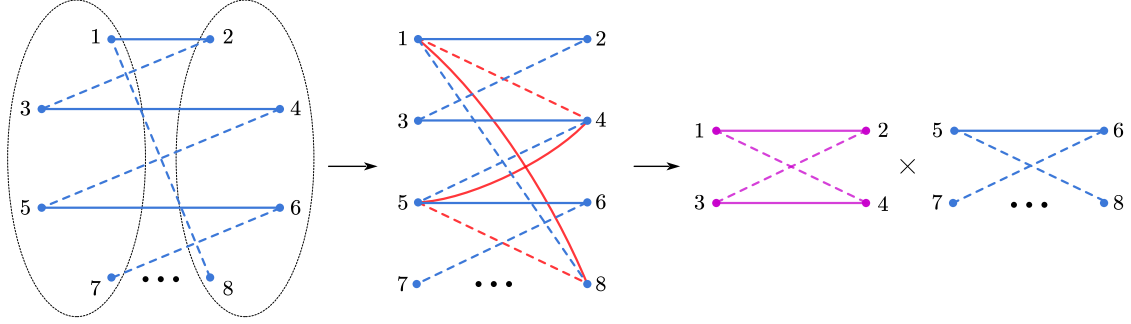


Figure 31. Decompose 0-regular graph to cross-ratios

Algorithm 5 0-regular Graph Decomposition Algorithm

Require: 0-regular multigraph $G = (V, E_s \cup E_d)$

Ensure: Product of elementary cross-ratios $\prod_{\alpha} \mathcal{P}_{\alpha}$

- 1: **Initialize:** Cross-ratio list $\mathcal{L} \leftarrow \emptyset$
 - 2: **while** $|V| \geq 4$ **do**
 - 3: Construct bipartite representation of G
 - 4: Find four-point alternating cycle $C_4 = (v_1, v_2, v_3, v_4, v_1)$
 - 5: Add cross-ratio $\frac{z_{v_1 v_2} z_{v_3 v_4}}{z_{v_1 v_3} z_{v_2 v_4}}$ to \mathcal{L}
 - 6: Remove edges of C_4 from G
 - 7: Update connected components of G
 - 8: **end while**
 - 9: **return** $\prod_{\mathcal{P} \in \mathcal{L}} \mathcal{P}$
-

The decomposition algorithm has polynomial complexity in the number of vertices. Each iteration removes exactly 4 edges (2 solid, 2 dashed) from the graph while maintaining the 0-regular property. Since a 0-regular graph on n vertices has exactly $2n$ edges (counting multiplicities), the algorithm terminates after at most $n/2$ iterations. Finding a four-point cycle in each iteration requires examining the bipartite structure, which can be done in $O(n^2)$ time using standard graph traversal algorithms [81]. Therefore, the total complexity is $O(n^3)$ in the worst case, though practical implementations often achieve $O(n^2)$ performance.

D Discrete AD-Based Neural Network Examples on 8-Point CHY Integrands

To demonstrate the scalability and effectiveness of our discrete automatic differentiation framework, we present a comprehensive example using an 8-point CHY integrand. This example showcases the three-layer network structure and illustrates how our neural-inspired pick-pole algorithm systematically isolates desired pole structures while maintaining exact constraint satisfaction.

Consider the 8-point CHY integrand:

$$I_8 = \frac{z_{18}^2 z_{28} z_{36}}{z_{12} z_{15}^2 z_{16}^2 z_{17} z_{23}^2 z_{24} z_{26} z_{34} z_{37} z_{38} z_{45} z_{48} z_{58} z_{68}^2 z_{78}^2}, \quad (\text{D.1})$$

which generates seven distinct Feynman diagrams:

$$\begin{aligned} & \frac{1}{s_{16} s_{23} s_{78} s_{156} s_{234}} + \frac{1}{s_{15} s_{23} s_{68} s_{234} s_{678}} + \frac{1}{s_{15} s_{23} s_{78} s_{234} s_{678}} + \frac{1}{s_{16} s_{78} s_{126} s_{378} s_{1256}} \\ & + \frac{1}{s_{15} s_{78} s_{156} s_{378} s_{1256}} + \frac{1}{s_{16} s_{78} s_{156} s_{378} s_{1256}} + \frac{1}{s_{15} s_{23} s_{78} s_{156} s_{234}}. \end{aligned} \quad (\text{D.2})$$

The amplitude contains simple poles at s_{15} , s_{16} , s_{23} , s_{68} , s_{78} , s_{156} , s_{234} , s_{378} , s_{678} , and s_{1256} . Our objective is to isolate all contributions containing the pole s_{15} by systematically removing all incompatible poles.

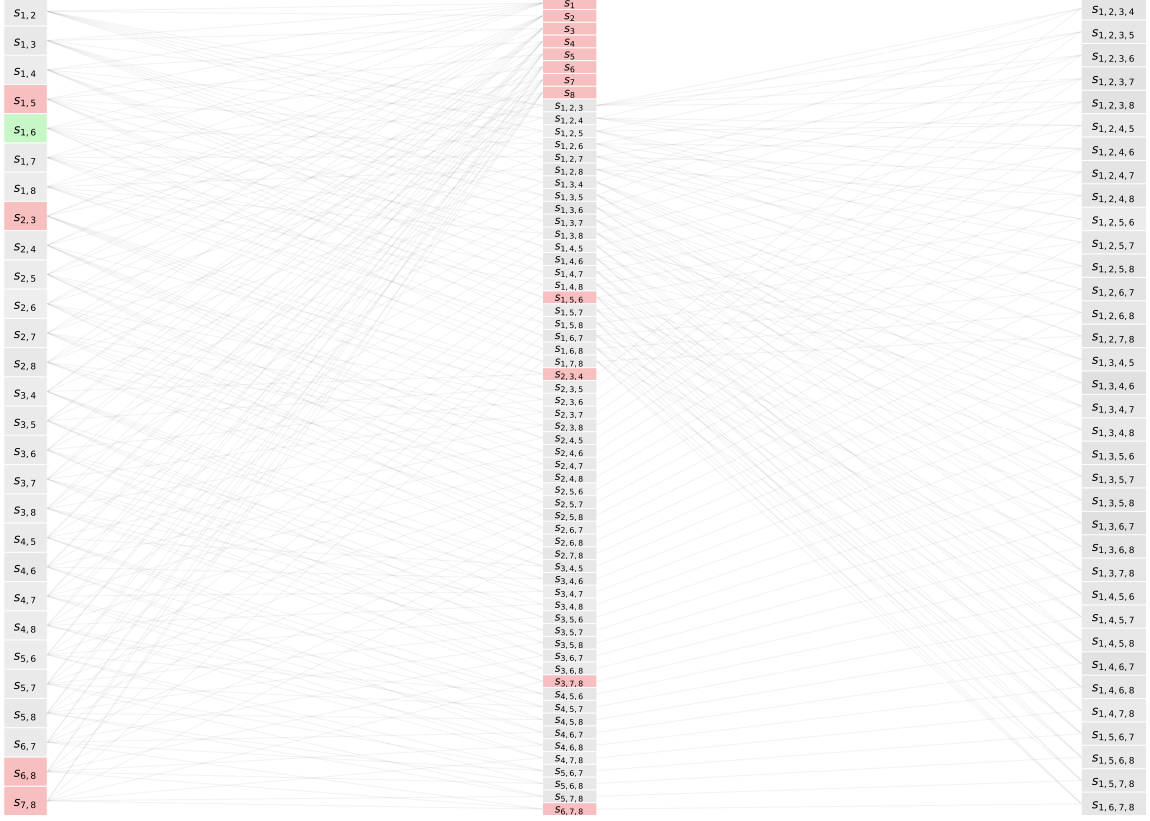


Figure 32. Three-layer hierarchical network structure for 8-point CHY integrand pole selection. The network comprises: (Layer 1) two-particle poles forming the base layer, (Layer 2) single-particle and three-particle poles in the intermediate layer, and (Layer 3) four-particle poles at the top. Gray edges encode the dependency relationships from the recursion relation $K(s_A) = \frac{1}{(|A|-2)!} \sum_{B \subset A, |B|=|A|-1} K(s_B)$. Red nodes represent fixed poles that must be preserved during the algorithm, including the target pole s_{15} and all compatible poles necessary for a consistent amplitude structure.

We construct a three-layer hierarchical network where the dependency relationships are governed by the recursion relation:

$$K(s_A) = \frac{1}{(|A|-2)!} \sum_{B \subset A, |B|=|A|-1} K(s_B). \quad (\text{D.3})$$

As illustrated in Figure 32, this creates a complex network structure where two-particle and single-particle poles form the foundational layer, three-particle poles constitute the intermediate layer, and four-particle poles occupy the top layer. We fix all poles compatible with s_{15} (marked in red) to ensure they remain unchanged throughout the discrete automatic differentiation process.

Removing Incompatible Pole s_{16}

Our first step involves removing the incompatible pole s_{16} by decrementing its K-value:

$$K^*(s_{16}) = K(s_{16}) - 1 = 1. \quad (\text{D.4})$$

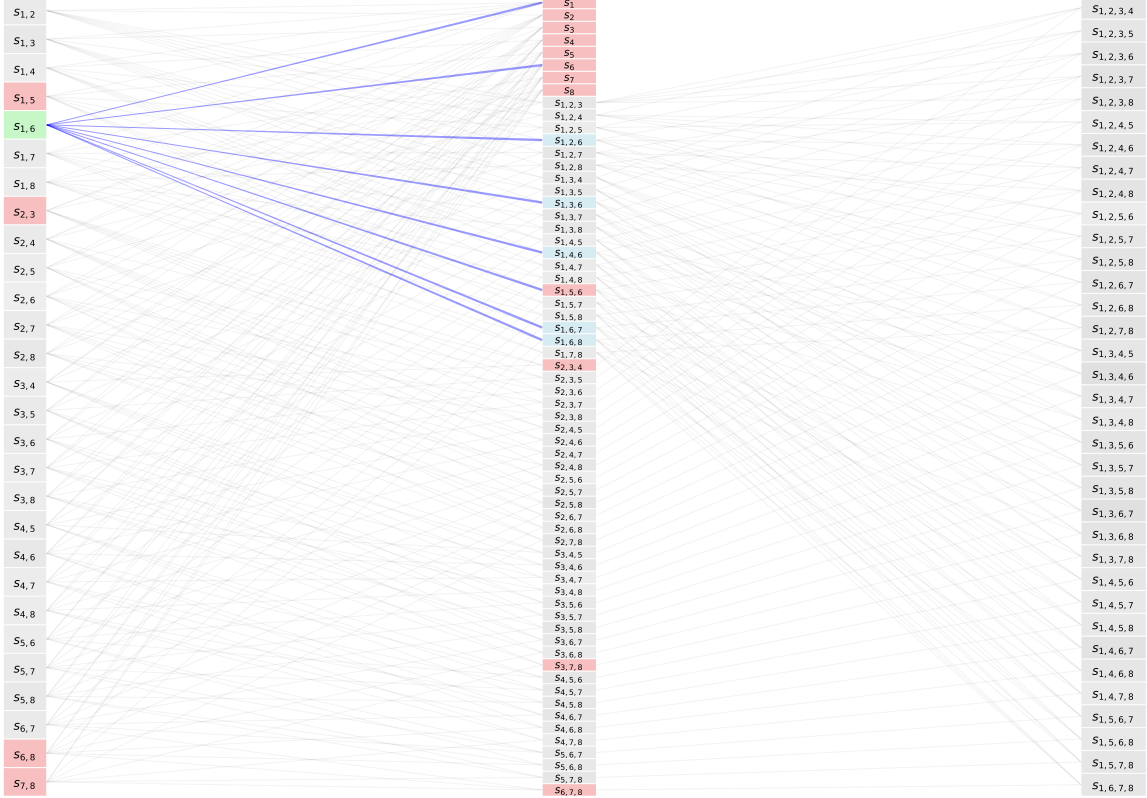


Figure 33. First upward propagation phase in the discrete automatic differentiation algorithm. The modification $\Delta K = -1$ at pole s_{16} (highlighted in green) triggers upward propagation throughout the network hierarchy. Blue arrows trace the propagation pathways to all three-particle supersets and single-particle subsets containing pole s_{16} . The algorithm systematically decrements the K-values of s_{16} 's three-particle supersets: s_{126} , s_{136} , s_{146} , s_{156} , s_{167} , and s_{168} by 1 unit each, following the recursion constraints. Critical fixed constraints are encountered at s_{156} , s_1 , and s_6 (red nodes), which triggers the backward propagation mechanism to maintain network consistency.

The upward propagation phase, shown in Figure 33, demonstrates how the initial modification cascades through the network hierarchy. The algorithm encounters fixed constraints at nodes s_{156} , s_1 , and s_6 , which cannot be modified due to physical requirements. This triggers the backward propagation mechanism.

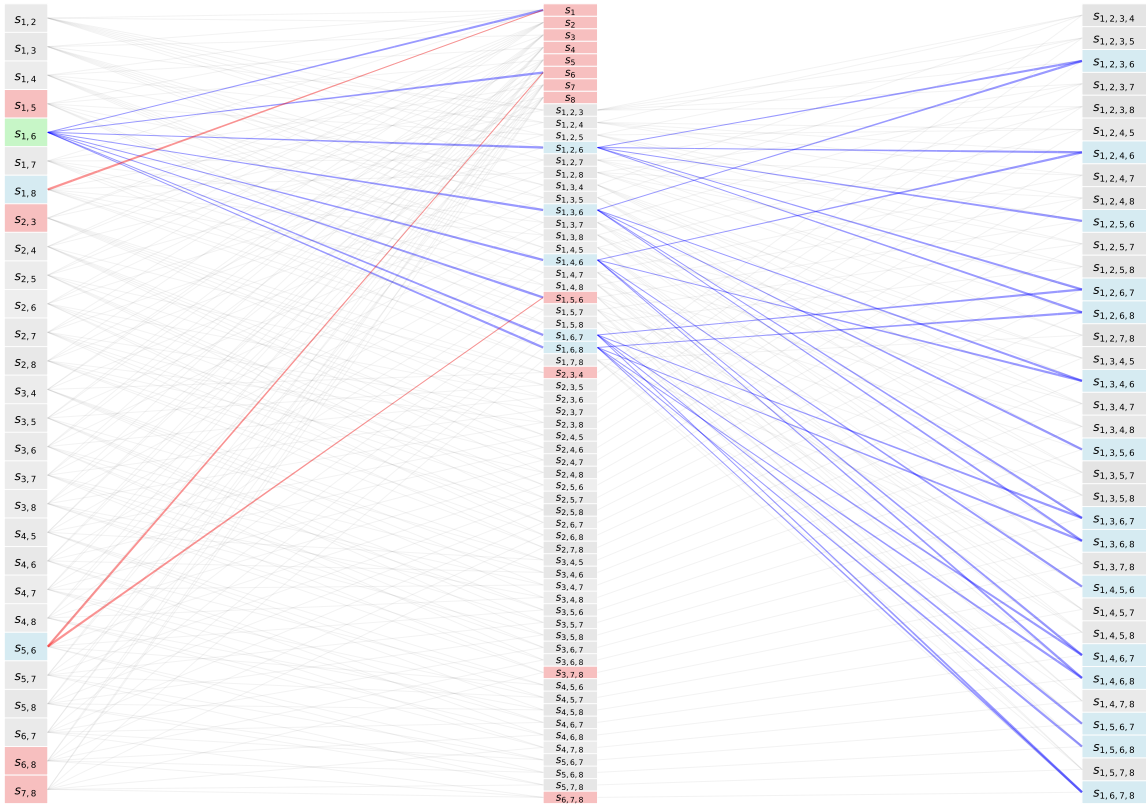


Figure 34. Backward propagation with simultaneous multi-layer updates. When upward propagation encounters fixed constraints, the discrete automatic differentiation algorithm activates backward propagation (red arrows) to redistribute changes while preserving all recursion relations. The algorithm strategically selects s_{56} (intersection of dependent subsets from fixed point s_{156} and superset of fixed node s_6) and s_{18} (superset of fixed point s_1), incrementing their K-values by $+1$. Simultaneously, the algorithm propagates from the second to third layer (blue arrows), updating four-point supersets by -0.5 to maintain consistency across all hierarchical levels.

The backward propagation phase, illustrated in Figure 34, shows the algorithm's sophisticated constraint handling. The system compensates for fixed constraints by selecting appropriate alternative poles and adjusting their values. Concurrently, changes propagate to the third layer, maintaining global consistency.

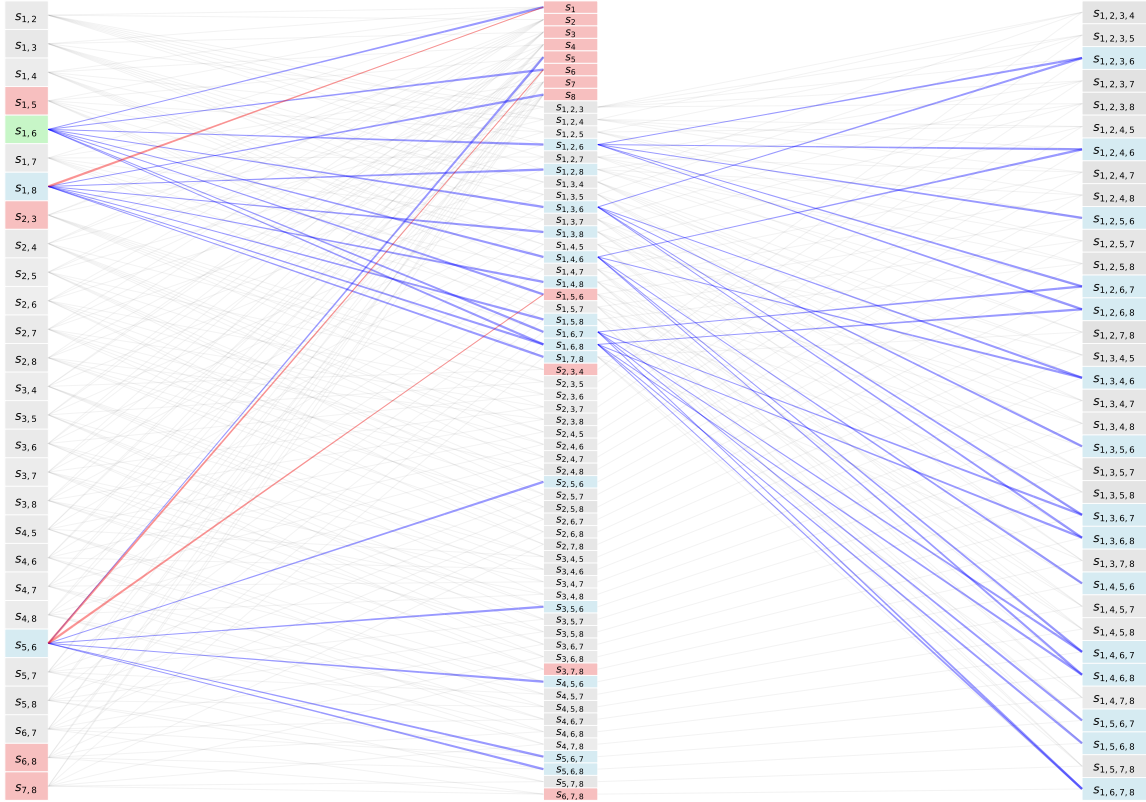


Figure 35. Second upward propagation cascade from compensatory modifications. The changes introduced at s_{18} and s_{56} during backward propagation now trigger their own upward propagation sequences (blue arrows). Each pole's three-particle supersets receive +1 increments: s_{18} affects s_{128} , s_{138} , s_{148} , s_{158} , s_{168} , and s_{178} , while s_{56} affects s_{156} , s_{256} , s_{356} , s_{456} , s_{567} , and s_{568} . The propagation encounters additional fixed points s_5 and s_8 , necessitating another backward propagation cycle to resolve the emerging constraint conflicts.

As shown in Figure 35, the compensatory changes from the previous step now generate their own propagation effects. The algorithm encounters additional fixed points, demonstrating the iterative nature of the constraint resolution process.



Figure 36. Second backward propagation cycle with inter-layer constraint resolution. The encounter with fixed points s_5 and s_8 activates another backward propagation phase (red arrows from second to first layer). The algorithm identifies s_{58} as the intersection of dependent supersets from fixed nodes s_5 and s_8 , decrementing its K-value by -1 to compensate for the constrained propagation. Simultaneously, upward propagation continues to the third layer (blue arrows), where four-point supersets of the affected three-particle poles receive $+0.5$ increments, ensuring that all recursion relations remain exactly satisfied throughout the multi-layer network.

The second backward propagation cycle, depicted in Figure 36, shows how the algorithm systematically resolves cascading constraints. The selection of s_{58} as a compensatory adjustment demonstrates the algorithm's ability to find optimal solutions within the constraint space.



Figure 37. Final upward propagation completing the constraint resolution. The modification at s_{58} triggers the final upward propagation phase (blue arrows), decrementing its three-particle supersets s_{158} , s_{258} , s_{358} , s_{458} , s_{568} , s_{578} , and s_{678} by -1 each. This propagation proceeds without encountering additional fixed constraints, indicating successful resolution of all constraint conflicts.

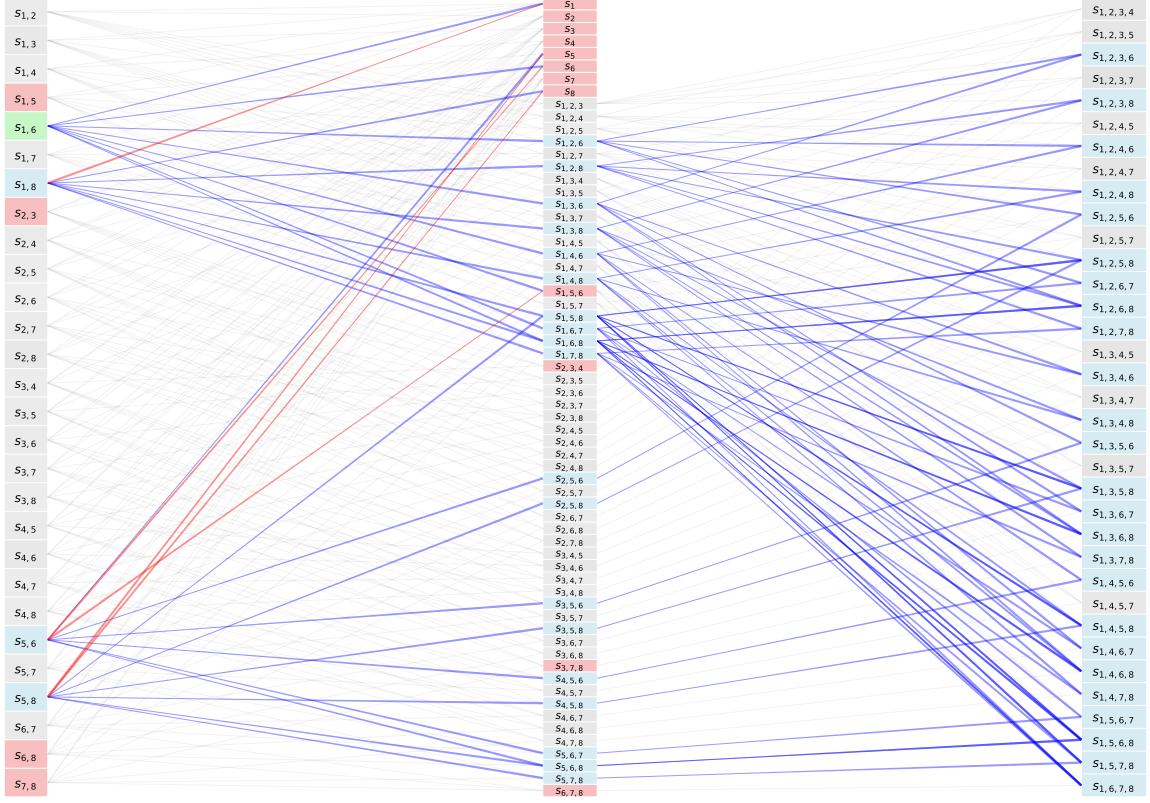


Figure 38. The algorithm seamlessly continues to update the third layer, where four-point super-sets receive corresponding -0.5 decrements to maintain the recursive relationships across all network levels. This systematic propagation through all network layers ensures that every recursion relation $K(s_A) = \frac{1}{(|A|-2)!} \sum_{B \subset A, |B|=|A|-1} K(s_B)$ remains exactly satisfied. The successful completion of this propagation without further constraint violations confirms that the removal of incompatible pole s_{16} has been achieved while preserving all required poles and maintaining network consistency.

The final propagation stages, shown in Figures 37 and 38, demonstrate the algorithm's convergence. The absence of additional constraint violations indicates successful completion of the pole removal process.

Upon completion of the discrete automatic differentiation process, the algorithm successfully removes the incompatible pole s_{16} while preserving all constraints. The modified CHY integrand becomes:

$$I_8^* = \frac{z_{18} z_{28} z_{36}}{z_{12} z_{15}^2 z_{16} z_{17} z_{23}^2 z_{24} z_{26} z_{34} z_{37} z_{38} z_{45} z_{48} z_{56} z_{68}^2 z_{78}^2}, \quad (\text{D.5})$$

which produces the refined amplitude:

$$\frac{1}{s_{15} s_{23} s_{68} s_{234} s_{678}} + \frac{1}{s_{15} s_{23} s_{78} s_{234} s_{678}} + \frac{1}{s_{15} s_{78} s_{156} s_{378} s_{1256}} + \frac{1}{s_{15} s_{23} s_{78} s_{156} s_{234}}. \quad (\text{D.6})$$

This result successfully isolates all terms containing the desired pole s_{15} , demonstrating the effectiveness of our neural-inspired approach for higher-multiplicity CHY integrands.

The 8-point example showcases several key features of our discrete automatic differentiation framework:

- **Three-layer architecture:** Unlike the 6-point case with its two-layer structure, the 8-point example requires a three-layer network, demonstrating scalability to higher multiplicities.
- **Cascading constraint resolution:** The algorithm successfully handles multiple rounds of backward propagation, showing robustness in complex constraint environments.
- **Exact constraint satisfaction:** Throughout the entire process, all recursion relations remain exactly satisfied, with no approximations or numerical errors.

This 8-point demonstration validates the practical applicability of our approach to realistic amplitude calculations and establishes the foundation for extensions to even higher multiplicities and more complex pole structures. The systematic nature of the constraint resolution process suggests that the method will continue to scale effectively as we move toward the frontiers of current amplitude computation capabilities.

E Examples: 8-Point CHY Integrand with Higher-Order Poles

We now demonstrate the scalability of our enhanced decomposition method through a more complex eight-point example. This case illustrates how the systematic approach based on 0-regular graph decomposition maintains its computational advantages even as the complexity increases significantly.

Consider the eight-point CHY integrand

$$I_8 = \frac{1}{z_{12}^3 z_{15} z_{26} z_{36} z_{38}^3 z_{45}^3 z_{47} z_{67}^2 z_{78}}, \quad (\text{E.1})$$

whose 4-regular graph representation is shown in Figure 39.

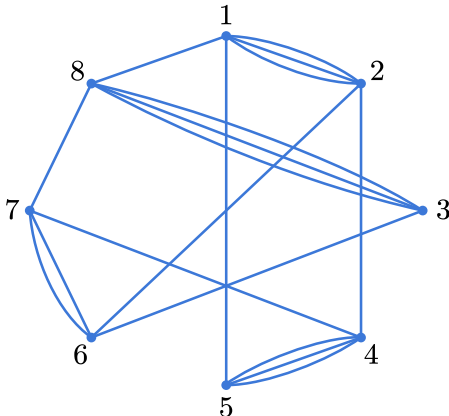


Figure 39. The 4-regular graph representation of the eight-point CHY integrand I_8 . The edge multiplicities directly encode the denominator powers in equation (E.1). The triple edges at (1, 2), (3, 8), and (4, 5) immediately reveal three double poles, while the more complex edge structure suggests an additional higher-order pole that requires careful analysis.

Using the pole index formula, we identify all subsets with $\chi(A) > 0$:

$$\{1, 2\}, \{3, 8\}, \{4, 5\}, \{1, 2, 4, 5\} \quad (\text{E.2})$$

where $\chi(A) = 1$ for each, indicating four constraints that must be addressed. The presence of the four-particle pole s_{1245} makes this example particularly challenging, as it introduces correlations between the decomposition steps.

In the original method [16], since the CHY-integrand I_8 has four higher-order poles s_{12} s_{38} s_{45} s_{1245} , we need to find 4 basic cross-ratio identities to multiply by the CHY-integrand I_8 . One of the basic cross-ratio identities of the subset $\{1, 2\}$, one of the subset $\{3, 8\}$, one of the subset $\{4, 5\}$ and one of the subset $\{1, 2, 4, 5\}$. Since identity of the subset $\{1, 2\}$, the subset $\{3, 8\}$ and the subset $\{4, 5\}$ contains 5 terms and identity of the subset $\{1, 2, 4, 5\}$ contains 9 terms, after multiplying four identities the original CHY-integrand would be decomposed into $5 \times 5 \times 5 \times 9 = 1125$ terms.

To reduce these higher-order poles and redundant items, we construct a six-point cross-ratio factor $\frac{z_{12}z_{38}z_{45}}{z_{18}z_{35}z_{42}}$ targeting the three two-particle double poles. Figure 40 shows its systematic decomposition.

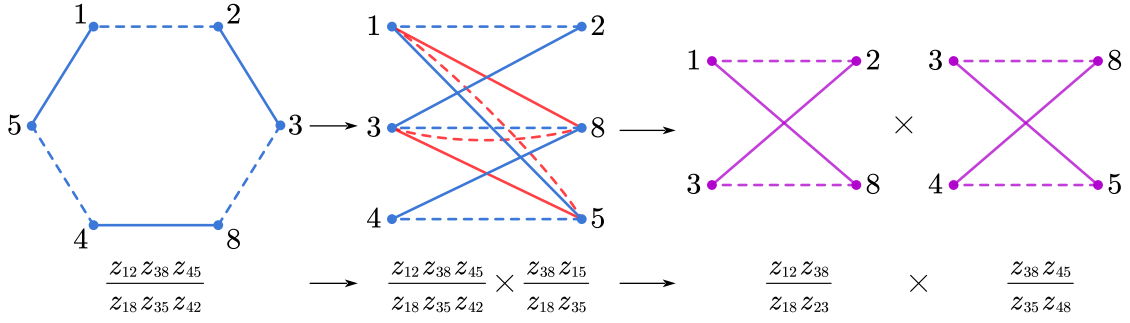


Figure 40. Decomposition of the six-point cross-ratio factor for the eight-point integrand. The bipartite representation reveals the natural factorization into $\frac{z_{12} z_{38} z_{45}}{z_{18} z_{35} z_{42}} \times \frac{z_{38} z_{15}}{z_{18} z_{35}}$, providing the foundation for our two-stage decomposition strategy. This decomposition is specifically designed to address the three two-particle double poles while minimizing interference with the four-particle pole s_{1245} .

Round 1: Initial Decomposition

Based on the cross-ratio decomposition, we select two strategic identities:

$$I_8[\{1, 2\}, 1, 8] = -\frac{s_{23} z_{12} z_{38}}{s_{12} z_{18} z_{23}} - \frac{s_{24} z_{12} z_{48}}{s_{12} z_{18} z_{24}} - \frac{s_{25} z_{12} z_{58}}{s_{12} z_{18} z_{25}} - \frac{s_{26} z_{12} z_{68}}{s_{12} z_{18} z_{26}} - \frac{s_{27} z_{12} z_{78}}{s_{12} z_{18} z_{27}}, \quad (\text{E.3})$$

$$I_8[\{4, 5\}, 5, 3] = -\frac{s_{41} z_{13} z_{45}}{s_{45} z_{14} z_{35}} - \frac{s_{42} z_{23} z_{45}}{s_{45} z_{24} z_{35}} - \frac{s_{46} z_{36} z_{45}}{s_{45} z_{35} z_{46}} - \frac{s_{47} z_{37} z_{45}}{s_{45} z_{35} z_{47}} - \frac{s_{48} z_{38} z_{45}}{s_{45} z_{35} z_{48}}. \quad (\text{E.4})$$

Multiplying I_8 by these identities produces $5^2 = 25$ terms, whose structure is shown in Figure 41.

The decomposition yields three categories:

- 9 terms with only simple poles
- 12 terms with double pole s_{38}
- 4 terms with double poles s_{38} and s_{1245}

Round 2: Eliminating the s_{38} Double Pole

For the 12 terms containing double pole s_{38} , we apply the identity:

$$I_8[\{3, 8\}, 3, 4] = -\frac{s_{81} z_{14} z_{38}}{s_{38} z_{18} z_{34}} - \frac{s_{82} z_{24} z_{38}}{s_{38} z_{28} z_{34}} - \frac{s_{85} z_{45} z_{38}}{s_{45} z_{34} z_{58}} - \frac{s_{86} z_{46} z_{38}}{s_{38} z_{34} z_{68}} - \frac{s_{87} z_{47} z_{38}}{s_{38} z_{34} z_{78}}. \quad (\text{E.5})$$

Figure 42 illustrates this decomposition for one representative term.

This process transforms the 12 terms with double pole s_{38} into $12 \times 5 = 60$ terms with only simple poles.

For the 4 terms containing both s_{38} and s_{1245} double poles, applying identity (E.5) yields 20 terms, of which 12 have only simple poles while 8 retain the double pole s_{1245} . Figure 43 shows a representative example.

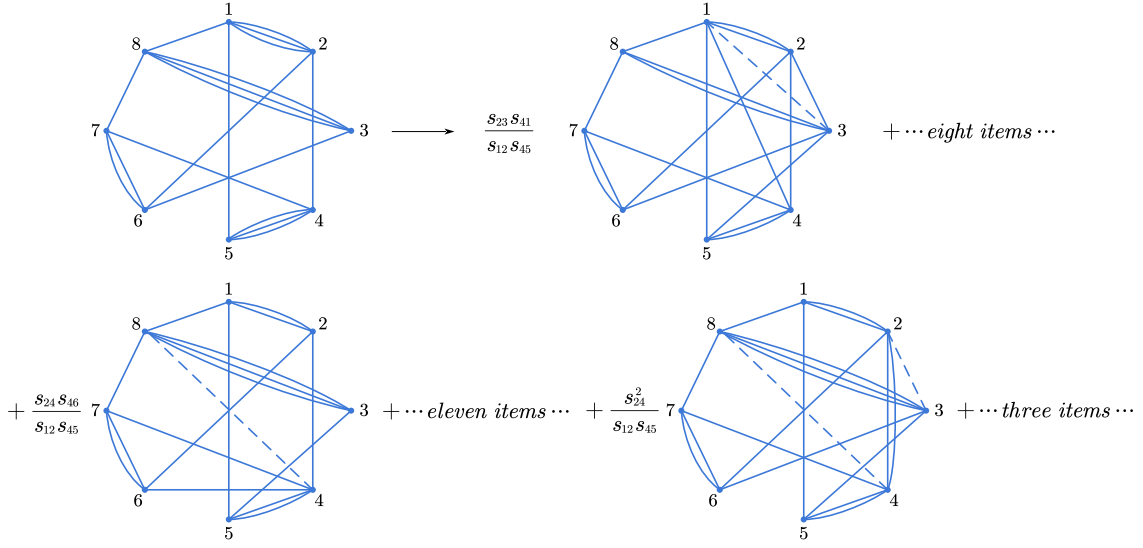


Figure 41. Round 1 decomposition results: The initial application of identities (E.3) and (E.4) produces 25 terms organized in a 5×5 grid. The first 9 terms (top-left, shown in gray) already contain only simple poles. The central 12 terms retain the double pole s_{38} , while the final 4 terms (bottom-right) contain both s_{38} and s_{1245} as double poles, requiring the most extensive further treatment.

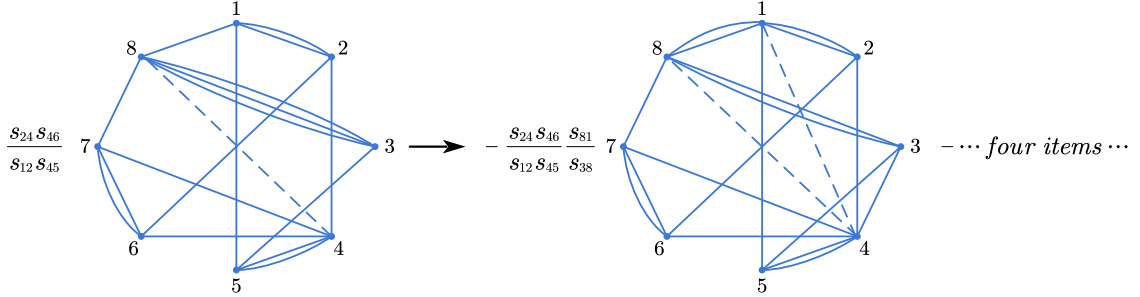


Figure 42. Round 2 decomposition of a term with double pole s_{38} . The application of identity (E.5) to the term $\frac{s_{24}s_{46}}{s_{12}s_{45}} \frac{z_{84}}{z_{21}^2 z_{42} z_{51} z_{53} z_{54}^2 z_{62} z_{64} z_{74} z_{76}^2 z_{81} z_{83}^3 z_{87}}$ produces 5 terms with only simple poles. The cross-ratio factors in the identity precisely cancel the z_{83}^3 contribution, reducing the pole order as required.

Round 3: Final Decomposition of s_{1245}

The remaining 8 terms with double pole s_{1245} require the application of a nine-term identity:

$$\begin{aligned}
 I_8[\{1, 2, 4, 5\}, 1, 3] = & -\frac{s_{26}z_{12}z_{36}}{s_{1245}z_{13}z_{26}} - \frac{s_{46}z_{14}z_{36}}{s_{1245}z_{13}z_{46}} - \frac{s_{56}z_{15}z_{36}}{s_{1245}z_{13}z_{56}} - \frac{s_{27}z_{12}z_{37}}{s_{1245}z_{13}z_{27}} \\
 & - \frac{s_{28}z_{12}z_{38}}{s_{1245}z_{13}z_{28}} - \frac{s_{47}z_{14}z_{37}}{s_{1245}z_{13}z_{47}} - \frac{s_{48}z_{14}z_{38}}{s_{1245}z_{13}z_{48}} - \frac{s_{57}z_{15}z_{37}}{s_{1245}z_{13}z_{57}} - \frac{s_{58}z_{15}z_{38}}{s_{1245}z_{13}z_{58}}.
 \end{aligned} \tag{E.6}$$

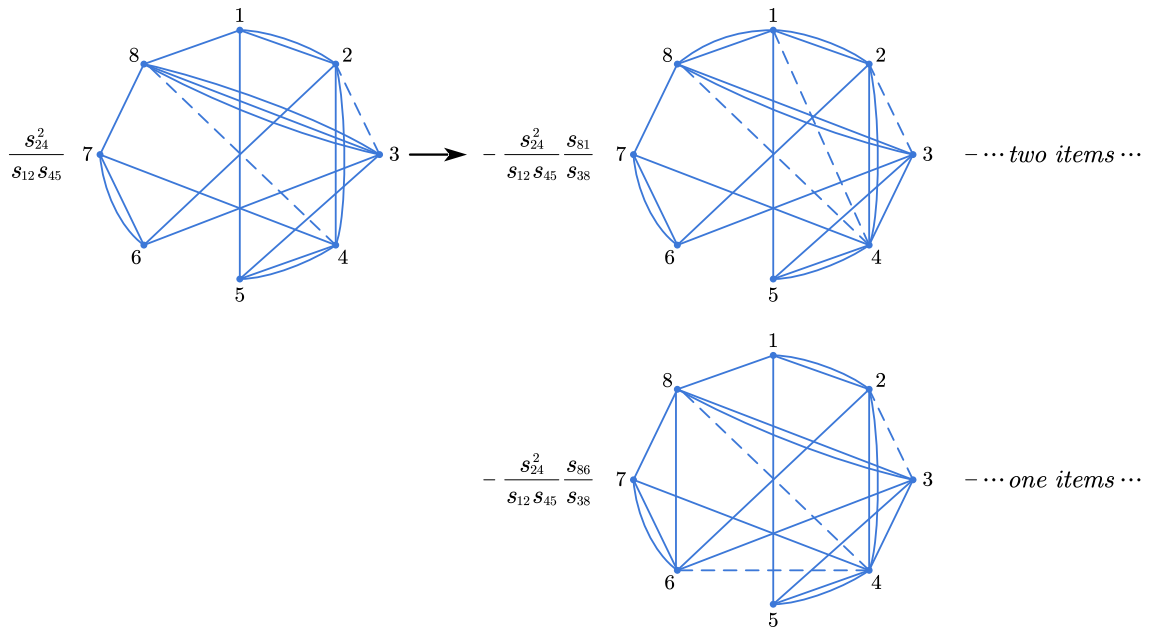


Figure 43. Round 2 decomposition of a term with double poles s_{38} and s_{1245} . After applying identity (E.5), the resulting 5 terms split into two categories: 3 terms (shown in gray) with only simple poles, and 2 terms (shown in white) that still contain the double pole s_{1245} , necessitating a third round of decomposition.

Figure 44 demonstrates the final decomposition step.

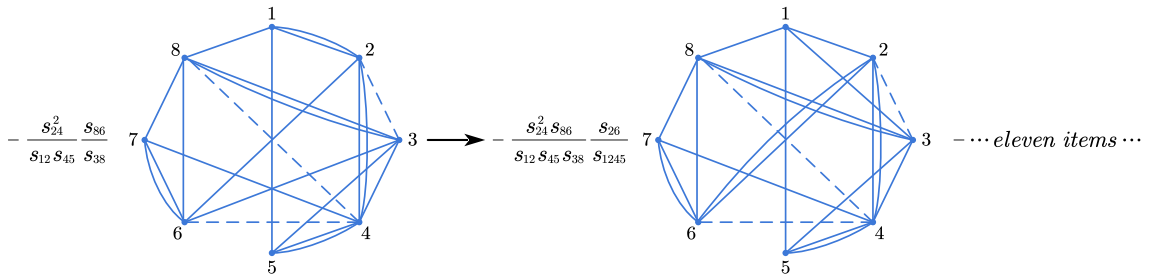


Figure 44. Round 3 final decomposition. The nine-term identity (E.6) applied to a term with double pole s_{1245} produces 9 CHY integrands with only simple poles. This completes the systematic reduction of all higher-order poles in the original eight-point integrand. The complexity of this final step (9 terms) reflects the four-particle nature of the s_{1245} pole.

Through this three-round process, the eight-point CHY integrand I_8 with four double poles is systematically decomposed into $9 + 60 + 12 + 72 = 153$ terms, each containing only simple poles. The improvement over traditional methods is summarized in the following table:

Method	Round 1	Round 2	Round 3	Round 4	Total
Systematic algorithm [16]	5 [5]	25 [20]	105 [20]	265 [0]	265
Our method	25 [16]	89 [8]	153 [0]	—	153

Numbers in brackets [·] indicate terms with remaining higher-order poles at each stage.

References

- [1] Freddy Cachazo, Song He, and Ellis Ye Yuan. Scattering equations and Kawai-Lewellen-Tye orthogonality. *Phys. Rev. D*, 90(6):065001, 2014.
- [2] Freddy Cachazo, Song He, and Ellis Ye Yuan. Scattering of Massless Particles: Scalars, Gluons and Gravitons. *JHEP*, 07:033, 2014.
- [3] Freddy Cachazo, Song He, and Ellis Ye Yuan. Scattering of Massless Particles in Arbitrary Dimensions. *Phys. Rev. Lett.*, 113(17):171601, 2014.
- [4] Freddy Cachazo, Song He, and Ellis Ye Yuan. Scattering Equations and Matrices: From Einstein To Yang-Mills, DBI and NLSM. *JHEP*, 07:149, 2015.
- [5] Louise Dolan and Peter Goddard. The polynomial form of the scattering equations. *JHEP*, 07:029, 2014.
- [6] Song He et al. On the new factorizations of yang-mills amplitudes. *JHEP*, 02:074, 2025.
- [7] Yong Zhang. New factorizations of yang-mills amplitudes. *Physical Review D*, 111(8):085004, 2025.
- [8] Samuel Abreu et al. One-loop amplitudes in gauge theories. *Phys. Rev. D*, 111:065015, 2025.
- [9] Song He and Ellis Ye Yuan. One-loop Scattering Equations and Amplitudes from Forward Limit. *Phys. Rev. D*, 92(10):105004, 2015.
- [10] Freddy Cachazo, Song He, and Ellis Ye Yuan. New double soft emission theorems. *Phys. Rev. D*, 92:065030, 2015.
- [11] Lionel Mason and David Skinner. Ambitwistor strings and the scattering equations. *JHEP*, 07:048, 2014.
- [12] Yvonne Geyer, Lionel Mason, Ricardo Monteiro, and Piotr Tourkine. Loop Integrands for Scattering Amplitudes from the Riemann Sphere. *Phys. Rev. Lett.*, 115(12):121603, 2015.
- [13] Bo Feng. Chy-construction of planar loop integrands of cubic scalar theory. *JHEP*, 05:061, 2016.
- [14] Bo Feng and Chang Hu. One-loop chy-integrand of bi-adjoint scalar theory. *Journal of High Energy Physics*, 2020(02):187, 2020.
- [15] Xiangrui Gao, Song He, and Yong Zhang. Labelled tree graphs, Feynman diagrams and disk integrals. *JHEP*, 11:144, 2017.
- [16] Carlos Cardona, Bo Feng, Humberto Gomez, and Rijun Huang. Cross-ratio Identities and Higher-order Poles of CHY-integrand. *JHEP*, 09:133, 2016.
- [17] Freddy Cachazo, Nick Early, Alfredo Guevara, and Sebastian Mizera. Scattering equations: From projective spaces to tropical grassmannians. *Journal of High Energy Physics*, 2019(06):039, 2019.

- [18] Nima Arkani-Hamed, Yuntao Bai, and Thomas Lam. Positive geometries and canonical forms. *JHEP*, 11:039, 2017.
- [19] Sebastian Mizera. Aspects of scattering amplitudes and moduli space localization. *arXiv*, 2019.
- [20] Yang-Hui He. Machine-learning the string landscape. *Physics Letters B*, 2017.
- [21] Yang-Hui He. Machine-learning the landscape. *Lecture Notes in Mathematics*, 2021.
- [22] Anthony Ashmore, Yang-Hui He, and Burt A. Ovrut. Machine learning calabi–yau metrics. *Fortschritte der Physik*, 2020.
- [23] Ramon Winterhalder, Vitaly Magerya, Emilio Villa, Stephen P. Jones, Matthias Kerner, Anja Butter, Gudrun Heinrich, and Tilman Plehn. Targeting multi-loop integrals with neural networks. *SciPost Phys.*, 12(4):129, 2022.
- [24] Simon Badger, Johannes Henn, Jan Plefka, and Simone Zoia. Scattering Amplitudes in Quantum Field Theory. *arXiv preprint*, 2023.
- [25] Enrico Bothmann, Timo Janssen, Max Knobbe, Tobias Schmale, and Steffen Schumann. Exploring phase space with Neural Importance Sampling. *SciPost Phys.*, 8(4):069, 2020.
- [26] Abdulrahman Almuqaydan, Sergei Gleyzer, and Harrison Prosper. Interpretable machine learning for high-energy physics. *Machine Learning: Science and Technology*, 3:011001, 2022.
- [27] Aurélien Dersy, Matthew D. Schwartz, and Xiaoyuan Zhang. Simplifying Polylogarithms with Machine Learning. *arXiv preprint*, 2023.
- [28] Tianji Cai, Minjie Cheng, Zhengkang Yan, and Yi Yu. TransformerPE: Transformers for Symbolic Regression of Physical Equations. *Physical Review Research*, 6:013154, 2024.
- [29] Abdulhakim Almuqaydan, Sergei Gleyzer, and Harrison Prosper. Symba: symbolic computation of squared amplitudes in high energy physics with machine learning. *Machine Learning: Science and Technology*, 4(1):015007, 2023.
- [30] Tony Hey, Stewart Tansley, and Kristin Tolle, editors. *The Fourth Paradigm: Data-Intensive Scientific Discovery*. Microsoft Research, Redmond, WA, 2009.
- [31] Kun Xu, Yitong Liu, Xiaohui Fan, Yu Ma, Jun Zhang, Qi Liu, and Jianwei Yin. Artificial intelligence: A powerful paradigm for scientific research. *Innovation*, 2(4):100179, 2021.
- [32] Giuseppe Carleo, Ignacio Cirac, Kyle Cranmer, Laurent Daudet, Maria Schuld, Naftali Tishby, Leslie Vogt-Maranto, and Lenka Zdeborová. Machine learning and the physical sciences. *Reviews of Modern Physics*, 2019.
- [33] Luisa Lucie-Smith, Hiranya V. Peiris, Andrew Pontzen, Brian Nord, and Jeyan Thiyaalingam. Deep learning insights into cosmological structure formation. *Phys. Rev. D*, 109(6):063524, 2024.
- [34] Stefania Ebli, Michaël Defferrard, and Gard Spreemann. Simplicial neural networks. *arXiv preprint arXiv:2010.03633*, 2020.
- [35] Cristian Bodnar, Fabrizio Frasca, Yu Guang Wang, Nina Otter, Guido F. Montúfar, Pietro Liò, and Michael M. Bronstein. Weisfeiler and lehman go topological: Message passing simplicial networks. In *Proceedings of the 38th International Conference on Machine Learning (ICML)*, volume 139 of *Proceedings of Machine Learning Research*, pages 1026–1037. PMLR, 2021.

- [36] Christian Baadsgaard, N. E. J. Bjerrum-Bohr, Jacob L. Bourjaily, and Poul H. Damgaard. Integration Rules for Scattering Equations. *JHEP*, 09:129, 2015.
- [37] Tim Adamo, Eduardo Casali, and David Skinner. Ambitwistor strings and the scattering equations at one loop. *JHEP*, 04:104, 2014.
- [38] Z. Bern, J. J. M. Carrasco, and Henrik Johansson. New Relations for Gauge-Theory Amplitudes. *Phys. Rev. D*, 78:085011, 2008.
- [39] Christian Baadsgaard, N. E. J. Bjerrum-Bohr, Jacob L. Bourjaily, and Poul H. Damgaard. Scattering equations and feynman diagrams. *JHEP*, 09:136, 2015.
- [40] Freddy Cachazo, Song He, and Ellis Ye Yuan. Einstein-Yang-Mills Scattering Amplitudes From Scattering Equations. *JHEP*, 01:121, 2015.
- [41] Johannes Broedel and Andre Kaderli. Amplitude recursions with an extra marked point. *arXiv preprint*, 2019.
- [42] Stefania Ebli, Michaël Defferrard, and Gard Spreemann. Simplicial neural networks. *arXiv*, 2020.
- [43] Keyulu Xu, Weihua Hu, Jure Leskovec, and Stefanie Jegelka. How powerful are graph neural networks? *arXiv preprint*, 2018. Published in ICLR 2019.
- [44] Christopher Morris, Martin Ritzert, Matthias Fey, William L. Hamilton, Jan Eric Lenssen, Gaurav Rattan, and Martin Grohe. Weisfeiler and leman go neural: Higher-order graph neural networks. *arXiv*, 2018.
- [45] Ali Zia, Abdelwahed Khamis, James Nichols, Zeeshan Hayder, Vivien Rolland, and Lars Petersson. Topological deep learning: A review of an emerging paradigm. *Artificial Intelligence Review*, 2023.
- [46] Mathilde Papillon, Sophia Sanborn, Mustafa Hajij, and Nina Miolane. Architectures of topological deep learning: A survey of message-passing topological neural networks. *arXiv preprint*, 2023.
- [47] Claudio Battiloro, Lucia Testa, Lorenzo Giusti, Stefania Sardellitti, Paolo Di Lorenzo, and Sergio Barbarossa. Simplicial attention neural networks. *arXiv preprint*, 2022.
- [48] Kelly Maggs, Celia Hacker, and Bastian Rieck. Simplicial representation learning with neural k -forms. In *International Conference on Learning Representations*, 2023. arXiv:2312.08515.
- [49] Michael M. Bronstein, Joan Bruna, Taco Cohen, and Petar Veličković. Geometric deep learning: Grids, groups, graphs, geodesics, and gauges. *arXiv preprint*, 2021.
- [50] Cristian Bodnar, Fabrizio Frasca, Yu Guang Wang, Nina Otter, Guido Montúfar, Pietro Liò, and Michael M. Bronstein. Weisfeiler and leman go topological: Message passing simplicial networks. In *Proceedings of ICML 2021*, 2021.
- [51] Stefania Ebli, Michaël Defferrard, and Gard Spreemann. Simplicial neural networks. In *NeurIPS 2020 Workshop on Topological Data Analysis and Beyond*, 2020.
- [52] Adam Paszke, Sam Gross, Francisco Massa, Adam Lerer, James Bradbury, Gregory Chanan, Trevor Killeen, Zeming Lin, Natalia Gimelshein, Luca Antiga, Alban Desmaison, Andreas Kopf, Edward Yang, Zachary DeVito, Martin Raison, Alykhan Tejani, Sasank Chilamkurthy, Benoit Steiner, Lu Fang, Junjie Bai, and Soumith Chintala. Automatic differentiation in pytorch. In *Advances in Neural Information Processing Systems (NeurIPS) 2017 Autodiff Workshop*, 2017.

- [53] Martín Abadi, Paul Barham, Jianmin Chen, Zhifeng Chen, Andy Davis, Jeffrey Dean, Matthieu Devin, Sanjay Ghemawat, Geoffrey Irving, Michael Isard, Manjunath Kudlur, Josh Levenberg, Rajat Monga, Sherry Moore, Derek Murray, Benoit Steiner, Paul Tucker, Vijay Vasudevan, Pete Warden, Martin Wicke, Yuan Yu, and Xiaoqiang Zheng. Tensorflow: Large-scale machine learning on heterogeneous systems. In *12th USENIX Symposium on Operating Systems Design and Implementation (OSDI)*, pages 265–283. USENIX Association, 2016.
- [54] James Bradbury, Roy Frostig, Peter Hawkins, Matthew James Johnson, Chris Leary, Dougal Maclaurin, George Necula, Adam Paszke, Jake VanderPlas, Skye Wanderman-Milne, and Qiao Zhang. Jax: composable transformations of python+numpy programs. <http://github.com/google/jax>, 2018.
- [55] Andreas Griewank and Andrea Walther. Evaluating derivatives. 2008.
- [56] Rijun Huang, Fei Teng, and Bo Feng. Permutation in the chy-formulation. *Nuclear Physics B*, 932:323–369, 2018.
- [57] Bo Feng and Yaobo Zhang. Note on the Labelled tree graphs. *J. High Energy Phys.*, 2020(12):096, 2020.
- [58] N. Arkani-Hamed and J. Trnka. The Amplituhedron. *JHEP*, 10:030, 2014.
- [59] E. Herrmann and J. Trnka. The SAGEX Review on Scattering Amplitudes, Chapter 7: Positive Geometry of Scattering Amplitudes. *J. Phys. A*, 55(44):443008, 2022.
- [60] C. Even-Zohar, T. Lakrec, and R. J. Tessler. The Amplituhedron BCFW Triangulation. *Invent. Math.*, 239(3):1009–1138, 2025.
- [61] N. Arkani-Hamed, Y. Bai, S. He, and G. Yan. Scattering Forms and the Positive Geometry of Kinematics, Color and the Worldsheet. *JHEP*, 05:096, 2018.
- [62] D. E. Parker. Cluster Algebra Structures for Scattering Amplitudes in $N = 4$ Super Yang-Mills. 2017. Senior Thesis, Brown University.
- [63] N. Arkani-Hamed, J. L. Bourjaily, F. Cachazo, A. B. Goncharov, A. Postnikov, and J. Trnka. Scattering Amplitudes and the Positive Grassmannian. 2012.
- [64] B. Feng, S. He, Y. K. Li, and Y. Zhang. Φ^p Amplitudes from the Positive Tropical Grassmannian: Triangulations of Extended Diagrams. 2024.
- [65] T. Cai, J. M. Henn, C. Kohr, R. Moerman, S. P. Trivedi, A. Volovich, and Z. Wang. Transforming the Bootstrap: Using Transformers to Compute Scattering Amplitudes in Planar $N = 4$ Super Yang-Mills Theory. 2024.
- [66] Christos H Papadimitriou and Kenneth Steiglitz. *Combinatorial optimization: algorithms and complexity*. Courier Corporation, 1998.
- [67] Bernhard Korte and Jens Vygen. Combinatorial optimization. *Algorithms and Combinatorics*, 2012.
- [68] Alexander Schrijver. *Theory of Linear and Integer Programming*. Wiley-Interscience Series in Discrete Mathematics and Optimization. John Wiley & Sons, Chichester, 1998.
- [69] Laurence A. Wolsey. *Integer Programming*. Wiley-Interscience Series in Discrete Mathematics and Optimization. John Wiley & Sons, New York, 1998.
- [70] John E. Mitchell. Integer programming: Branch and cut algorithms. *Encyclopedia of Optimization*, 2008.

- [71] Robert E. Bixby. A brief history of linear and mixed-integer programming computation. *Documenta Mathematica Series*, 2012.
- [72] Yoshua Bengio, Andrea Lodi, and Antoine Prouvost. Machine learning for combinatorial optimization: a methodological tour d’horizon. *arXiv*, 2018.
- [73] Maxime Gasse, Didier Chételat, Nicola Ferroni, Laurent Charlin, and Andrea Lodi. Exact combinatorial optimization with graph convolutional neural networks. *arXiv*, 2019.
- [74] Wolfram Research, Inc. Mathematica, version 14.2, 2024.
- [75] Pauli Virtanen, Ralf Gommers, Travis E. Oliphant, Matt Haberland, Tyler Reddy, David Cournapeau, Evgeni Burovski, Pearu Peterson, Warren Weckesser, Jonathan Bright, Stéfan J. van der Walt, Matthew Brett, Joshua Wilson, K. Jarrod Millman, Nikolay Mayorov, Andrew R. J. Nelson, Eric Jones, Robert Kern, Eric Larson, C J Carey, İlhan Polat, Yu Feng, Eric W. Moore, Jake VanderPlas, Denis Laxalde, Josef Perktold, Robert Cimrman, Ian Henriksen, E. A. Quintero, Charles R. Harris, Anne M. Archibald, Antônio H. Ribeiro, Fabian Pedregosa, Paul van Mulbregt, and SciPy 1.0 Contributors. SciPy 1.0: Fundamental Algorithms for Scientific Computing in Python. *Nature Methods*, 17:261–272, 2020.
- [76] Q. Huangfu and J. A. J. Hall. Parallelizing the dual revised simplex method. In *2018 IEEE High Performance Extreme Computing Conference (HPEC)*, pages 1–7. IEEE, 2018.
- [77] Steven Diamond and Stephen Boyd. Cvxpy: A python-embedded modeling language for convex optimization. *Journal of Machine Learning Research*, 17(83):1–5, 2016.
- [78] Stuart Mitchell. Pulp: A linear programming toolkit for python, 2011. Available at <https://coin-or.github.io/pulp/>.
- [79] Bo Feng, Chang Hu, and Yaobo Zhang. Note on solutions of scattering equations. *Phys. Rev. D*, 105:036015, Feb 2022.
- [80] Freddy Cachazo, Karen Yeats, and Samuel Yusim. Compatible cycles and chy integrals. *Journal of High Energy Physics*, (12):105, 2019. arXiv:1907.12661 [math-ph, hep-th].
- [81] J. A. Bondy and U. S. R. Murty. Graph theory with applications. 1976.
- [82] Reinhard Diestel. Graph theory. *Graduate Texts in Mathematics*, 2017.
- [83] Leonhard Euler. Solutio problematis ad geometriam situs pertinentis. *Commentarii Academiae Scientiarum Petropolitanae*, 8:128–140, 1741.
- [84] G. A. Dirac. Some theorems on abstract graphs. *Proceedings of the London Mathematical Society*, 1952.
- [85] Oystein Ore. Note on hamilton circuits. *The American Mathematical Monthly*, 1960.